

Development and Analysis of Techniques to Improve Air-cooling and Temperature
Uniformity in Battery Packs

By

Seham Shahid

A Thesis Submitted in Partial Fulfilment
of the Requirements for the Degree of

Master of Applied Science

in

The Faculty of Engineering and Applied Science

Mechanical Engineering

University of Ontario Institute of Technology

August, 2017

© Seham Shahid, 2017

Abstract

One of the challenges to the advancement of electric vehicles is the requirement of an effective thermal management system to maintain the temperature, and temperature uniformity of the battery pack and the cell within the operating limits. In this study, a novel concept has been developed to improve air-cooling and temperature uniformity in a simple battery pack by incorporating inlet plenum, jet inlets, and vortex generators. The proposed battery pack concept reduced the maximum temperature by about 6%. Furthermore, the temperature difference between the maximum temperature and the minimum temperature exhibited by the battery pack was reduced by 24%. Additionally, up to 37% improvement in the temperature uniformity within a single cell was achieved. Moreover, the new concept developed in this study achieved the desired temperature uniformity at the cell level and the pack level to within 5 °C.

Acknowledgements

I would like to express my deepest gratitude to my supervisor Dr. Martin Agelin-Chaab for his exemplary guidance, care, patience. He provided me with a remarkable atmosphere for to conduct my research. His immense knowledge, intelligence, and enthusiasm as a scientist inspired me every moment to be more devoted to my research work. His efficiency and vision as an outstanding academician encouraged me to think and see beyond my own perceived limit of capability. He also helped with his insightful comments, challenging questions and great discussions which incited me to widen my research from various perspectives.

Dr. Farrukh Khalid deserves special thanks for his continuous support and help during the course of my research. I would also like to thank my colleagues at UOIT for their assistance especially the people in my research room ACE3030B who helped me during critical times.

I am thankful to my friends Khalique U Zaman, Aisha Tariq, Komal Nadeem, Shuja Azhar, Hasan Iftikhar, Ahmed Alam, Umer Imam Uddin, Muhammad Faizan Rao and Dr. Satyam Panchal for their support. Special thanks to Sundus Ateeq for providing her support and care during the preparation of this thesis.

Last but not the least, I would like to express my gratitude to my grandmother, Mehrunnessa, my parents, Shahid Mahmood and Nuzhat Seema, and my sibling and best friend, Hisham Shahid, for their limitless prayers, support, fortitude, inspiration, and reassurance throughout my life. I am also thankful to my aunts, uncles, and cousins especially Zubair Ahmed Siddiqui, Zahid Mahmood, Shazia Wasim, Nighat Jehan, Riffat Siddiqui, Syed Danish Alam and Syed Faizan Alam for supporting me throughout my life. I would also like to thank Sohail Ahmed Siddiqui, Owais Ahmed Siddiqui and Dr. Khalid Mahmood for helping and supporting me during my graduate studies.

Table of Contents

Abstract.....	ii
Acknowledgements	iii
Table of Contents	iv
List of Tables	vii
List of Figures.....	ix
List of Appendices.....	xii
Nomenclature	xiii
Chapter 1: Introduction.....	1
Chapter 2: Background and Literature Review.....	3
2.1 Electric Batteries	3
2.1.1 Li-ion Cell Types	5
2.1.2 Li-ion Cell Chemistry	7
2.2 Heat Generation within a Cell.....	11
2.3 Thermal Management of Batteries	12
2.3.1 Liquid Cooling	13
2.3.2 Phase Change Material Cooling.....	15
2.3.3 Air Cooling	16
2.3.4 Vortex Generators	20
2.4 Gaps in the Literature.....	22
2.5 Motivation and Objectives.....	23
2.6 Thesis Structure.....	25
Chapter 3: Experimental and Numerical Procedures	27
3.1 Battery Pack Configurations.....	27

3.1.1	Study of Inlet Plenum and Cell Orientations	28
3.1.2	Parametric Study of Case A	29
3.1.3	Reynolds Number Study of Case A	30
3.1.4	Jet Inlet and Multiple Vortex Generator Study for Case A.....	30
3.1.5	Jet Inlet and Multiple Vortex Generator Study for Baseline (Case D).....	33
3.2	Experimental Setup	36
3.3	Experimental Procedure	37
3.4	Uncertainty Analysis	39
3.5	Numerical Modeling.....	41
3.5.1	Mesh Generation	43
3.5.2	Mesh Independence Study	44
3.5.3	Boundary conditions	46
Chapter 4:	Results and Discussion.....	48
4.1	Heat Generation Rate of Cell	48
4.2	Model Validation	49
4.3	Study of Inlet Plenum and Cell Orientations.....	50
4.3.1	Thermal Analysis	50
4.3.2	Air Flow Analysis	57
4.4	Parametric Study and Reynolds Number Study of Case A.....	62
4.4.1	Separating Plate Length Analysis	62
4.4.2	Nozzle Slit Length Analysis	66
4.4.3	Reynolds Number Study	68
4.5	Jet Inlet and Multiple Vortex Generator Study for Case A.....	70
4.5.1	Jet Inlet Analysis.....	70
4.5.2	Multiple Vortex Generator Analysis.....	72
4.5.3	Jet Inlet and MVG Analysis.....	74
4.6	Jet Inlet and Multiple Vortex Generator Study for Baseline (Case D)	78

4.6.1	Jet Inlet and Multiple Vortex Generator Analysis	78
4.6.2	Vortex Generator Placement Analysis	84
4.6.3	Vortex Generator Type Analysis	86
Chapter 5: Conclusions and Recommendations		89
5.1	Summary of Results and Conclusions	89
5.2	Contributions	91
5.3	Recommendations	92
Appendices.....		93
Appendix I.....		93
Appendix II		97
References.....		99

List of Tables

Table 2.1: Battery type performance characteristics (Huat, 2014; Zhang, 2007b).....	4
Table 2.2: Comparison of cylindrical, prismatic and pouch type Li-ion cells (Andrea, 2010) .	6
Table 2.3: Specifications of commercially used Li-ion batteries (Bandhauer et al., 2011; Ohzuku and Brodd, 2007; Huat, 2014).....	10
Table 2.4: Comparison of battery TMS (Rao and Wang, 2011).....	13
Table 3.1: Samsung INR18650-25R cell specifications (SSDICo., 2014).....	27
Table 3.2: Lengths of separating plate and nozzle slit for different test numbers.	30
Table 3.3: Parameters and test numbers for the Reynolds number study.....	30
Table 3.4: Calculated values of relative bias and precision errors and total uncertainty.....	41
Table 3.5: Boundary conditions for Cases A, B, C, and D.....	47
Table 4.1: Temperature differences between the experimental and numerical results.....	50
Table 4.2: Comparison of Case A, B, and C with the baseline battery pack (Case D).....	51
Table 4.3: Comparison of Case A1 with Case A.....	70
Table 4.4: Comparison of Case A2 with Case A.....	72
Table 4.5: Comparison of Case A3 with Case A.....	75
Table 4.6: Comparison of Case D1 with Case D (baseline case).	78
Table 4.7: Comparison of Case D2 with Case D (baseline case).	82

Table 4.8: Comparison of Case D3 with Case D2.....	84
Table 4.9: Comparison of Case D4 with Case D2.....	86

List of Figures

Figure 2.1: Comparison of the volumetric energy density and the gravimetric energy density for various battery technologies (modified from Tarascon and Armand, 2001).	4
Figure 2.2: Internal structures of (a) cylindrical cell (modified from NRC, 2012), (b) prismatic cell (modified from CWTD, 2013) and (c) pouch cell (Tarascon and Armand, 2001).	5
Figure 2.3: Li-ion battery charge and discharge mechanisms (Panchal, 2016).	9
Figure 2.4: Comparison of Li-ion cell chemistries (BU, 2017c).	10
Figure 2.5: Schematic of longitudinal vortices generated by delta winglet vortex generator (modified from He et al., 2014b)	20
Figure 2.6: Basic vortex generator forms: (a) delta wing, (b) rectangular wing, (c) delta winglet, and (d) rectangular winglet vortex generators (modified from Chu et al., 2009).	21
Figure 3.1: Computer aided design (CAD) models of (a) Case A, (b) Case B, (c) Case C and (d) Baseline battery pack (Case D)	28
Figure 3.2: Schematics of (a) Arrangement of cells and (b) Case A battery pack.	29
Figure 3.3: Plan view of schematics of (a) Case A, (b) Case A1, and (c) Case A3.	31
Figure 3.4: Schematic of Case A2; (a) Side view of MVG, (b) Front view of MVG, (c) Plan view of MVG, (d) CAD model of MVG, (e) Side view of Case A2 configuration and (f) Plan view.	32
Figure 3.5: Plan views of schematic of (a) Case D1, (b) Case D2, (c) Case D3 and (d) Case D4.	34
Figure 3.6: CAD model of (a) delta winglet multiple vortex generators and (b) rectangular winglet multiple vortex generator.	35
Figure 3.7: (a) Picture of the plan view of the experimental setup and (b) Schematic of the experimental setup.	36

Figure 3.8: (a) Thermocouple placement locations at the leeward side of the cell; (b) front view of heat flux sensor placement location; and (c) front view of velocity measurement locations at the inlet.	38
Figure 3.9: (a) Side view of generated mesh of Case A, (b) Plan view of generated mesh of Case B, (c) Plan view of generated mesh of Case C and (d) Plan view of generated mesh of Case D.	43
Figure 3.10: Comparison of (a) velocity and (b) temperature for the coarse, medium and fine meshes.	45
Figure 4.1: Heat generation rate and the corresponding temperature increase at 2C discharge rate.	49
Figure 4.2: Model validation: (a) temperatures at location L1 (b) temperatures at location L2 of the cell.	50
Figure 4.3: Temperature distribution of the cells: (a) Baseline battery pack, (b) Case A, (c) Case B, and (d) Case C.	53
Figure 4.4: Maximum temperature of cells across (a) Row 1, (b) Row 2, (c) Row 3 and (d) Row 4.	55
Figure 4.5: Temperature difference between the maximum and minimum temperatures of cells across (a) Row 1, (b) Row 2, (c) Row 3, and (d) Row 4.	56
Figure 4.6: Velocity contours of (a) Case D, (b) Case A, (c) Case B, and (c) Case C in the horizontal plane at 52 mm from the base of the battery pack.	58
Figure 4.7: Turbulence kinetic energy contours of (a) Case D, (b) Case A, (c) Case B, and (c) Case C in the horizontal plane at 52 mm from the base of the battery pack.	60
Figure 4.8: Temperature contours of (a) Case D, (b) Case A, (c) Case B, and (c) Case C in the horizontal plane at 52 mm from the base of the battery pack.	61
Figure 4.9: (a) Maximum temperature, (b) maximum temperature difference, (c) average maximum temperature and (d) average temperature difference across the battery pack for test numbers 1 to 5 in Table 3.2.	63
Figure 4.10: Temperature difference between the maximum and minimum temperatures of cells across (a) Row 1, (b) Row 2, (c) Row 3 and (d) Row 4.	65

Figure 4.11: (a) Maximum temperature, (b) maximum temperature difference, (c) average maximum temperature, and (d) average temperature difference across the battery pack for test numbers 1, 6 and 7 in Table 3.2.	67
Figure 4.12: (a) Maximum temperature, (b) maximum temperature difference, (c) average maximum temperature, and (d) average temperature difference across the battery pack for test numbers 8 to 13 in Table 3.2.	69
Figure 4.13: Contours of (a) velocity, (b) turbulence kinetic energy, and (c) temperature in the horizontal plane at 52 mm from the base of the battery pack for Case A1.....	71
Figure 4.14: Contours of (a) velocity, (b) turbulence kinetic energy, and (c) temperature in the horizontal plane at 52 mm from the base of the battery pack for Case A2.....	74
Figure 4.15: Contours of (a) velocity, (b) turbulence kinetic energy, and (c) temperature in the horizontal plane at 52 mm from the base of the battery pack for Case A3.....	76
Figure 4.16: Contours of (a) velocity, (b) turbulence kinetic energy, and (c) temperature in the horizontal plane at 52 mm from the base of the battery pack for Case A.....	77
Figure 4.17: Contours of (a) velocity, (b) turbulence kinetic energy, and (c) temperature in the horizontal plane at 52 mm from the base of the battery pack for Case D.....	79
Figure 4.18: Contours of (a) velocity, (b) turbulence kinetic energy, and (c) temperature in the horizontal plane at 52 mm from the base of the battery pack for Case D1.....	80
Figure 4.19: Contours of (a) velocity, (b) turbulence kinetic energy, and (c) temperature in the horizontal plane at 52 mm from the base of the battery pack for Case D2.....	83
Figure 4.20: Contours of (a) velocity, (b) turbulence kinetic energy, and (c) temperature in the horizontal plane at 52 mm from the base of the battery pack for Case D3.....	85
Figure 4.21: Contours of (a) velocity, (b) turbulence kinetic energy, and (c) temperature in the horizontal plane at 52 mm from the base of the battery pack for Case D4.....	87
Figure A.1: Various views of the CAD model of the better pack concept developed.....	97
Figure A.2: Schematic of the better pack concept developed: (a) plan view and (b) side view.	98

List of Appendices

Appendix I	93
Appendix II	97

Nomenclature

C	Capacity
c_p	Specific heat capacity ($\text{J kg}^{-1} \text{K}^{-1}$)
D	Cell diameter (m)
E	Total energy (J)
F_i	Blending function in SST model
I	Current (A)
k	Turbulence kinetic energy (J kg^{-1})
k_T	Thermal conductivity ($\text{W m}^{-1} \text{K}^{-1}$)
k_s	Scale factor
N	Number
p	Pressure (Pa)
q''	Heat flux (W m^{-2})
S	Absolute value of shear strain rate
s	Standard deviation
t	Time (s)
V	Voltage (V)

v	Velocity (m s^{-1})
\vec{v}	Velocity vector (m s^{-1})
x_i	Tensor coordinate
y	Nearest wall distance (m)

Symbols

α	SST model constant
β^*	SST model constant
ρ	Density (kg m^{-3})
μ	Viscosity (Pa s)
ω	Specific rate of turbulence dissipation (s^{-1})
σ	Diffusion parameters

Subscripts

ave	Average
c	Coulomb
diff	Difference
HFS	Heat flux sensor
i	Tensor indices

max Maximum

o Initial

x x-direction

y y-direction

z z-direction

Acronyms

CAD Computer Aided Design

CFD Computational Fluid Dynamics

DEC Diethyl Carbonate

DMC Dimethyl Carbonate

DOD Depth of Discharge

DW-MVG Delta Winglet Multiple Vortex Generator

EV Electric Vehicle

EC Ethyl Carbonate

HEV Hybrid Electric Vehicle

IR Internal Resistance

Li-ion Lithium Ion

MCMB Micro-Carbon Microbeads

MVG	Multiple Vortex Generators
NCA	Lithium Nickel Cobalt Aluminum Oxide Battery
NiCd	Nickel-Cadmium
NiMH	Nickel Metal Hydride
NMC	Lithium Nickel Manganese Cobalt Oxide Battery
PC	Propylene Carbonate
PCM	Phase Change Material
PE	Polyethylene
PP	Polypropylene
PTC	Positive Thermal Coefficient
RSD	Relative Standard Deviation
RW-MVG	Rectangular Winglet Multiple Vortex Generator
SOC	State of Charge
TMS	Thermal Management System
VG	Vortex Generator

Chapter 1: Introduction

Climate change is the most important environmental issue today and many countries are adopting various methods to promote sustainability. One of the major contributors to greenhouse gasses and global warming is the transportation industry. The current transportation sector contributes significantly to the increasing amount of greenhouse gas (GHG) emissions in the atmosphere. For instance, the transportation sector in US contributed 27% in 2015 to the greenhouse gas emissions (USEPA, 2015). As a result, there is pressure on the automotive industry from governments around the world to decrease GHG emissions by producing more energy efficient vehicles. To meet this goal the industry has identified transportation electrification as one of the most innovative changes in the automotive sector. Hybrid electric vehicles (HEV) and electric vehicles (EV) are considered sustainable and environmental-friendly options. In the past few years, the market share of these vehicles has increased and is bound to increase further over the coming years. Reports suggest that HEVs and EVs reduce GHG emissions by almost 20%, which can be further reduced by 40% if the electricity used by these vehicles is obtained from renewable sources (Omar et al., 2014).

One of the main challenges to the advancement of EVs is the development of high power and energy density cells. This is needed to overcome the issue of the range anxiety which is critical for the mass adoption of EVs. There are a number of potential candidate cells in the market including nickel metal hydride (NiMH), lithium-ion (Li-ion) and lithium-ion polymer (LiPo) cells. However, a lot of attention has been focused on Li-ion cells because of their high capacity, high efficiency, long-life and slow self-discharge rate (Omar et al., 2014). However, Li-ion cells are most effective when they work within certain temperature and thermal specifications. The operating temperature ranges from 0 °C to 40 °C for the cells to perform without rapid degradation (Li et al., 2013). Heat accumulation in a poorly designed thermal

management system of a battery pack (or battery) can result in overheating of the Li-ion cells which can become a safety hazard and in some extreme cases cause the battery pack to explode. In addition, the degradation of the cells accelerate once the temperature increases and moves out of the operating range, which can result in thermal runaway, reduced efficiency of the battery pack and reduction of the life of the batteries (Yang et al., 2016).

Furthermore, the uniformity in the battery pack impacts the availability of the charging and discharging power. At low temperatures, the cell with the lowest temperature limits the power capability but at high temperatures, the cell with the highest temperature defines the rate of power limiting (Kuper et al., 2009). A large temperature variation across the battery pack causes the individual cells to charge and discharge at different rates resulting in electrically unbalanced cells and subsequently a reduction in the performance of the battery pack. A temperature variation of about 10 to 15 °C in the battery pack can lead to 30 to 50% degradation (Saw et al., 2016). Therefore, uniformity in the temperature of the battery pack is required for optimum performance.

Chapter 2: Background and Literature Review

This chapter reviews the background information related to electric batteries. It discusses the different types of electric battery technologies and lithium-ion cells, different chemistries of lithium ion cells, and the heat generation within the cells. It also provides a literature review on the types of thermal management systems of electric batteries with a focus on forced air cooling of the cylindrical cell battery packs. The detailed definitions of the terms and terminology of batteries can be found in Appendix I.

2.1 Electric Batteries

Previously, lead EVs were developed using lead acid batteries due to their low self-discharge rate and cost. However, in later years new battery chemistries were utilized and lead acid batteries were replaced because of their low energy density and higher weight (Kalhammer et al., 2007). More recently, the potential candidate batteries for EVs in the market include nickel-cadmium (NiCd), nickel metal hydride (NiMH), and lithium-ion (Li-ion) batteries. For electric vehicles, a lot of attention has been focused on Li-ion cells because of their high specific energy and power density (Ling et al. 2015; Qu et al. 2014), high capacity, high efficiency, long-life, and slow self-discharge rate (Omar et al., 2014). The drawbacks of Li-ion cells include high cost and safety issues. A comparison of lead-acid, NiCd, NiMH, and Li-ion is provided in Table 2.1. Additionally, the energy densities of various batteries are shown in Figure 2.1.

Table 2.1: Battery type performance characteristics (Huat, 2014; Zhang, 2007b)

Parameters	Lead Acid	NiCd	NiMH	Li-ion
Nominal Voltage (V)	2.0	1.2	1.2	3.6
Specific Energy (Wh/kg)	30-50	45-80	60-120	100
Energy Density (Wh/L)	60	150	200	230
Specific Power (W/kg)	130	200	250	330
Energy Efficiency (%)	65	80	85	95
Cycle Life	200-300	500-1000	300-500	1000
Safety	Medium	High	High	Low
Cost	Low	Low	Medium	High
Self-discharge (%/month)	5	25-30	30-35	<10
Memory Effect	No	Yes	Yes	No

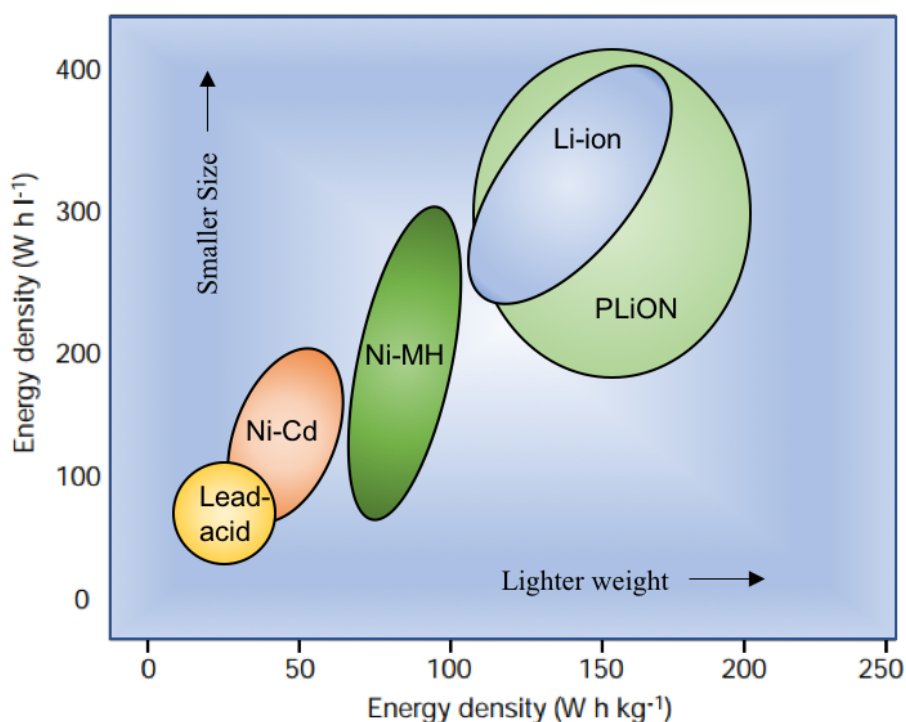


Figure 2.1: Comparison of the volumetric energy density and the gravimetric energy density for various battery technologies (modified from Tarascon and Armand, 2001).

It can be seen that Li-ion cells have the highest nominal voltage of 3.6 V, a high specific energy of 100 Wh/kg, and highest energy density of 230 Wh/L, compared to other battery technologies. Li-ion cells also have a 95% energy efficiency and a specific power of 330 W/kg (32% more than NiMH cells). Therefore, Li-ion cells are considered for this research. The different types of Li-ion cells are discussed in Section 2.1.1.

2.1.1 Li-ion Cell Types

There are mainly three types of cells currently used in the automotive sector for HEVs and EVs, namely, cylindrical, pouch, and prismatic. Cylindrical cells are utilized by Tesla Model S, pouch cells by Chevrolet Volt, and prismatic cells by Nissan Leaf, BMW i3, and Toyota Prius (Arcus, 2016; BU, 2017b). The active material of cylindrical cells is spirally wound over the nylon mandrel, prismatic cells is elliptically wound, and pouch cells is in the form of stacked plates (Huat, 2014). Cylindrical and prismatic cells usually have aluminum and stainless-steel casing for the outermost surface of the cell. Whereas, pouch cells have soft packaging of metalized plastic (Schalkwijk and Scrosati, 2002). The internal structure of different types of cells is shown in Figure 2.2 and a comparison is provided in Table 2.2.

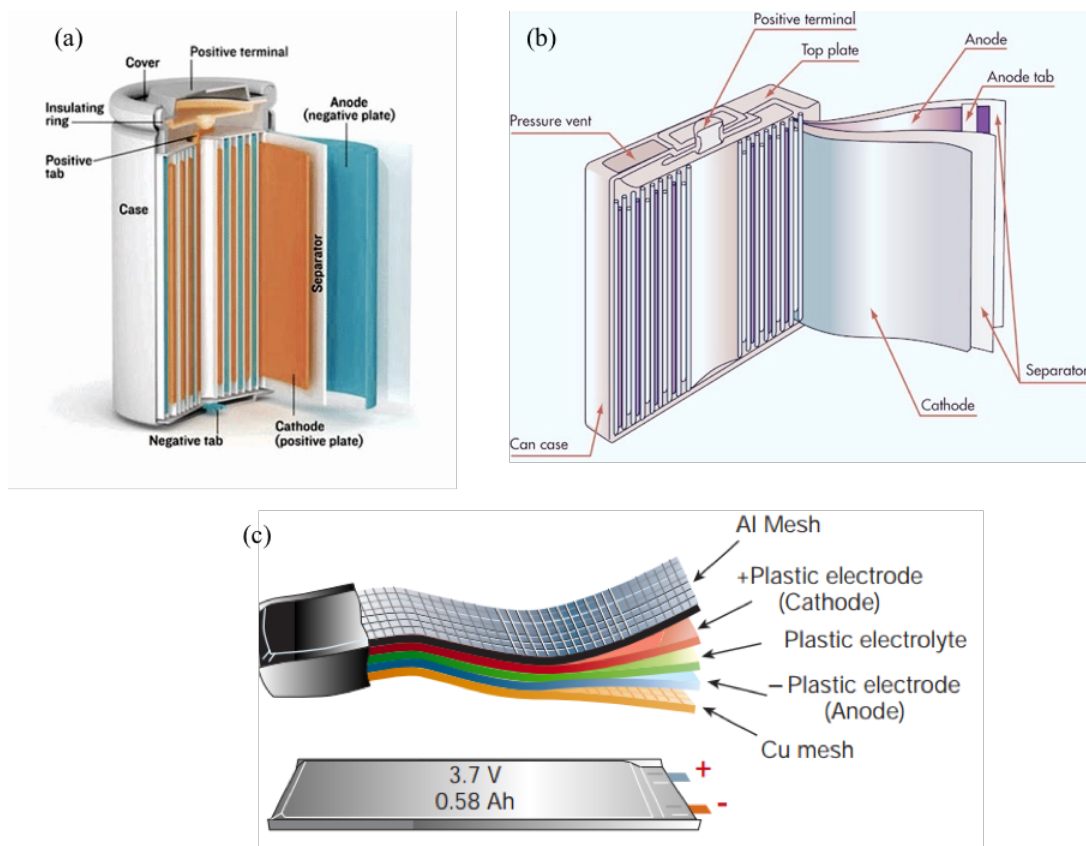


Figure 2.2: Internal structures of (a) cylindrical cell (modified from NRC, 2012), (b) prismatic cell (modified from CWTD, 2013) and (c) pouch cell (Tarascon and Armand, 2001).

Table 2.2: Comparison of cylindrical, prismatic and pouch type Li-ion cells (Andrea, 2010)

Parameters	Small Cylindrical	Large Cylindrical	Prismatic	Pouch
Shape	Contained in metal casing.	Contained in metal casing.	Contained in semi-hard plastic or metal casing	Contained in aluminum soft bag
Connections	Welded nickel or copper strips or plates	Treaded stud for nut or threaded hole for bolt	Thread hole for bolt	Tabs that are clamped, welded or soldered
Retention against expansion	Inherent from cylindrical shape	Inherent from cylindrical shape	Requires retaining plates at ends of battery	Requires retaining plates at ends of battery
Appropriateness for production runs	Good: welded connections are reliable	Good	Excellent	Excellent
Field replacement	Not possible	Possible	Possible	Not possible
Compressive force holding	Excellent	Excellent	Poor	Extremely poor
Thermal management	Not favorable	Not favorable	Favorable	Favorable
Heat dissipation	Poor	Poor	Fair	Good
Local stress	No	No	No	Yes
Safety	Good, integrated with PTC	Good, integrated with PTC	Good, integrated with PTC	Poor, no safety feature included

Cylindrical cells, compared to prismatic cells, have the advantage of the ease of manufacturing and a good mechanical stability. Cylindrical cells can be produced relatively faster than the prismatic cells, therefore, more kWh per cell can be produced in a day resulting in the lower manufacturing cost per kWh. In a battery pack, many cylindrical cells are combined in series and parallel to provide the higher voltage and capacity required for EVs and HEVs, so if one of the cells degrades and fails to work, the impact on the whole battery is low. Whereas, if a prismatic cell fails to function then the impact on the battery pack is higher (SB, n.d.).

Lithium-ion cylindrical cells are mechanically stable. They contain positive thermal coefficient switches. When excessive current is applied the polymer heats up and changes its state from a conductive to a resistive polymer. This prevents the flow of current, and acts as a short circuit protection. Once the temperature is back to normal the polymer cools down and reverts back to its conductive state (BU, 2017b). The electrodes in cylindrical cells are covered with a metal casing and are wound tightly around a central nylon mandrel. This assembly helps in minimizing the breaking of electrode material due to mechanical vibrations, thermal cycling, and mechanical expansion of the current conductors inside due to charging and discharging of the cells (SB, n.d.). Cylindrical cells also contain a pressure relief mechanism and when under high pressure the membrane seal ruptures. The pressure relief valve is connected to an electrical fuse. When an unsafe pressure builds up then it permanently opens the cell (BU, 2017b).

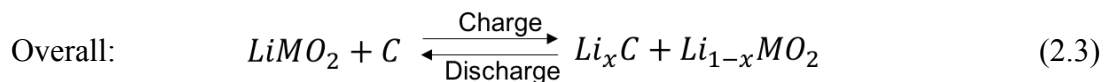
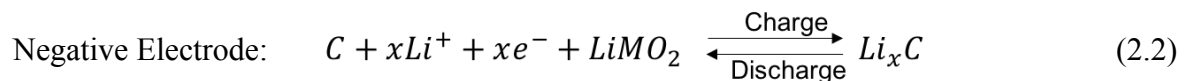
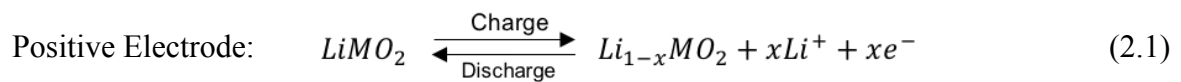
2.1.2 Li-ion Cell Chemistry

Li-ion cell contains four main components, namely, anode, cathode, electrolyte, and separator. The separator isolates the anode and cathode to prevent physical contact and short-circuit of the cell while permitting free ion flow. The material of the separator increases the cell density and electrical resistance, affecting the cell performance adversely. Therefore, the material for the separator should be carefully selected (Zhang, 2007a). Liquids electrolytes that are commercially available use microporous polyolefin materials, such as polyethylene (PE) or polypropylene (PP). The pore sizes vary from 0.03 μm to 0.1 μm and the porosity of ranges from 30% to 50% (Dahn and Ehrlich, 2011). The separator also acts as a thermal fuse. The low melting point of the PE material enables the membrane to shrink and reduce the pore size once the temperature of the cell rises to the softening point of the polymer. This restricts the flow of Li^+ ions and the reaction rate decreases. Below the thermal runaway threshold, the separator has the capability to shut down the entire reaction if the temperature rises continuously.

Currently used PE-PP bilayer separators shuts down the reaction at 130 °C and melts at 165 °C (Zhang, 2007a).

The electrolyte in a Li-ion cell is a combination and mixture of electrolyte salts and organic solvents. It provides an interface for the movement of the lithium ions associated with the redox reactions on the anode and the cathode (Dhameja, 2001). Various types of Lithium electrolyte salts are used in Li-ion cells, which include Lithium Hexafluorophosphate (LiPF₆), Lithium Triflate (LiSO₃CF₃), Lithium Tetrafluoroborate (LiBF₄), and Lithium Tris (trifluoromethane sulfonyl) methide (LiC(SO₃CF₃)₃) (Wenige et al., 1997). Organic solvents used to mix with electrolyte salts are Ethyl Carbonate (EC), Propylene Carbonate (PC), Diethyl Carbonate (DEC), and Dimethyl Carbonate (DMC). 1M LiPF₆/EC: DEC is the most commonly used electrolyte due to its highest electrical conductivity compared to other electrolyte mixtures (Berini et al., 2014; Wenige et al., 1997).

Typical chemical reactions occurring at the anode and cathode during the charging/discharging process for a Li-ion cell are shown in Equations 2.1 to 2.3 (Qu et al., 2014; Vyroubal et al., 2015) and the charge and discharge mechanism is shown in Figure 2.3. Lithium ions intercalate into solid particles of the anode and de-intercalate from solid particles at the cathode during charging. For discharging, the reactions occur in the reverse direction. Both these processes result in the heat generation within the cell.



Anode materials used in the Li-ion cells include graphite, hard carbon, meso-carbon microbeads (MCMB), graphene, lithium titanate oxide ($\text{Li}_4\text{Ti}_5\text{O}_{12}$), lithium silicide ($\text{Li}_{4.4}\text{Si}$), and lithium germanium ($\text{Li}_{4.4}\text{Ge}$) (Schalkwijk and Scrosati, 2002). Graphite is, however, the most commonly utilized material for the anode because of its high coulombic efficiencies of more than 95%, with a theoretical specific capacity of 372 mAh/g (Brodd and Kozawa, 2009).

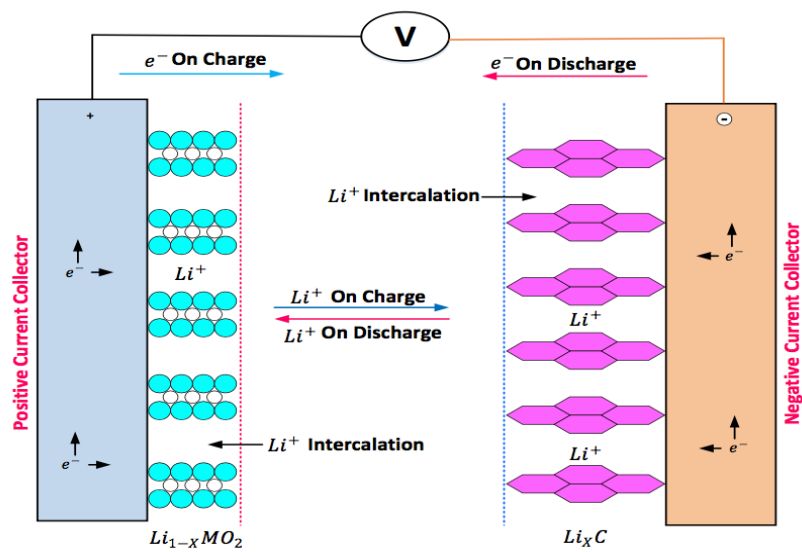


Figure 2.3: Li-ion battery charge and discharge mechanisms (Panchal, 2016).

The naming of Li-ion cells is based on the material of the cathode. Commonly used cathode materials include Lithium Cobalt Oxide (LiCoO_2), Lithium Manganese Oxide (LiMnO_4), Lithium Iron Phosphate (LiFePO_4), and Lithium Nickel Manganese Cobalt Oxide (LiNiMnCoO_2 or NMC) (Berini et al., 2014; Schalkwijk and Scrosati, 2002). A comparison of these cathode materials is provided in Table 2.3 and Figure 2.4.

Table 2.3: Specifications of commercially used Li-ion batteries (Bandhauer et al., 2011; Ohzuku and Brodd, 2007; Huat, 2014)

Specifications	LiCoO ₂ (LCO)	LiMn ₂ O ₂ (LMO)	LiFePO ₄ (LFP)	LiNiMnCoO ₂ (NMC)
Voltage (V)	3.60	3.80	3.30	3.60/3.70
Charge Limit (V)	4.20	4.20	3.60	4.20
Life Cycle	500-1000	500-1000	1000-2000	1000-2000
Specific Energy (Wh/kg)	150-190	100-135	90-120	140-180
Specific Power	1C	10C, 40C Pulse	35C Continuous	10C
Safety	Medium	Medium	High	Safer than LCO
Thermal Runaway (°C)	150	250	270	210
In Market Since	1994	1996	1999	2003
Manufacturers	Sony, Sanyo, GS Yuasa, LG Chem, Samsung, Hitachi, Toshiba	Sanyo, GS Yuasa, LG Chem, Samsung, Toshiba, Moli Energy, NEC, Hitachi	GS Yuasa, BYD, JCI/Saft, Lishen, A123, Valence	Sony, Sanyo, LG Chem, GS Yuasa, Hitachi, Samsung

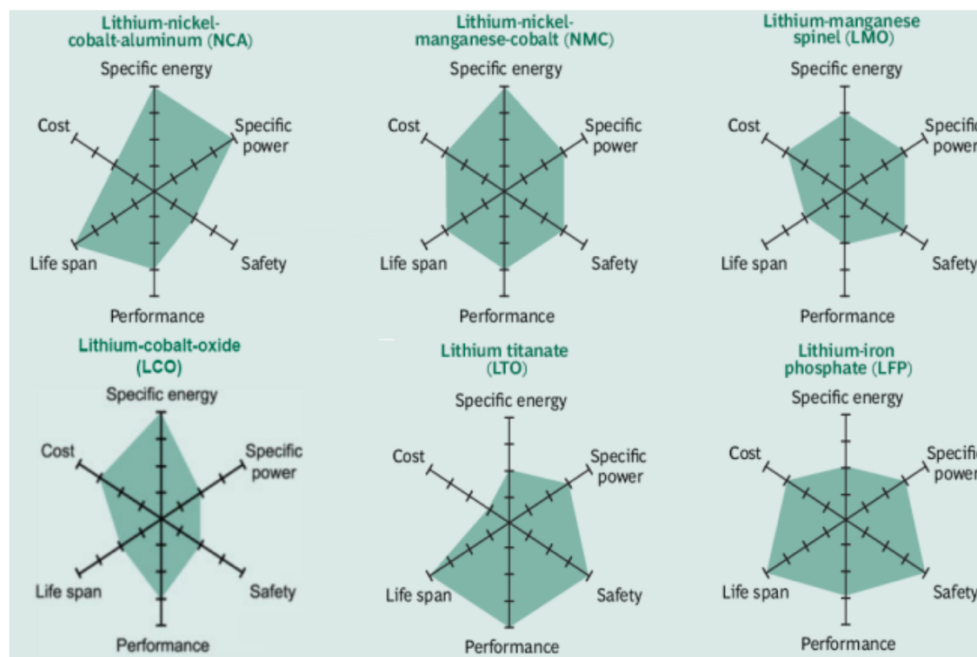


Figure 2.4: Comparison of Li-ion cell chemistries (BU, 2017c).

2.2 Heat Generation within a Cell

The heat is generated within a cell due to two processes: (1) Ohmic heating, otherwise known as the Joule's effect, due to the transfer and movement of current across the internal resistances of the cell and over potential; and (2) change in entropy from the electrochemical reactions. There is a third source of heat generation or electrical energy loss in some electrochemical pairs. This is due to the overcharging of a completely charged cell. The rate of heat generation within the Li-ion cell can be calculated using Equation 2.4 (McKinney et al., 1983; Pals and Newman, 1995; Chen and Evans, 1996; Abdul-Quadir et al., 2014a; Abdul-Quadir et al., 2014b; Drake et al., 2015).

$$\dot{Q} = I(E - V) - I \left[T \left(\frac{dE}{dT} \right) \right] \quad (2.4)$$

The first term in Equation 2.4, $I(E - V)$, represents the generation of heat due to the internal resistance (irreversible heat dissipation). The second term, $-I \left[T \left(\frac{dE}{dT} \right) \right]$, represents the reversible heat due to the changes in open circuit potentials with respect to change in temperature at the anode and the cathode. In practical applications of EVs and HEVs the reversible heat generation (second term of Equation 2.4) is smaller compared to the irreversible heat generation (first term of Equation 2.4). Therefore, heat is generated in a cell during both the charging and discharging processes (McKinney et al., 1983).

The heat generated, if not removed properly, can result in a thermal runaway of the cell, as increased temperature trigger additional exothermic reactions (Coman et al., 2016; Feng et al., 2015a; Feng et al., 2015b; Spotnitz and Franklin, 2003). These additional reactions generate more heat and further increase the temperature of the cell, creating a positive feedback mechanism which results in a sharp rise of the cell temperature. This sharp rise in temperature causes thermal runaway and can result in a complete failure of the cell accompanied by the fire

of the explosive gas release. Moreover, significant degradation of the capacity of the cell occurs by consistently operating the cell at higher and elevated temperatures ($>50\text{ }^{\circ}\text{C}$) (Ramadass et al., 2002).

Current collectors, within the cell at the anode and cathode, are responsible for additional Ohmic heating. Therefore, to account for this additional heat generation in the current collectors, Equation 2.5 was developed (Gu and Wang, 2000; Kim et al., 2009).

$$\dot{Q} = I(E - V) - I \left[T \left(\frac{dE}{dT} \right) \right] + A_p R_p I_p^2 + A_n R_n I_n^2 \quad (2.5)$$

Due to the generation of the heat during the charging the discharging processes, thermal management systems of the batteries are required. A battery pack without a thermal management system can result in heat accumulation which may overheat the battery pack. This can become a serious safety issue and in some extreme cases can cause the battery pack to explode. In addition to that, once the temperature increases above the optimum range of operating temperature, the degradation of the cells accelerate which results in thermal runaway, reduced efficiency of the battery pack and reduction of the life of the batteries (Yang et al., 2016). Thermal management of batteries is discussed in Section 2.3.

2.3 Thermal Management of Batteries

To perform effectively, Li-ion batteries must operate within particular temperature and thermal specifications, as stated earlier. A thermal management system (TMS) is required for battery packs to maintain the temperature of the cells within the operating limit of $0\text{ }^{\circ}\text{C}$ to $40\text{ }^{\circ}\text{C}$ (Li et al., 2013) and to increase the temperature uniformity within the cell and the battery pack. The TMS of a battery pack is divided into three separate categories, namely, liquid cooling (Jarrett and Kim, 2011, 2014; Panchal et al., 2015; Park and Jung, 2013), phase change material (PCM) cooling (Ling et al., 2014, 2015; Somasundaram et al., 2012) and air cooling (Choi and Kang,

2014; He et al., 2014; Yang et al., 2015; Yu et al., 2014). A summary of the comparison between different TMS is provided in Table 2.4.

Table 2.4: Comparison of battery TMS (Rao and Wang, 2011)

Parameters	Forced Air	Liquid	Heat Pipe	PCM	Thermoelectric	Cold Plate
Ease of Use	Easy	Difficult	Moderate	Easy	Moderate	Moderate
Efficiency	Low	High	High	High	Low	Medium
Temperature Drop	Small	Large	Large	Large	Medium	Medium
Temperature Uniformity	Uneven	Even	Moderate	Even	Moderate	Moderate
Maintenance	Easy	Difficult	Moderate	Easy	Difficult	Moderate
Life	≥20 years	3-5 years	≥20 years	≥20 years	1-3 years	≥20 years
Initial Cost	Low	High	High	Moderate	High	High
Annual Cost	Low	High	Moderate	Low	High	Moderate

According to Chen et al. (2016) when considering the thermal management system of the battery packs, trade-off has to be made amongst many parameters that include the cost, complexity, weight, cooling effects, temperature uniformity, and parasitic power. The authors conducted a comparative study of the different cooling methods that included air cooling, direct liquid cooling, indirect liquid cooling, and fin cooling. An electrochemical thermal model was developed using ANSYS Fluent. The results of their study concluded that the indirect cooling method resulted in the lowest maximum temperature increase. The fin cooling added 40% extra weight to the cell (the highest weight when compared to other methods of cooling at the same volume). Air cooling method required 2 to 3 times more energy than other methods in order to maintain the same average temperature obtained from other methods. A brief review of the different cooling methods is reported subsequently.

2.3.1 Liquid Cooling

Liquid cooled TMS is a complex system compared to PCM cooling and air cooling. In liquid cooling the heat is transferred from the surface of the battery to the liquid with discrete tubing

around the batteries; a jacket around the batteries; submerging cells into dielectric liquids such as silicone based liquids or mineral oils for direct contact cooling methods to avoid short circuiting; or by placing the batteries on cold plates (heat sinks) (Rao and Wang, 2011). Compared to air cooling the performance of the direct cooling method is higher because of its higher thermal conductivity, however, the higher viscosity of dielectric oils restricts the flow rates and require higher pumping power. Pesaran et al. (1999) and Pesaran (2002) compared the performances of the liquid cooled TMS and air cooled TMS by conducting experiments and suggested that even though liquid cooling is more complicated than air cooling, however, it is highly efficient for cooling the batteries. For HEVs air cooling is adequate enough but for EVs liquid cooling may be required. Karimi and Dehghen (2014) also compared liquid cooling with air cooling using LiCoO₂ prismatic cells. Two different types of battery configurations were modeled; U-type configuration, in which the cooling medium enters and exits at the same side of the battery pack and Z-type configuration, in which the cooling medium enters and exits from the opposite ends of the battery pack. The cooling medium used was air and silicon oil for air cooling and liquid cooling, respectively. Results showed that Z-type configuration results in a better temperature uniformity of the battery pack for both air and liquid cooling. Additionally, silicon oil provides a temperature deviation of 0.15 °C whereas, air provides a temperature deviation of 7.33 °C. However, it was concluded that the drawback for improved thermal performance of the liquid cooled pack is the higher pumping power requirements of silicon oil due to its high viscosity. When compared with air the thermal conductivities of liquids are higher, an example is the thermal conductivity of propylene glycol, used in the battery packs of Tesla vehicles (IE, 2015), is 0.147 W/mK and for air it is 0.0259 W/mK at 300 K (ETB, 2017a; ETB, 2017b).

Heat pipes are also being considered for liquid cooling methods as they make use of change of phase heat transfer. The heat pipe removes the heat through evaporation and condensation of

the cooling fluid in an endless cycle (Rao and Wang, 2011). Wu et al. (2002) attached two heat pipes with an aluminum fin to cylindrical 40110 battery walls. The experimental and simulations results showed a significant cooling of the battery pack as the maximum temperature was restricted to 32 °C with metallic aluminum fins.

2.3.2 Phase Change Material Cooling

Phase Change Materials (PCMs), otherwise called thermal storage materials, utilize chemical bonds to store and release heat. The heat is absorbed into the PCMs and the aggregate state changes from solid to liquid (Al-Hallaj et al., 2005; Demirbas, 2006). Paraffin wax is a commonly used PCM material. One of the benefits of using PCMs is that they improve power availability and wipe out the need for auxiliary cooling systems such as pumps and fans. Batteries usually generate a large amount of heat during the discharging process when integrated between the cells in a module. PCMs with the high latent heat of fusion are often used to overcome this problem and can prevent a sharp rise in battery temperature and ensure that the battery operates at its optimum temperature. By infusing the PCM in a graphite matrix, the rate of heat removal can be increased drastically as it has a higher thermal conductivity (Al-Hallaj et al., 2005; Demirbas, 2006). A battery pack equipped with PCM offers benefits such as reduced peak temperature, better temperature uniformity, and reduced volume of the overall thermal management system. However, drawbacks include added weight, heat accumulation at the center of the battery pack, and undesired thermal inertia (Al-Hallaj and Selman, 2002; Alrashdan et al., 2010; Johnson et al., 2001; Kizilel et al., 2008; Rao et al., 2011; Sabbah et al., 2008).

A PCM reduces the peak temperature of the battery at a high current rate of charging and discharging. Additionally, compared to air cooling, it is much more effective in retaining large amounts of heat released during thermal runaway of the battery. Heat from the cell transfers

rather rapidly through the highly conductive carbon matrix while maintaining the uniformity of cell temperature (Johnson et al., 2001). A PCM Li-ion battery pack comprises a block made of PCM material with holes in it to fit in the cylindrical battery cells.

A lumped capacitance model was used by Kim et al. (2008) for a forced air cooling ($h = 15 \text{ W/m}^2\text{K}$) thermal management system in order to benchmark the performance of a PCM for a Li-ion battery pack under 40 A single discharge for 9 minutes. The low peak temperature of the battery pack resulted from the large thermal mass of the PCM. When the PCM reaches its melting point at a high temperature of 40 °C, it converts the heat generated from the battery into latent heat by melting the wax in the matrix and preventing the temperature from rising further. Therefore, the PCM module has the most minimal temperature rise and the slowest cool-down since the stored heat is slowly released into the environment. Currently, PCM TMS battery systems are still under development for commercial EVs and HEVs applications.

2.3.3 Air Cooling

Using air as a heat transfer medium is the simplest approach. Air cooling is divided into two categories, natural air cooling and forced air cooling, both of which were investigated by Li et al. (2013). The authors used a LiMn_2O_4 battery to compare the forced air cooling with natural air convection. Their findings concluded that the maximum temperature of the cell reduced by 3.5 °C when compared to natural convection, therefore, forced air cooling was more effective.

In addition, a parametric study on the LiFePO_4 cylindrical cells was performed by Zhao et al. (2015) and the effects of various ventilation types and forced air velocities were investigated. The spacing between adjacent cells and the effects of environmental temperature and inlet air temperature were also studied. The results of their study showed that with the increase in air flow speed the local temperature differences initially increased and then decreased.

Furthermore, a simulation was conducted by the authors to examine the effect of the cooling of the battery pack when there was a counter-flow of air between adjacent rows of the cells. It was concluded that counter-flow was not an effective cooling method. When the ambient temperature is high and the spacing between cell is reduced with an increase in cell diameter, the battery pack is susceptible to thermal runaway. For an 18650 battery pack, the optimum values of S/D (the ratio of the spacing distance between the adjacent to the cell diameter) is between 0.3 and 0.35.

Various arrangements of LiNiMnCoO₂ (18650) cylindrical cells were also explored by Wang et al. (2014) which included 1×24, 3×8, and 5×5 arrays of rectangular structures, 19 cell hexagonal structure, and 28 cell circular structure. For every arrangement, air cooling strategies were investigated by placing the fan and exhaust at different locations of the battery pack. Three-dimensional CFD simulations were conducted and using the thermal insulation experiment the heat generation rate was obtained for the cell. The results of their study concluded that the cooling ability of the thermal management system is depended on the length and cross-sectional area of the airflow path, the temperature of the cooling air, and the velocity of the cooling air. The most effective cooling was achieved when the fan was located at the top of the battery pack regardless of the arrangement and structures of the cells. Comparing the various arrangements of the cells, the 5×5 cubic cell structure, with the inlet placed at the top of the pack and the exhaust at the bottom of the pack, had the best thermal performance in terms of cooling capability and cost. However, the hexagonal structure with 19 cells was considered the most suitable option in terms of the utilization of the space and cooling effectiveness. Finally, the optimum cell spacing between the adjacent cells in 5×5 cubic structure, with an air velocity of 1 m/s, is 1 mm. Based on this study Wang et al. (2015) also investigated the effects of inlet air temperature on the cooling of the cells in the 5×5 cubic

structure. The authors concluded that the temperature of the inlet air should lie within the range of 20°C and 35°C in order to effectively cool the cells. If higher ambient temperatures of the inlet air are used, then the velocity of the air should be increased to achieve effective cooling. Without the forced air cooling, the highest temperature areas are located in the middle of the battery due to the mutual heating among cells. On the contrary when the air is blown through the battery pack then the outermost cells experience the highest temperature because of the slower air velocity near the edges compared to the center of the battery pack.

The effects of ambient temperature on the temperature uniformity were also studied by Cho et al. (2014). It was concluded that the temperature difference between the cells increased at low ambient temperatures but the temperature difference between the cells reduced at high ambient temperatures. It was also observed that irrespective of the ambient temperature, the cells closer to the inlet had low maximum temperatures compared to the cells towards the outlet.

In another study, Yang et al. (2015) investigated aligned and staggered cell arrangements using LiFePO₄ cylindrical cells. The focus was placed on determining the optimum spacing values between the cells in the longitudinal and transverse directions in a cylindrical battery pack of 10×6 arrangement. It was concluded that the aligned arrangement is better in terms of uniform cooling of the cells when compared to the staggered arrangement. The optimum distances between the cells should be 34 mm in the longitudinal direction and 32 mm in the transverse direction. Additionally, by increasing the distances in the transverse direction the temperature uniformity is improved and the required power is reduced for both the aligned and staggered arrangements, however, this results in an increase of the battery temperature.

More recently, Yang et al. (2016) investigated the axial air flow with 32 cylindrical cells in the battery pack. The thermal model was developed and coupled with the fluid flow governing equations to conduct the simulation. The heat generation rate was obtained by developing a

user defined function program based on the pseudo-2D model for Li-ion cells. The results of their study showed that by increasing the radial interval between the cells from 2 mm to 10 mm the temperature uniformity increased by about 0.8 °C, while the average temperature of the battery pack increased by 0.56 °C. Also by quintupling the air flux the maximum temperature of the battery pack reduced to ~33.5 °C, a decrease of 5.3 °C when compared to single air flux and the minimum temperature reduced to ~31.5 °C, a decrease of 4.1 °C, resulting in the decrease in temperature difference by 1.2 °C.

In order to investigate the effect of the flow circuit, Saw et al. (2016) developed a battery pack based on the concept of air entering from the top of the pack and exhausting to the bottom for Lithium Iron Phosphate (LFP) 38120 cylindrical cells. It was concluded based on the results that the heat accumulation takes places at the center of the battery pack resulting in the highest temperatures of the cell. It was also shown that the front end of the battery pack also exhibited the highest temperatures because of lack of air flow.

Mahamud and Park (2011) investigated a reciprocating air flow inside the battery pack using LiMn_2O_4 cells and results showed that the reciprocating air flow improves the uniformity in the battery pack, and reduces the temperature difference between cells by about 4 °C. Also, the maximum cell temperature was reduced by 1.5 °C for a reciprocating period of 120 seconds.

Furthermore, a parametric optimization study was conducted by Liu et al. (2015), using a Sony US-18650 cell, on a reciprocating air flow system. In this study, a numerical analysis was conducted on a single row of cells and symmetry applied on both sides of the row. Based on the range of values of the maximum temperature, minimum temperature, and the temperature difference, it was concluded that 6 ms^{-1} of air velocity, 283.15 K inlet temperature and a reciprocation period of 67.5 s were the most optimal factors. Therefore, the temperature variation between the maximum and minimum temperatures was about 3.76 K.

Reciprocating flow was also investigated by He et al. (2015) using A123 26650 cylindrical cells and confirms the studies done by Mahamud and Park (2011) and Liu et al. (2015), that due to the reciprocation the temperature uniformity improves, temperature fluctuations of the cells over time reduces and the total amount of cooling required also reduces.

Finally, a study was conducted on prismatic cells' battery pack by Yu et al. (2014), in which a second inlet fan was added based on which jet inlet was developed. The air from this jet inlet was introduced in the middle of the of the battery pack where heat accumulation occurred. This jet inlet reduced the maximum temperature of the cell from 42.3 to 33.1 °C and maintained the temperature difference for each cell to within 5 °C.

2.3.4 Vortex Generators

Vortex generation has emerged as one of the most promising methods to enhance the convection of heat in air-cooling applications. In this technique, a passive flow manipulator, known as vortex generator (VG), is mounted onto a surface. As the incoming flow of air encounters the vortex generator, the adverse pressure gradient causes the boundary layer to separate along the leading edge and form a vortex system (He et al., 2014b). This is shown in Figure 2.5. The vortices improve heat convection by increased mixing or unsteadiness and flow destabilization (He et al., 2014b).

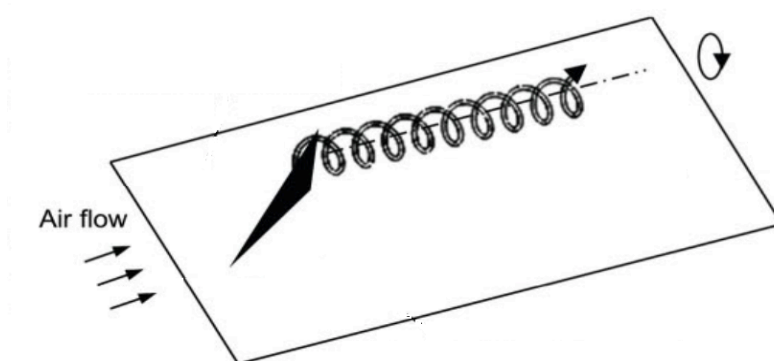


Figure 2.5: Schematic of longitudinal vortices generated by delta winglet vortex generator (modified from He et al., 2014b)

There are various types of vortex generators used to increase the heat transfer through convection, however, the basic vortex generator forms include delta wing, rectangular wing, delta winglet, and rectangular winglet vortex generators (Althaher et al., 2012; Chu et al., 2009). The different types of VGs are shown in Figure 2.6.

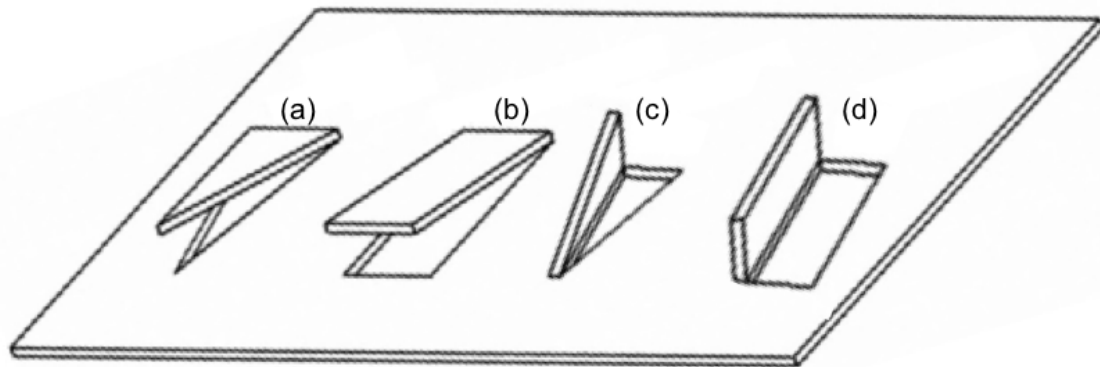


Figure 2.6: Basic vortex generator forms: (a) delta wing, (b) rectangular wing, (c) delta winglet, and (d) rectangular winglet vortex generators (modified from Chu et al., 2009).

Currently, there are no reported studies that involve the incorporation of vortex generators in a battery pack for cylindrical Li-ion cells. Therefore, for this study inspiration has been taken from the studies that include the addition of vortex generators to enhance heat convection in heat exchangers and rectangular ducts.

Based on the experimental studies conducted in ducts by Eaton (1994) and Tiggelback et al. (1994), it was reported that delta winglet vortex generators were preferred for heat transfer enhancement applications. Additionally, it was reported by Tiggelback et al. (1994) that the delta winglet vortex generator causes a lower pressure drop and provides a higher heat transfer rate than the rectangular wing and rectangular winglet vortex generators. It was also reported by Wang et al. (2002) that the delta winglet vortex generators showed more intense vertical motion and flow unsteadiness. Furthermore, it was also reported by Fiebeg et al. (1986) and Fiebeg (1998) that delta winglet vortex generator had the best performance when compared with a delta wing and rectangular winglet vortex generators. Fiebig (1995) in his review paper

also concluded that at Reynolds number less than 5000, rectangular type vortex generators were more effective in enhancing heat transfer, whereas, at higher Reynolds number, delta type vortex generators were more effective. Additionally, the studies conducted by Biswas et al. (1996), Jain et al. (2003), and Tian et al. (2009) also conclude that delta winglet vortex generators are better at removing heat with reduced drag. Therefore, in this study, a focus is placed on the delta winglet vortex generators.

Studies were also conducted for heat exchangers by Zhang et al. (2016) and He et al. (2014b) on the attack angles of delta winglet vortex generators and it was found that vortex generators placed at 30° angles provide the highest convection of heat. Additionally, Lei et al. (2010), found that 20° of attack angle for the delta winglet provided the best performance.

2.4 Gaps in the Literature

The literature review provided above can be summarized as follows. Reciprocating air flow systems have shown promising results as discussed in Section 2.3.3. However, reciprocating air flow systems are considered active systems as they require timing valves to change the direction and the flow of the air, thereby increasing the power requirement and complexity of the system.

Additionally, the temperature uniformity at the cell and pack levels, has a significant effect on the performance of the cells and the battery pack as stated earlier. The self-discharge rates of the cells are dependent on the temperature of the cell and if there are significant differences in temperature variations, the discharge rates of each cell will also vary significantly. This variation results in the different values of state of charge (SOC) amongst all the cells. In a battery pack, the lowest SOC cell determines the discharge rate of the battery pack and the lower end of the usable energy rate. On the other hand, the highest SOC cell determines the upper end of the usable energy range (Kuper et al., 2009). Non-uniform discharge rates result

in electrically unbalanced cells and a degradation of the performance of the battery pack (Pesaran, 2002; Saw et al., 2016). Therefore, the desired temperature uniformity within each cell and within the battery pack is less than 5 °C (Kuper et al., 2009; Liu et al., 2015; Pesaran, 2002; Saw et al., 2016).

There have been very limited reported studies on the Li-ion 18650 cells that examine temperature uniformity in the battery packs, especially for non-active systems. Moreover, the incorporation of jet inlets and vortex generators in the battery pack for cylindrical cells have not been studied at all. Therefore, a forced air cooling system is required that is simple, eliminates the power requirement of reciprocating valves and simultaneously reduces the non-uniformity of temperature within the battery pack. There is also the need to examine the temperatures at different locations of a battery pack and also the variation of temperature between all the cells at those locations. This will provide some insight in the temperature differences across the battery pack as well as within individual cells.

2.5 Motivation and Objectives

Li-ion battery is the most promising battery for EVs and HEVs, but it has problems associated with thermal management of cylindrical air-cooled batteries. This is due to the high operating temperatures and temperature non-uniformity within the battery pack as well as within each cell. Therefore, it is important to conduct a research into the thermal performance of the battery pack. In order to perform efficiently and effectively, Li-ion batteries require a specific temperature and thermal specifications. As the temperature of the batteries increases beyond the optimum operating range of 0 to 40 °C (Li et al., 2013), the batteries can become a safety hazard and in some highly extreme cases cause the battery pack to explode. In addition, the degradation of the cells accelerates once the temperature increases and moves out of the operating range of the cells, which can result in thermal runaway, reduced efficiency of the

battery pack and reduction of the life of the batteries (Yang et al., 2016). Moreover, the performance of the cells and battery pack is significantly affected by the uniformity of the temperature of a single cell and the battery pack. Since the self-discharge rates of the cells depend on the temperature of the cell, therefore if the differences in temperature vary significantly, the discharge rates of the cell will also vary accordingly. In a battery pack, the discharge rate of the battery pack and the lower end of the usable energy rate is determined by the lowest state of charge (SOC) cell whereas, the upper end of the usable energy range is determined by the highest SOC cell (Kuper et al., 2009). Non-uniform discharge rates result in electrically unbalanced cells and a degradation of the performance of the battery pack (Pesaran, 2002; Saw et al., 2016).

Therefore, the main objective of this research is to develop and analyze concepts to improve the cooling of the cells and the battery pack and to improve temperature uniformity at the pack and cell levels for cylindrical cells. Based on this main objective, the specific objectives of this thesis are as follows:

1. Develop new battery pack concepts to improve cooling and temperature uniformity at the pack and cell levels.
2. Incorporate an inlet plenum to improve the concepts to be developed in (1), and conduct a parametric study to find the optimum location of the inlet plenum.
3. Conduct a Reynolds number study and examine the effects of mass flow rate in order to reduce fan power.
4. Investigate the application of flow control techniques including jet inlets and vortex generators to further improve thermal management.

2.6 Thesis Structure

This thesis is organized into 5 chapters as follows:

Chapter 1 provides an introductory passage for this thesis. It gives an overview of the current problems related to the mass adoption of the electric and hybrid electric vehicles.

Chapter 2 presents the background and the literature review related to electric batteries. It provides the necessary definitions for technical terms related to the electric batteries in order to understand this thesis. In this chapter, the different types and chemistries of lithium ion cells are discussed and the heat generation within a cell is explained. Additionally, the different types of thermal management systems for battery packs with cylindrical cells are examined with a focus on the air cooling systems. Finally, the gaps in the literature are presented and the motivation and objectives of this research are stated.

Chapter 3 introduces the experimental and numerical procedures. It provides the different battery pack configurations used to achieve the desired results. The experimental setups are given that explain the equipment that was used, followed by the procedures adopted to conduct successful experiments. Two different kinds of experiments were undertaken. The first experiment was done to get the temperature variation profiles for different cells in the battery pack, which was required to validate the numerical simulations and the second experiment provided the heat generation rates of the cell without any cooling. An uncertainty analysis is also provided in order to account for the errors and uncertainties in the experimental equipment. Finally, a numerical modeling is presented that includes the flow models, energy equations, mesh generation and the boundary conditions used for all the tests.

Chapter 4 presents the results and discussions that were obtained from the experiments and numerical simulations. The first part provides an analysis for the different configurations of the

inlet plenum and cell orientations. The second part gives an analysis of the parametric study conducted to determine the optimum location of the inlet plenum and the Reynolds number study to determine the optimum inlet velocity required for the thermal management system. The third part provides an analysis on the addition of jet inlets and vortex generators. Finally, the last part compares and analyzes the jet inlets and vortex generators when used without the inlet plenum on the basic battery pack.

Chapter 5 presents the summary of results and conclusions, contributions and recommendations for future work.

Chapter 3: Experimental and Numerical Procedures

This chapter presents the experimental and numerical techniques. It gives the distinctive battery pack configurations used to accomplish the coveted outcomes. The experimental setups are given that clarify the types of equipment that were utilized, followed by the procedures adopted to conduct successful experiments. Two different types of experiments were undertaken. The main experiment was done to get the temperature variation profiles for various cells in the battery pack, which was required to approve the numerical simulations and the second experiment gave the heat generation rates of the cell without any cooling. An uncertainty analysis is conducted to record the errors and uncertainties in the experimental equipment. Finally, a numerical modeling is presented that includes the flow models, energy equations, mesh generation and the boundary conditions used for all the tests.

3.1 Battery Pack Configurations

To solve the problem of non-uniform cooling of the cells, a simple battery pack was developed, which consisted of 32 commercial Li-ion 18650 cells (Samsung INR18650-25R). The specifications of the cells are summarized in Table 3.1.

Table 3.1: Samsung INR18650-25R cell specifications (SSDICO., 2014)

Parameters	Specifications
Nominal discharge capacity (mAh)	2,500
Nominal voltage (V)	3.6
Standard charge (A)	1.25 A, (0.125 A cut-off)
Maximum continuous discharge (A)	20
Discharge cut-off voltage (V)	2.5
Cell weight (g)	45
Cell height (mm)	65
Cell diameter (mm)	18
Cathode material	LiNiMnCoO ₂
Anode material	Graphite

3.1.1 Study of Inlet Plenum and Cell Orientations

Three different battery pack configurations were used to investigate the different orientations of the cells and the results are compared with a baseline battery pack. The battery packs consist of a cell holder onto which the cells are placed. The inlet is placed at the front of the cells and the outlet is placed at the bottom of the pack, for all the configurations. In addition, an inlet plenum is added to the baseline configuration, in order to develop Case A configuration, shown in Figure 3.1a. The airflow is separated from the compartment of the cells and inlet plenum by a thin separating plate. In addition, the volume of the inlet plenum reduces along the length of the battery pack which acts as a nozzle and accelerates the airflow into the main compartment. Based on this dynamics two more configurations, namely Case B and Case C, were developed and are shown in Figure 3.1b and Figure 3.1c, respectively. For comparison, a baseline configuration (Case D) without the inlet plenum was used as shown in Figure 3.1d.

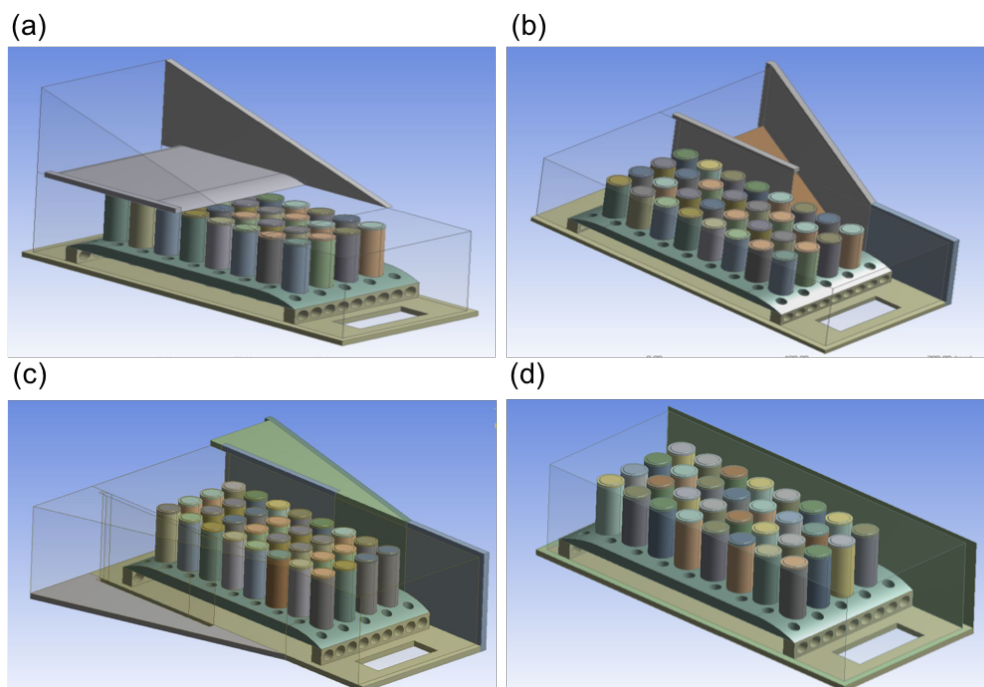


Figure 3.1: Computer aided design (CAD) models of (a) Case A, (b) Case B, (c) Case C and (d) Baseline battery pack (Case D)

3.1.2 Parametric Study of Case A

The major dimensions of Case A configuration and the arrangement of cells and the cell numbers for all the configurations are shown in Figure 3.2. In this study, the effects of the change in the length of the separating plate were studied in order to determine the optimum location to inject the airflow from the plenum into the pack. Therefore, the length of the separating plate was varied in five test configurations and the cooling and temperature uniformity were examined. The test parameters for these five tests are provided in Table 3.2.

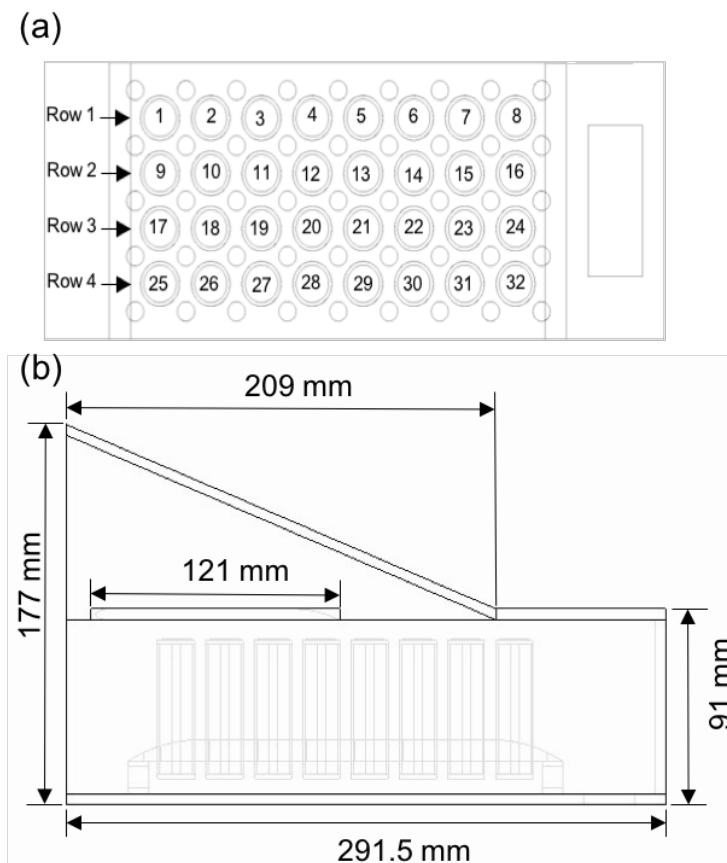


Figure 3.2: Schematics of (a) Arrangement of cells and (b) Case A battery pack.

Additionally, the effects of the length of the nozzle slit were studied to determine the optimum size of the outlet of inlet plenum (nozzle slit). For this, the length of the nozzle slit was varied from 88 mm to 41 mm in test number 1, 6 and 7, provided in Table 3.2.

Table 3.2: Lengths of separating plate and nozzle slit for different test numbers.

Test Number	1	2	3	4	5	6	7
Length of Separating Plate (mm)	121	97.5	74	50.5	0	121	121
Length of Nozzle Slit (mm)	88	88	88	88	88	64.5	41

3.1.3 Reynolds Number Study of Case A

Furthermore, there was the need to determine the inlet velocity which provides a compromise between the velocity at the inlet and the temperature uniformity and cooling of the battery pack. For this, a Reynolds number study was carried out. The Reynolds number is calculated using Equation 3.1 (Saw et al., 2016). The diameter of the cell was selected as the characteristic length for this study.

$$Re = \frac{\rho v D}{\mu} \quad (3.1)$$

Where; ρ is the density of air, v is the velocity of air at inlet, D is the diameter of the cell and μ is the viscosity of air. The parameters used for this study is provided in Table 3.3.

Table 3.3: Parameters and test numbers for the Reynolds number study.

Test Number	8	9	10	11	12	13
Reynolds Number	2430	4252	7440	13021	22786	39876
Inlet Velocity (m/s)	2.0	3.5	6.0	10.6	18.5	32.4
Mass Flow Rate (g/s)	44.8	78.3	137.1	239.9	419.9	734.8

3.1.4 Jet Inlet and Multiple Vortex Generator Study for Case A

In addition to the inlet plenum positioned at the top of the battery pack, jet inlets were added to the sides of the battery pack (Case A1), as presented in Figure 3.3b. As shown in Figure 3.2a, the air enters from the inlet plenum after the fourth column of cells. Therefore, the air from the jet inlet was introduced in the spacing between the second and the third column of cells, as shown in Figure 3.3b. The jet changes the airflow dynamics and significantly minimizes the problem of recirculation and dead air regions between the adjacent cells.

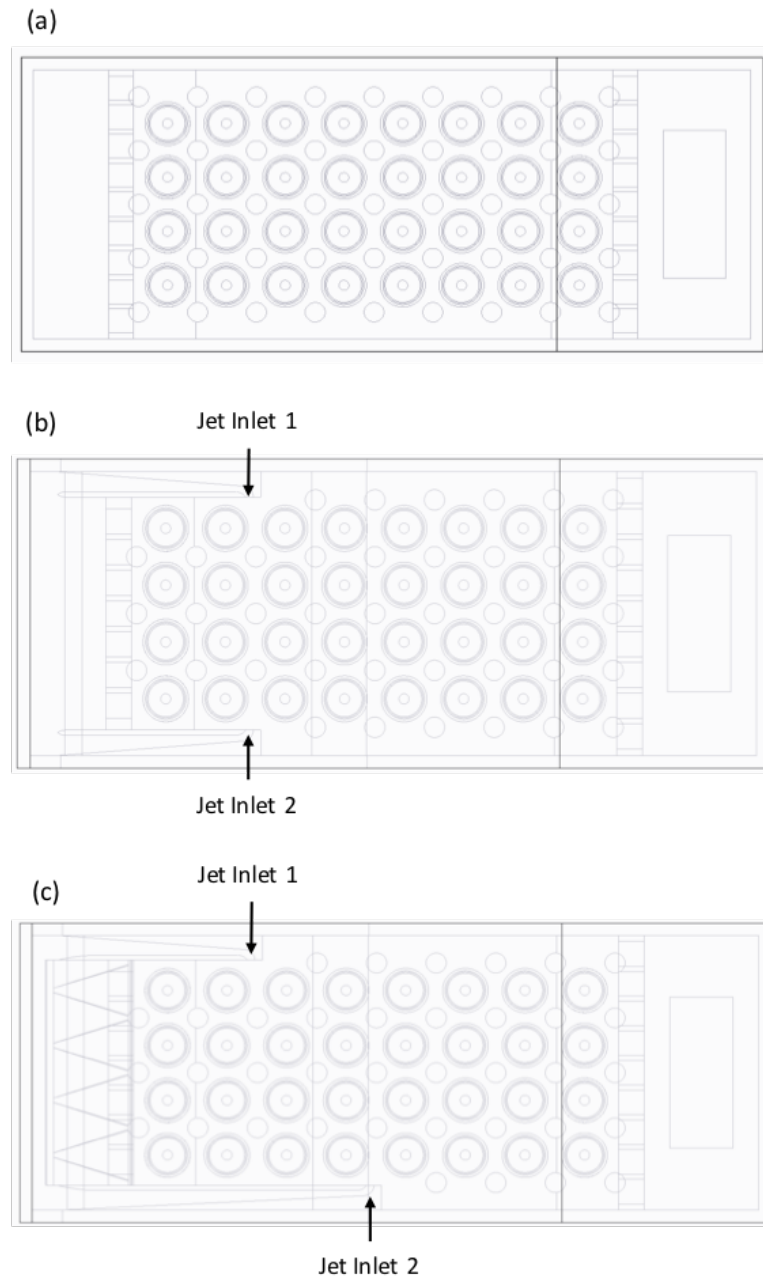


Figure 3.3: Plan view of schematics of (a) Case A, (b) Case A1, and (c) Case A3.

In order to increase mixing within the battery pack, a vortex generator was developed. Multiple delta winglet vortex generators were placed onto a thin plate. To increase the number of vortices generated the delta winglet vortex generators were mirrored to the bottom of the plate as well. This developed vortex generator is known as the delta winglet multiple vortex generator (DW-MVG) and is shown in Figure 3.4. For this study, Case A2 configuration was

developed in which, two DW-MVGs were placed at the front of the cells near the inlet as shown in Figure 3.4e and 3.4f.

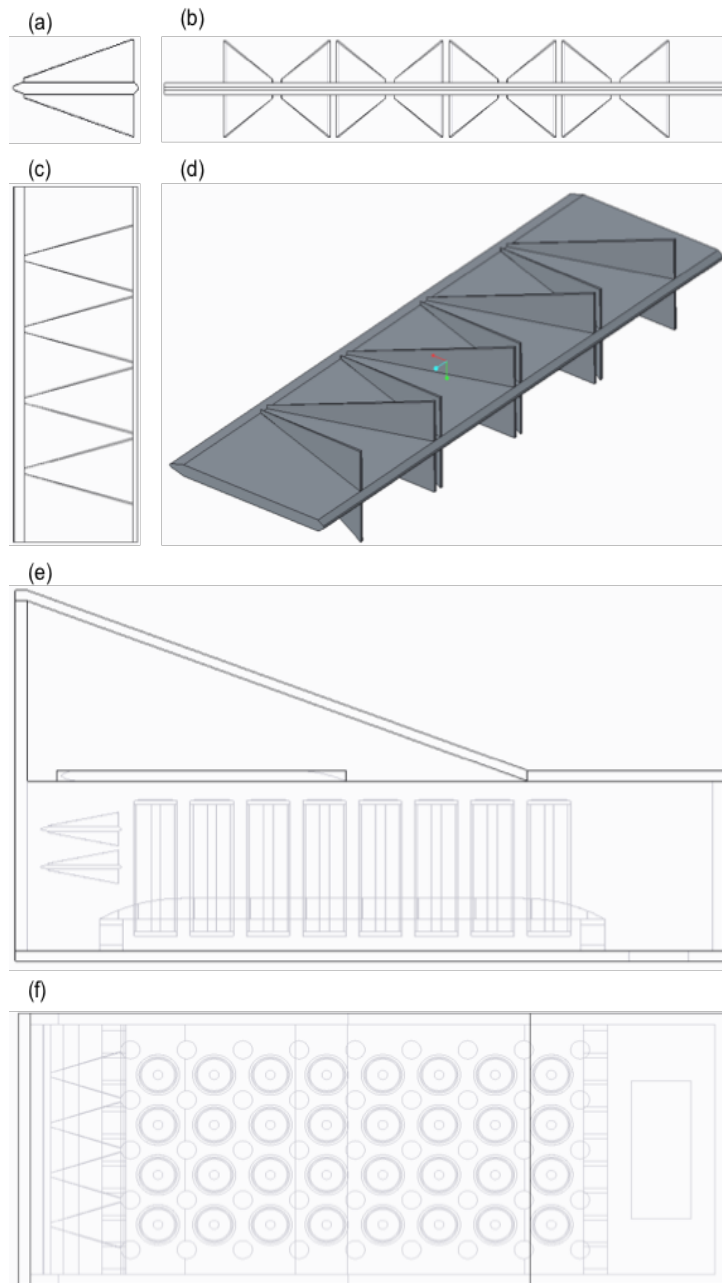


Figure 3.4: Schematic of Case A2; (a) Side view of MVG, (b) Front view of MVG, (c) Plan view of MVG, (d) CAD model of MVG, (e) Side view of Case A2 configuration and (f) Plan view.

Based on the studies by He et al. (2014b), Zhang et al. (2016), and Lei et al. (2010), an attempt was made to maximize the angle of the vortex generator. However, due to the limitations of the dimension of the battery pack, the spacing between the adjacent cells and the incorporation

of multiple vortex generators on a single plate, the maximum angle achieved was 17 degrees. Additionally, the height of a single vortex generator was set to 7 mm. This value was dependent on the battery pack dimension, cell dimensions, mirroring option to increase of amount vortices generated and incorporation of two DW-MVGs in the battery pack.

A combination of DW-MVGs and Jet Inlets were also investigated. Case A3 configuration was developed in which, the jet inlets and DW-MVGs were added to the same configuration and is presented in Figure 3.3c. However, in this configuration, the air from jet inlet 1 enters between the second and third column of cells and the air from the jet inlet 2 enters between the fourth and the fifth columns in order to enhance the turbulence across the whole battery pack.

3.1.5 Jet Inlet and Multiple Vortex Generator Study for Baseline (Case D)

For this study, 4 additional configurations were developed. Case D1 incorporates jet inlets on both sides of the battery pack with the goal of changing the airflow dynamics and minimizing the problem of recirculation and dead air regions between the adjacent cells. Similar to Case A3, the arrangement, as shown in Figure 3.5a, is that air from the jet inlet 1 enters between the 2nd and 3rd column of cells and the air from the jet inlet 2 enters between the 4th and the 5th columns. Moreover, two DW-MVGs were incorporated into Case D1 in front of the cells.

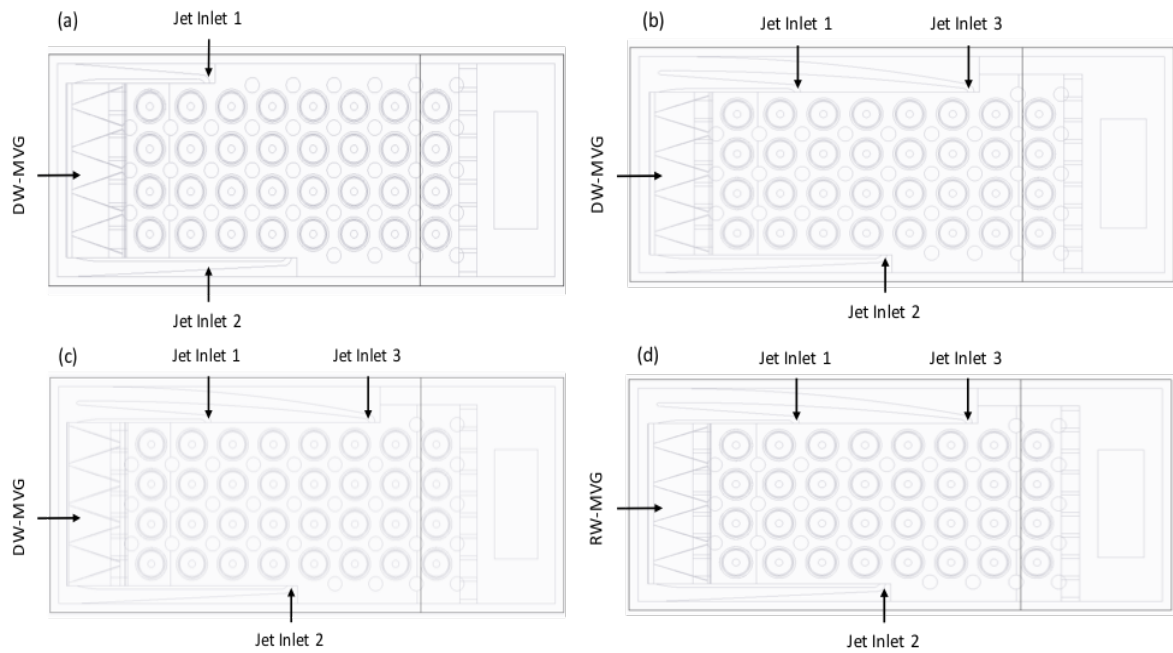


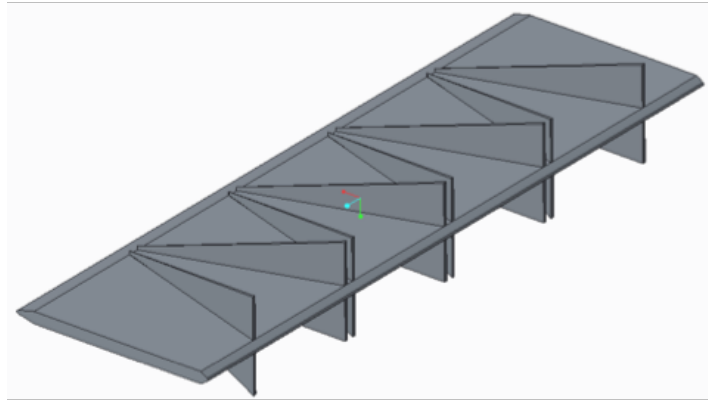
Figure 3.5: Plan views of schematic of (a) Case D1, (b) Case D2, (c) Case D3 and (d) Case D4.

Case D2 is modifications of Case D1 by the addition of a third jet inlet shown in Figure 3.5b. In order to enhance the turbulence across the whole battery pack, the air from jet inlet 3 enters between the 6th and the 7th columns of the cells. The width of the battery pack had to be increased by 10 mm (from 121 mm to 131 mm) to incorporate the 3rd jet inlet.

Furthermore, Case D3 was developed to study the placement and the position of the DW-MVG by modifying Case D2 (vortex generator placement test). In previous configurations, the DW-MVG was placed in between the cell rows. However, in Case D3, the position of the DW-MVG has been shifted towards the center of the cells as shown in Figure 3.5c.

Finally, in order to the study the types of vortex generators, the second type of multiple vortex generators (MVG) was developed, named as rectangular winglet multiple vortex generators (RW-MVG). In RW-MVG the delta winglet vortex generators are replaced with the rectangular winglet vortex generators as shown in Figure 3.6b. To incorporate RW-MVG, Case D2 was modified by changing the DW-MVG to RW-MVG. This modified configuration is named as Case D4 and is shown in Figure 3.5d.

(a)



(b)

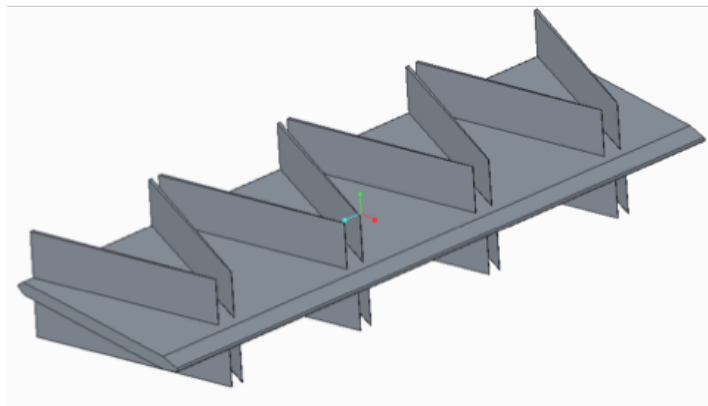


Figure 3.6: CAD model of (a) delta winglet multiple vortex generators and (b) rectangular winglet multiple vortex generator.

3.2 Experimental Setup

Numerical simulations were validated with experimental results. The experimental setup is shown in Figure 3.7.

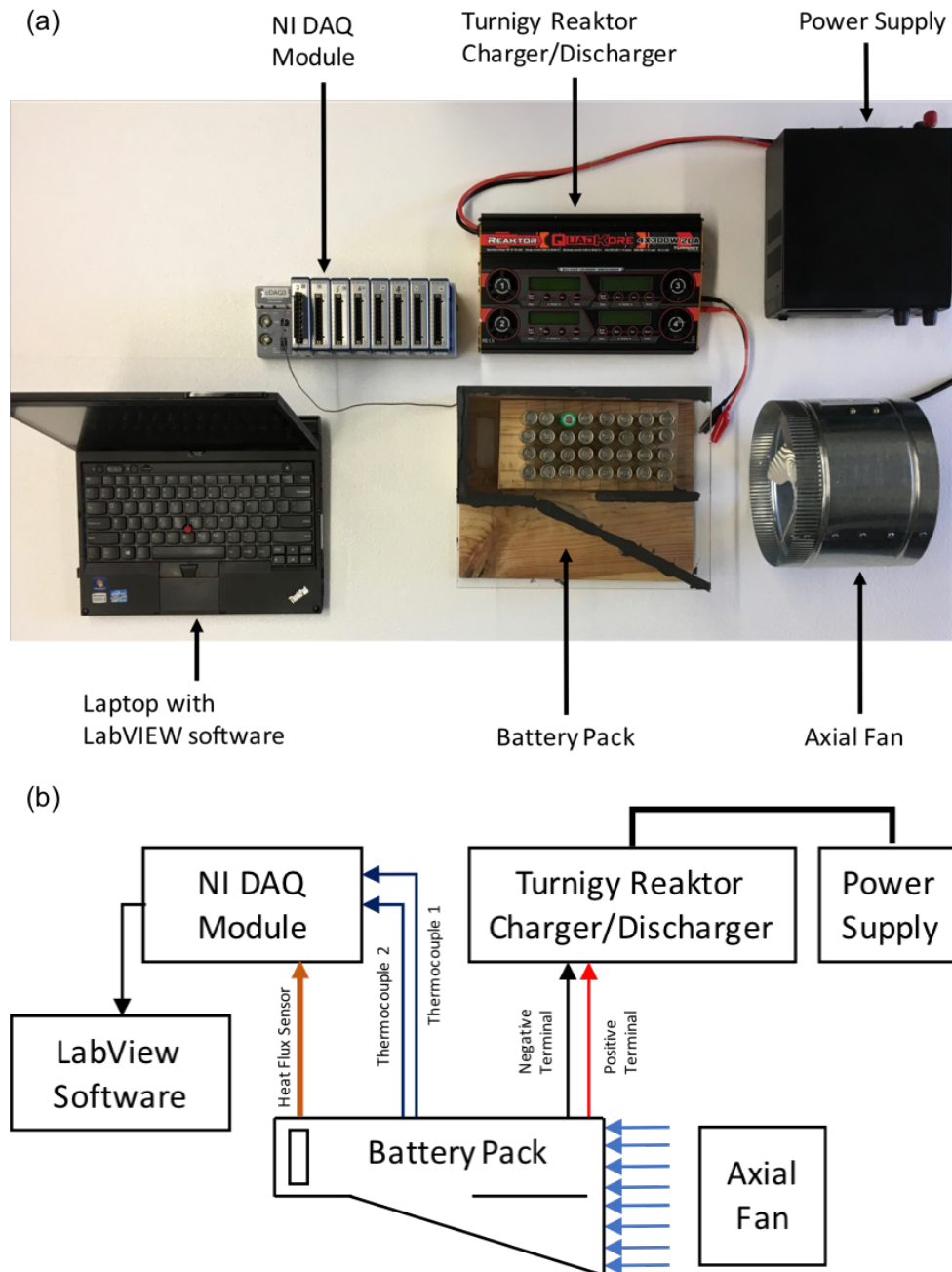


Figure 3.7: (a) Picture of the plan view of the experimental setup and (b) Schematic of the experimental setup.

For the experiments, the Case B configuration was considered. The experimental pack is shown in Figure 3.7a and the CAD model is shown in Figure 3.1b. The case of the battery pack is made of wood with an exception of the lid, which is made of acrylic to provide optical access. Commercial Li-ion 18650 cells (Samsung INR18650-25R) were used for the experimental study. The parameters/specifications of the cell are shown in Table 3.1. Two T-type thermocouples (0.51 mm diameter) were used to measure the surface temperatures of the cells. The placement locations of thermocouples are shown in Figure 3.8a. The thermocouples were connected to the National Instruments (NI) data acquisition device (NI-9211) combined with an NI cDAQ-9178 chassis and the temperature readings were recorded using LabVIEW software. The NI-9211 module has a built-in cold junction compensation for T-type and K-type thermocouples. The charge and discharge processes for the battery were conducted using the Turnigy Reaktor QuadKore (4 × 300 W 20 A) DC Synchronous Balance Charger/Discharger. To force the air through the battery pack, an axial fan (203.2 mm diameter and 42 W) was used. To measure the velocity of the air at the inlet of the battery pack an anemometer (Proster TL017), with a velocity range of 0 to 30 m/s and a temperature range of -10 to 45 °C was used.

3.3 Experimental Procedure

The thermal testing of the cells in the battery pack was carried out using the arrangement shown in Figure 3.7b. The electric wires were used to connect the positive and negative terminals and alligator clip wires connected them to the Turnigy Reaktor QuadKore charger/discharger.

Due to space constraints, two T-type thermocouples were placed on the surface of the cell at locations L1 and L2 (Figure 3.8a) using adhesive tape. As indicated in the figure they are at a distance of 52 mm from the base of the battery pack. These specific locations were selected because at location L1 there is a dead air region and the temperature is expected to be higher.

However, location L2 is expected to have a lower temperature due to the extra cooling provided by the air entering from the inlet plenum. The data from the thermocouples were recorded using the NI-9211 module, as mentioned earlier.

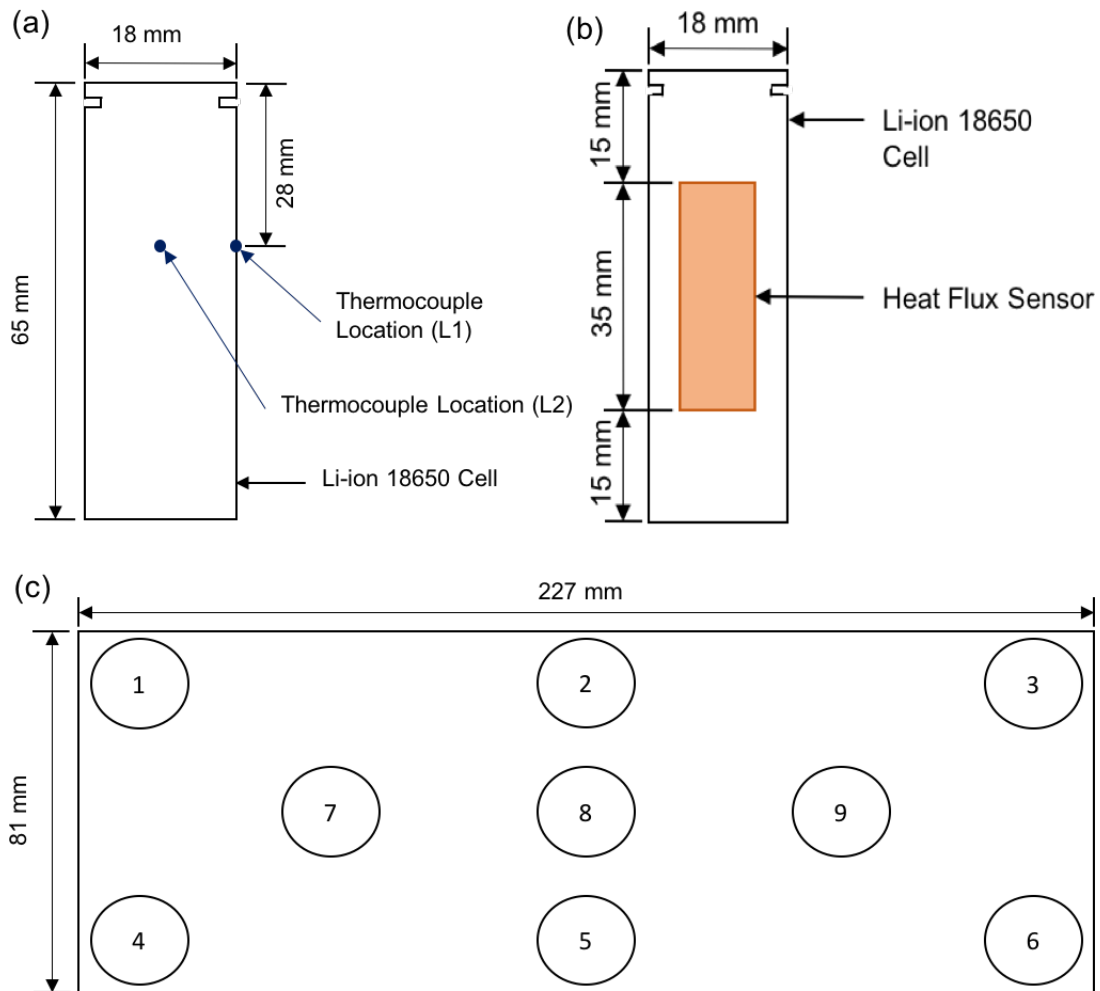


Figure 3.8: (a) Thermocouple placement locations at the leeward side of the cell; (b) front view of heat flux sensor placement location; and (c) front view of velocity measurement locations at the inlet.

The fan was placed at the inlet and the velocity was measured at multiple points across the inlet (see Figure 3.8c) and averaged to obtain the average inlet velocity. The cell was charged at 1.0 A up to 4.2 V and then natural air cooled to 23 °C. It was important to maintain the same initial conditions for both thermocouples so that temperature differences between the two locations can be reported. Once the temperature of the cell was maintained at 23 °C the discharge process was started and the cell was discharged until it reached 2.7 V at a 2 C (5 A) discharge rate. The

charging and discharging rates were carefully selected so that it falls within the charging and discharging ranges provided by Samsung SDI Company Ltd. (2014). The data for the thermocouples were recorded using LabVIEW.

A second experiment was conducted to obtain the heat flux at the surface of the cell. In this experiment, a thin film heat flux sensor (Omega HFS-3) was attached to the surface of the cell as shown in the schematic in Figure 3.8b. The cell was then insulated so that there was negligible heat transfer from the cell surface. The voltage from the heat flux sensor was recorded using the NI-9211 data acquisition device and LabVIEW. To obtain the heat flux values the voltage acquired from the heat flux sensor was converted using Equation 3.2 (Omega, n.d.). The heat flux sensor also employs a K-type thermocouple and the temperature of the cell surface corresponding to the heat flux is also recorded. Based on the results of the heat flux values, the heat generation rate was calculated. The maximum heat generation rate and corresponding temperature measured was 3.77 W and 55.7 °C, respectively. The average heat generation rate calculated was 2.75 W.

$$q'' = \frac{V}{6.37 \times 10^{-6}} \times 3.15, \quad (3.2)$$

where V is the voltage from the heat flux sensor, and q'' is the heat flux (W/m^2).

To estimate the accuracy of the results, an uncertainty analysis was carried out based on the method suggested by Moffat (1988).

3.4 Uncertainty Analysis

An uncertainty analysis was carried out for the measurements obtained from the experimental study and is presented in this section. To calculate the uncertainty of the measurements, the method described by Moffat (1998) is used. According to this method, the result, R , of the experiment is calculated as follows:

$$R = R(X_1, X_2, X_3, \dots, X_N) \quad (3.3)$$

Each individual measurement is represented as $X_i \pm \delta X_i$ where δX_i is the uncertainty. The effect on the uncertainty of each measurement on the calculated result is analyzed using the following equation:

$$\delta R = \frac{\delta R}{\delta X_i} \delta X_i \quad (3.4)$$

Therefore, the overall uncertainty of the results is calculated using the following equation:

$$\delta R = \left\{ \sum_{i=1}^N \left(\frac{\delta R}{\delta X_i} \delta X_i \right)^2 \right\}^{1/2} \quad (3.5)$$

If R is described by an equation in the form of

$$R = X_1^a X_2^b X_3^c \dots \dots X_N^m \quad (3.6)$$

then the overall uncertainty of the result can be determined using the set individual measurement uncertainties directly using the following equation:

$$\frac{\delta R}{R} = \left\{ \left(a \frac{\delta X_1}{X_1} \right)^2 + \left(b \frac{\delta X_2}{X_2} \right)^2 + \dots + \left(m \frac{\delta X_N}{X_N} \right)^2 \right\}^{1/2} \quad (3.7)$$

During the course of the experimental study, random (precision) errors arise due to personal errors and physical variations. To account for the precision errors, a relative standard deviation (RSD) is calculated using the standard deviation, s , and Equation 3.7. The relative standard deviation is useful during the comparison of uncertainties between various measurements of varying values. Finally, the bias error and precision error, are combined using the root mean square method.

$$RSD = \frac{s}{\bar{x}} 100\% \quad (3.8)$$

The uncertainty analysis explained above was used to determine the uncertainty in the temperature and heat flux measurements. According to the manufacturer's specifications, the uncertainty due to thermocouple readout is 0.6 °C (NI, n.d.). Using the above equations, the temperature uncertainties were obtained for the measured minimum temperature (T_{\min}) and maximum temperature (T_{\max}) and are shown in Table 3.4. Based on the manufacturer's specifications, the uncertainty for the heat flux sensor is 1.5 W/m² (Omega, n.d.). The calculated uncertainties associated with the minimum heat flux ($q_{\text{HFS}_{\min}}$) and maximum heat flux ($q_{\text{HFS}_{\max}}$) values are also provided in Table 3.4.

Table 3.4: Calculated values of relative bias and precision errors and total uncertainty.

Parameters	Reference Value	Absolute Bias Error	Relative Bias Error (%)	Relative Precision Error (%)	Total Uncertainty (%)
T_{\min}	23 °C	0.6 °C	2.61	6.88	7.35
T_{\max}	55.7 °C	0.6 °C	1.08	2.84	3.04
$q_{\text{HFS}_{\min}}$	21 W/m ²	1.5 W/m ²	7.06	7.53	10.3
$q_{\text{HFS}_{\max}}$	1025 W/m ²	1.5 W/m ²	0.146	0.154	0.213

The average percentage uncertainty in the temperature measurements were $\pm 5.2\%$ and in the heat flux measurements were $\pm 6.2\%$. However, it can be seen from Table 3.4 that the high percentage uncertainties in the measurements of temperatures are due to the relative precision error. The experiments were repeated only 5 times and as indicated in the equations above the precision error is sensitive to the sample size.

3.5 Numerical Modeling

To complement the experimental study, a detailed thermal and fluid flow analysis during the discharge of all the cells in the battery pack was performed using a numerical analysis.

A commercial computational fluid dynamic (CFD) software, ANSYS Fluent, was employed for the numerical analysis. The governing equations for continuity, momentum, and energy are expressed in Equations 3.9 to 3.11, respectively (Wang et al., 2015).

Continuity Equation

$$\nabla \vec{v} = 0 \quad (3.9)$$

Momentum Conservation Equation

$$\frac{\partial \vec{v}}{\partial t} + (\vec{v} \nabla) \vec{v} = -\frac{\nabla p}{\rho} + \frac{\mu}{\rho} \nabla^2 \vec{v} \quad (3.10)$$

Energy Conservation Equation

$$\rho c_p \left(\frac{\partial E}{\partial t} + v_x \frac{\partial E}{\partial x} + v_y \frac{\partial E}{\partial y} + v_z \frac{\partial E}{\partial z} \right) = k_T \left(\frac{\partial^2 E}{\partial x^2} + \frac{\partial^2 E}{\partial y^2} + \frac{\partial^2 E}{\partial z^2} \right) \quad (3.11)$$

The Shear Stress Transport (SST) k - ω model was employed to simulate the air flow. The SST model has been proven to be stable and numerically robust and it has the capability to provide a suitable prediction when a compromise between accuracy of the results and robustness of the simulation is required (Saw et al., 2016). The details of the SST model can be found in the studies done by Menter et al. (2003), Sparrow et al. (2009) and Lee et al. (2013). The transport equations of the SST model are as follows (Menter et al., 2003; Saw et al., 2016):

$$\frac{\partial(\rho k)}{\partial t} + \frac{\partial(\rho U_i k)}{\partial x_i} = \tilde{P}_k - \beta^* \rho k \omega + \frac{\partial k}{\partial x_i} \left[(\mu + \sigma_k \mu_t) \frac{\partial k}{\partial x_i} \right] \quad (3.12)$$

$$\begin{aligned} \frac{\partial(\rho \omega)}{\partial t} + \frac{\partial(\rho U_i \omega)}{\partial x_i} = & \alpha \rho S^2 - \beta^* \rho \omega^2 + \frac{\partial}{\partial x_i} \left[(\mu + \sigma_\omega \mu_t) \frac{\partial \omega}{\partial x_i} \right] + \\ & 2(1 - F_1) \rho \sigma_{\omega 2} \frac{1}{\omega} \frac{\partial k}{\partial x_i} \frac{\partial \omega}{\partial x_i} \end{aligned} \quad (3.13)$$

where the function F_1 is defined by the following equation:

$$F_1 = \tanh \left\{ \left\{ \min \left[\max \left(\frac{\sqrt{k}}{\beta^* \omega y}, \frac{500\nu}{y^2 \omega} \right), \frac{4\rho \sigma_{\omega 2} k}{CD_{k\omega} y^2} \right] \right\}^4 \right\} \quad (3.14)$$

where y is the nearest wall distance and $CD_{k\omega}$ is defined as follows:

$$CD_{k\omega} = \max \left(2\rho \sigma_{\omega 2} \frac{1}{\omega} \frac{\partial k}{\partial x_i} \frac{\partial \omega}{\partial x_i}, 10^{-10} \right) \quad (3.15)$$

3.5.1 Mesh Generation

One of the important steps is to generate a mesh with high quality. Various parameters, including the number of nodes and the shape of the elements, have a significant impact on the accuracy of the results and the numerical behavior of the solution. The unstructured mesh shown in Figure 3.1 was generated using the ANSYS Meshing software.

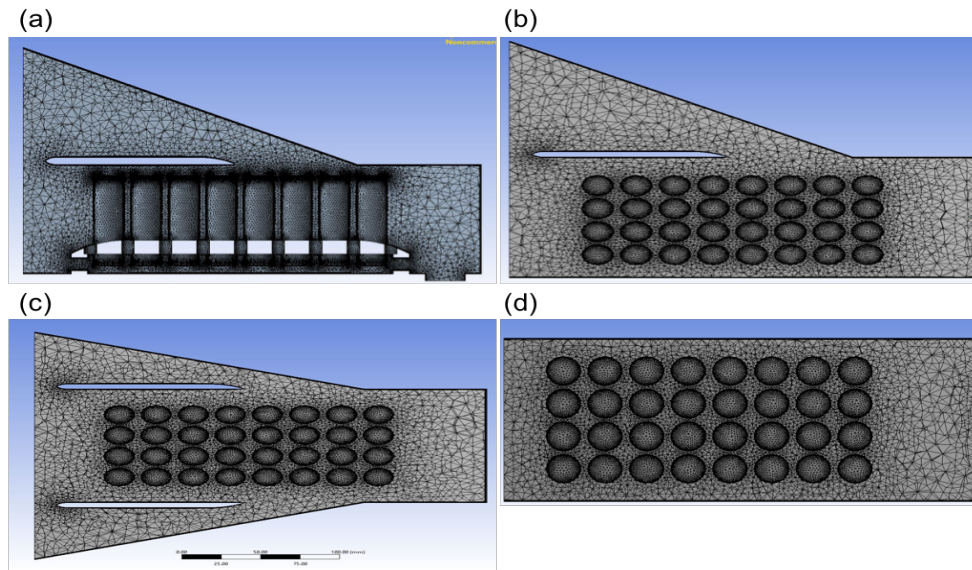


Figure 3.9: (a) Side view of generated mesh of Case A, (b) Plan view of generated mesh of Case B, (c) Plan view of generated mesh of Case C and (d) Plan view of generated mesh of Case D.

Mesh refinement and inflation layers were applied to capture the boundary layer at the surface of the cells, vortex generators and the boundary walls of the jet inlets and the battery pack. The y^+ number is defined in Equation 3.15 (He et al., 2015).

$$y^+ = \frac{y}{\nu} \sqrt{\frac{\tau_w}{\rho_f}} \quad (3.16)$$

Where; ν represents the local kinematic viscosity, y nearest wall distance (i.e., the thickness of the boundary layer grids here), τ_w the wall shear stress, and ρ_f the fluid density.

A total of 7 prismatic layers were used with a growth ratio of 1.2. The thickness of the first layer was set based on the y^+ value of 1. This y^+ value is consistent with the recommended

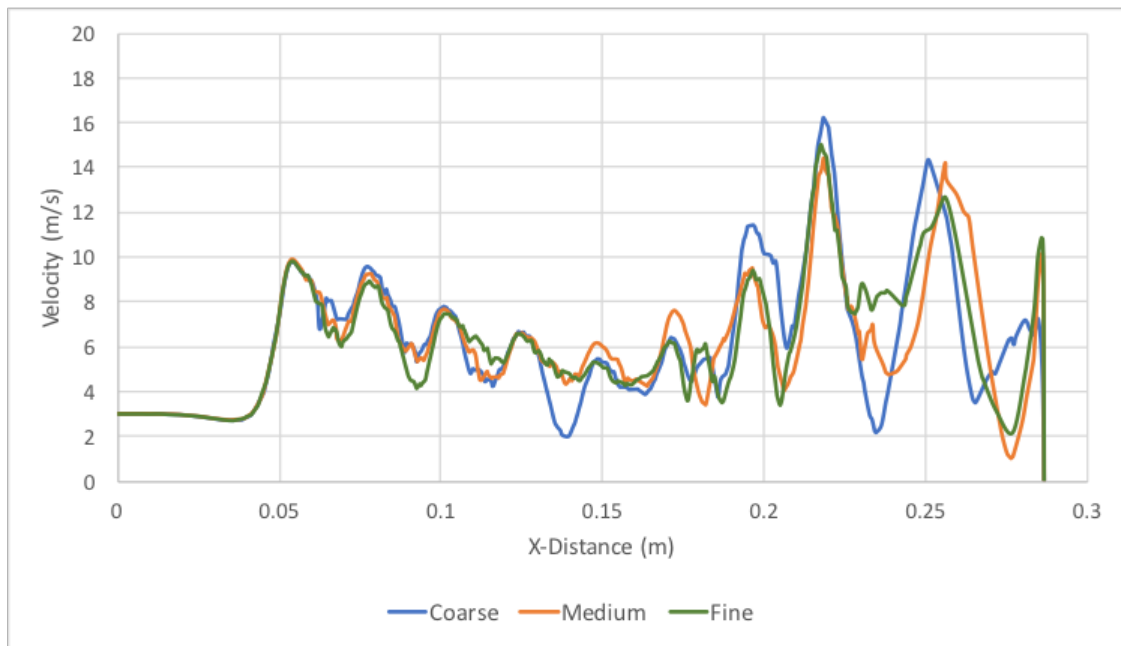
values in the open literature (He et al., 2015; Li et al., 2013). It trades off extreme resolution with lower y^+ values while still maintaining approximation of the boundary layer.

3.5.2 Mesh Independence Study

In order to verify that the results obtained from the numerical analysis are independent of the resolutions of the generated meshes, a mesh independence study was conducted. For this study, a coarse, medium and fine meshes were developed. The number of elements was increased by 25% for each subsequent mesh. A course mesh consisted of 6.15 million elements, medium mesh consisted of 8.2 million elements and fine mesh consisted of 10.25 million elements. The solution was computed for Case A configuration. The results of the mesh independence study in shown in Figure 3.9. The velocities and temperatures were obtained at the center of the battery pack along the axial direction.

The velocity and the temperatures data are a near match between the medium and the fine detail meshes, as shown in Figure 3.9. Given the difference in computational times for the meshes, it was decided that the medium detail mesh was a good balance between computational time and accuracy. Therefore, based on the mesh independence study the selected (medium-detail) mesh consisted of approximately 8.2 million elements.

(a)



(b)

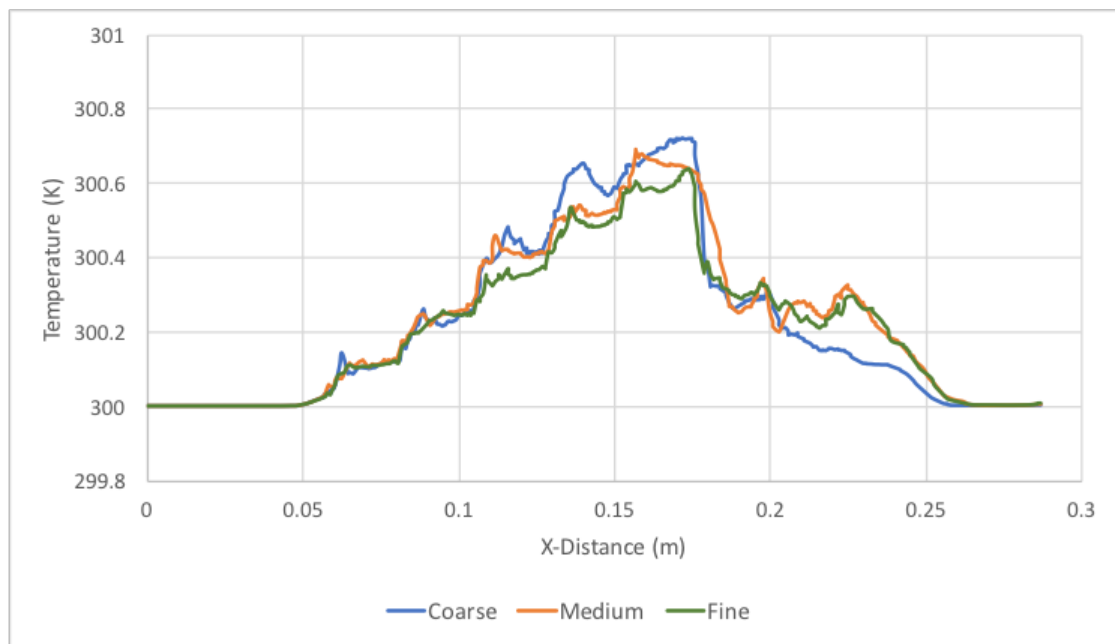


Figure 3.10: Comparison of (a) velocity and (b) temperature for the coarse, medium and fine meshes.

3.5.3 Boundary conditions

For all the battery pack configurations and tests, the outlet boundary condition was set to pressure outlet. The flow was considered incompressible, steady-state and turbulent. The temperature at the inlet was set to 23 °C. In addition, the value of heat generation rate was calculated using the heat flux values obtained from the experimental study. An average heat generation rate value of 2.75 W was used as the thermal boundary condition at the surface of the cells. A no-slip boundary condition was set on the walls. Moreover, the convergence criteria of the residuals of the computational variables were set at 10^{-4} for continuity, velocity, turbulence, specific dissipation rate, and energy equations. The SIMPLE scheme was used for pressure-velocity coupling and second order upwind spatial discretization method was used for momentum, turbulent kinetic energy, specific dissipation rate, and energy equations (He et al., 2015). The inlet velocity boundary condition was different depending on the study, therefore, the velocity boundary condition is described in the following sections.

3.5.3.1 Study of Inlet Plenum and Cell Orientations

The inlet boundary conditions for Cases A, B, C, and D were based on the Reynolds number at the inlet of the battery pack. The hydraulic diameter of the inlet was selected as the characteristic length for Reynolds number calculation due to the variation in the dimensions of the battery pack inlet. Based on the velocity of inlet air of 2.2 m/s, obtained from experimental study, the Reynolds number calculated was 18,000 for Case B and it was kept constant for all the other cases including the baseline battery pack so that a comparison of air cooling can be made amongst the different configurations. The boundary conditions used for the comparison of different cell orientations are provided in Table 3.5.

Table 3.5: Boundary conditions for Cases A, B, C, and D.

Boundary Conditions	Case A	Case B	Case C	Case D
Inlet velocity (m/s)	2.0	2.2	2.2	2.8
Inlet temperature (°C)	23.0	23.0	23.0	23.0
Heat generation rate (W)	2.75	2.75	2.75	2.75

3.5.3.2 Parametric Study and Reynolds Number Study of Case A

For the separating plate length and nozzle length changes, the velocity-inlet boundary condition of the air was set to 2 m/s so that a comparison can be made between all the test configurations (Test numbers 1 to 7). For the Reynolds number study (test numbers 8 to 13), six Reynolds numbers as shown in Table 3.3 were examined. In order to be consistent with the open literature, the calculation of Reynolds number for this study was based on the diameter of the cell rather than the inlet hydraulic diameter.

3.5.3.3 Jet Inlet and Multiple Vortex Generator Study for Case A and Case D

For Cases A1, A2 and A3 described in section 3.1.4, the velocity inlet boundary condition of the air was set as 3.45 m/s, based on the Reynolds number of 4,252 of Case A. The velocity is constant as there is no change in the dimensions of these configurations, and thus, no change in the mass flow rate.

For Case D1, D2, D3, and D4 described in section 3.1.5, the mass flow rate was kept the same. Based on the Reynolds number of 4,252, the velocity-inlet boundary condition of the air was set to 7.11 m/s for Case D1 and 6.53 m/s for Case D2, D3, and D4. This difference in the inlet velocities is caused by the increase in the width due to the addition of jet inlet 3.

Chapter 4: Results and Discussion

This chapter presents the results and discussions that were obtained from the experiments and numerical simulations. The first part provides an analysis for the different configurations of the inlet plenum and cell orientations. The second part gives an analysis of the parametric study conducted to determine the optimum location of the inlet plenum and the Reynolds number study to determine the optimum inlet velocity required for the thermal management system. The third part provides an analysis on the addition of jet inlets and vortex generators. Finally, the last part compares and analyzes the jet inlets vortex generators when used without the inlet plenum on the basic battery pack.

4.1 Heat Generation Rate of Cell

Figure 4.1 shows the results of the heat generation rate at the surface of the cells at 2C discharge rate and the corresponding temperatures of the cell without cooling. Using the measurements of the heat flux at the surface of the cell through the experiments, the heat generation rate was calculated. The profiles of the heat generation rate and the temperature (without cooling) are consistent with the profiles reported in the study by Saw et al. (2016). The maximum heat generation rate measured is 3.77 W and its corresponding temperature increase is up to 55.7 °C. Additionally, 2.75 W is average heat generation rate calculated. The average heat generation rate calculated is used as a thermal boundary condition for the cells in the numerical study. The profiles in Figure 4.1 provide a perspective of how heat generation rate and temperature change with time during the experiment.

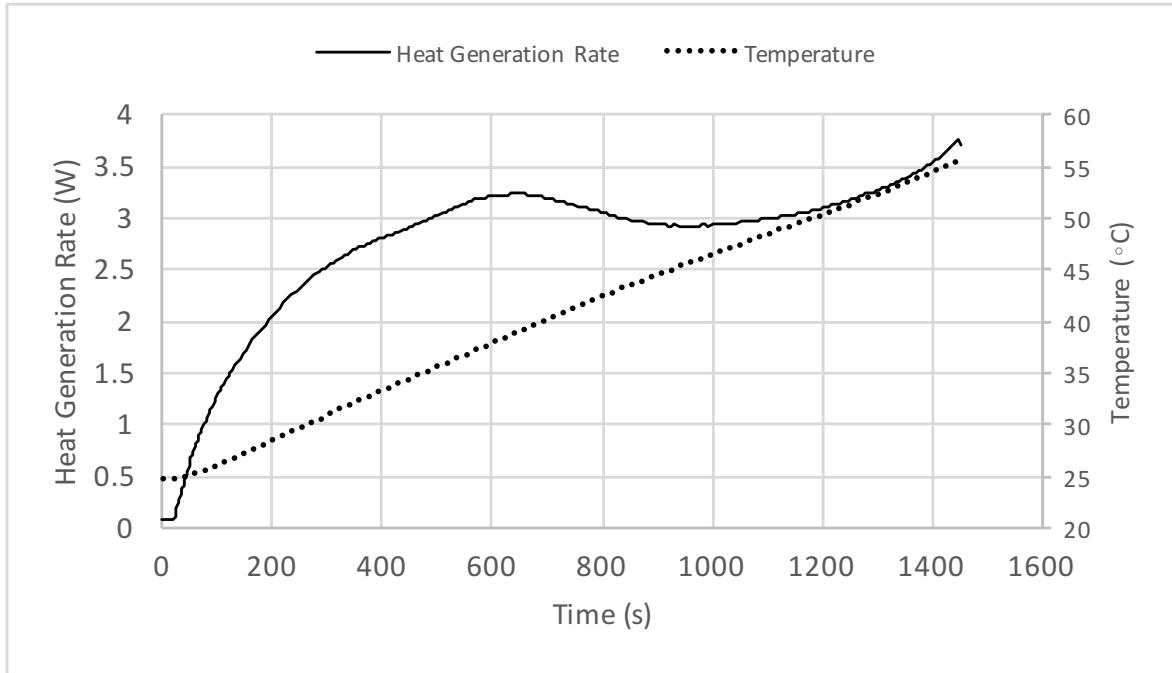


Figure 4.1: Heat generation rate and the corresponding temperature increase at 2C discharge rate.

4.2 Model Validation

Model validations are required and deemed necessary in order to confirm that the developed mesh, model parameters, and the boundary conditions used predict similar results when compared to results of the actual experimental conditions. Therefore, the numerical study employed for this research has also been validated with the results of the experimental studies.

Due to the capacity of the charger/discharger to discharge one cell at a time, three cells were selected randomly for the experiments, which include cell number 3, 9 and 31 as indicated in Figure 3.2a. The temperature measurements obtained for these cells at locations L1 and L2 from the experiments (Figure 3.8a) were compared with the temperature results attained from the simulations at the same locations. The validations are shown in Figure 4.2 and the percentage differences between the compared results are provided in Table 4.1. There is an average temperature difference of 1.1 °C between the experiments and simulations, which is consistent with the temperature validations in open literature (Ling et al., 2015). Therefore, it

can be concluded that the modeling and the numerical results are in agreement with the experimental results.

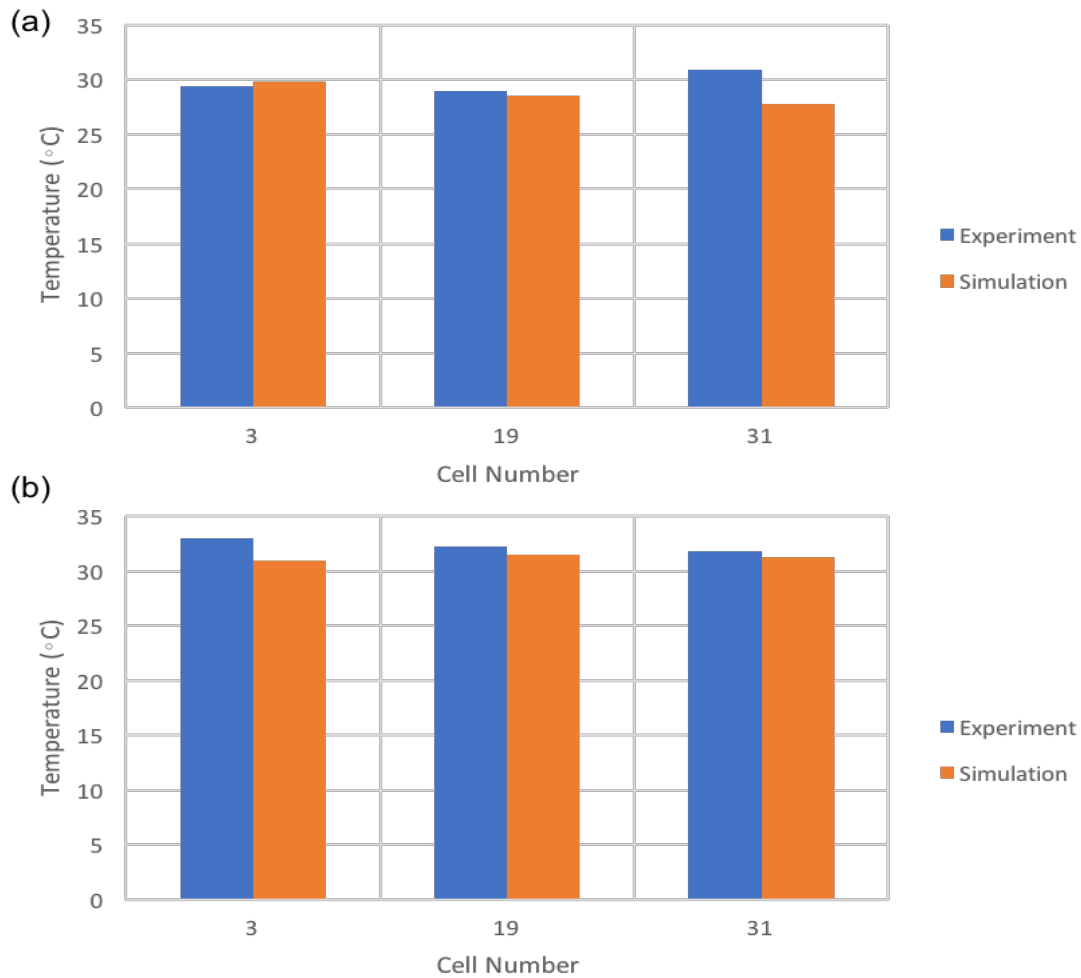


Figure 4.2: Model validation: (a) temperatures at location L1 (b) temperatures at location L2 of the cell.

Table 4.1: Temperature differences between the experimental and numerical results.

Location	L1			L2		
Cell Number	3	19	31	3	19	31
Temperature Difference (°C)	0.4	0.5	3.1	2	0.8	0.5

4.3 Study of Inlet Plenum and Cell Orientations

4.3.1 Thermal Analysis

As mentioned earlier, uniformity in the temperature of a single cell and the battery pack has a significant effect on the performance of the cells and the battery pack. The discharge rates of

the cells are dependent on the temperature of the cell and if there are significant differences in temperature variations, the discharge rates of each cell will also vary significantly. This variation results in the different values of state of charge (SOC) amongst all the cells. In a battery pack, the lowest SOC cell determines the discharge rate of the battery pack and the lower end of the usable energy rate and the highest SOC cell determines the upper end of the usable energy range (Kuper et al., 2009). Non-uniform discharge rates result in electrically unbalanced cells and a degradation of the performance of the battery pack (Pesaran, 2002; Saw et al., 2016).

Table 4.2 shows a comparison of the results of the battery packs (Case A, B, and C) used in this study and the baseline battery pack (Case D). The maximum temperature in the table represents the maximum temperature of the whole battery pack and not a particular cell, similarly, the temperature difference represents the difference between the maximum temperature of the battery pack and the minimum temperature of the battery pack. It can be seen from the table that for Cases A and B, the maximum temperature of the battery pack reduces by 9% and 7.4% respectively and the temperature difference between the maximum and the minimum temperature of the battery pack decreases by 25% and 16.7% respectively, compared to the baseline pack. Whereas, for Case C there is no change in the maximum temperature of the battery pack compared to the baseline pack and the temperature difference between the maximum and the minimum temperature of the battery pack increases by 3.3%. A higher temperature difference equates to lower temperature uniformity in the battery pack and a lower temperature difference equates to a higher temperature uniformity,

Table 4.2: Comparison of Case A, B, and C with the baseline battery pack (Case D).

Parameters	Baseline (Case D)	Case A	Case B	Case C
Maximum Temperature (°C)	37.8	34.4	35.0	37.8
Temperature Difference (°C)	12.0	9.0	10.0	12.4

Figure 4.3 presents the contours of the temperature distribution of the cells for the different battery pack configuration and clearly indicates that the type of configuration affects the temperature profiles significantly. The contours in Figure 4.3a show that in the baseline pack, the temperature of the cells increases along the length of the battery pack as expected. For Case A (Figure 4.3b), the contours show that the temperature increases until the first 5 cells in each row and then start to reduce once airflow from the inlet plenum mixes with the battery pack airflow. Similarly, for Case B (Figure 4.3c), the contours show that the temperature increases until the 4th cell in rows 1 and then starts to reduce but for row 2, 3 and 4 the temperature increases till the 6th cell. Also, Case C (Figure 4.3d) shows that the temperature of the cells in rows 2 and 3 increases till the 6th cell, whereas, the temperature of cells in row 1 and 4 starts to decrease after the 5th cell.

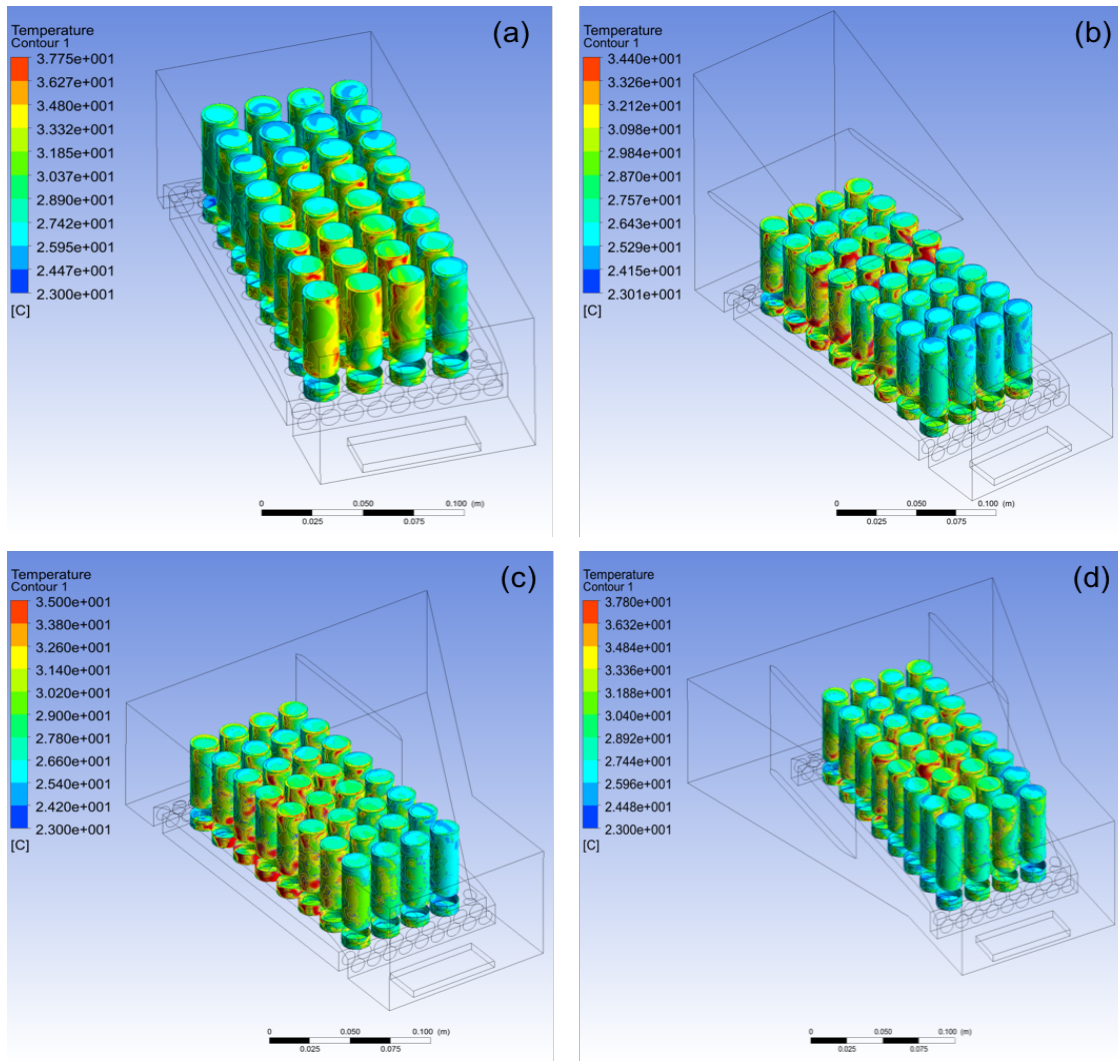


Figure 4.3: Temperature distribution of the cells: (a) Baseline battery pack, (b) Case A, (c) Case B, and (d) Case C.

For further analysis, the maximum temperature for the cells in each row is shown in Figure 4.4 for all the battery packs. For Case A, the overall trend in each row is that the maximum temperature starts to reduce after the 5th cell with the exception of row 1, in which, the maximum temperature starts to reduce after the 4th cell. In Case B, the first row shows the same trend as Case A. In the second and third rows the temperature starts to reduce after the 6th cell. In Case C, the 5th cell in the first row, 6th cell in the second row and 2nd, 4th and 5th cells in the third-row exhibit high temperature. The fourth row exhibits a trend of a more uniform maximum temperature throughout the whole row except the last cell.

Comparing Case A with Case C, Figure 4.4 shows that most of the cells in all the rows in Case C have higher maximum temperatures, with the exception of cell number 4, 10, 12, 13, 19, 26 and 29. This shows that 78% of cells in Case A have lower maximum temperatures than Case C and the average maximum temperature is reduced by 5%. In Case B, all the cells in first row, 3 cells (cell number 9, 10 and 12) in second row, 3 cells (cell number 19, 22 and 23) in third row and 3 cells (cell number 27, 29 and 32) in fourth row have lower temperatures than Case C. This amounts to 72% of cells with lower maximum temperatures than Case C and the average maximum temperature is reduced by 3.7%. This suggests that Case A and B provide better cooling of cells compared to Case C. Moreover, in Case A, 3 cells (cell number 3, 4 and 8) in first row, 2 cells (cell number 10 and 13) in the second row, 3 cells (cell number 17, 19 and 21) in the third row and 4 cells (cell number 25, 26, 28 and 29) in the fourth row exhibit higher temperatures than Case B. This amounts to 63% of cells with lower maximum temperature in Case A and the average maximum temperature is reduced by 1.3%. Additionally, compared to the baseline model, Case A reduces the average maximum temperature by 3.8%.

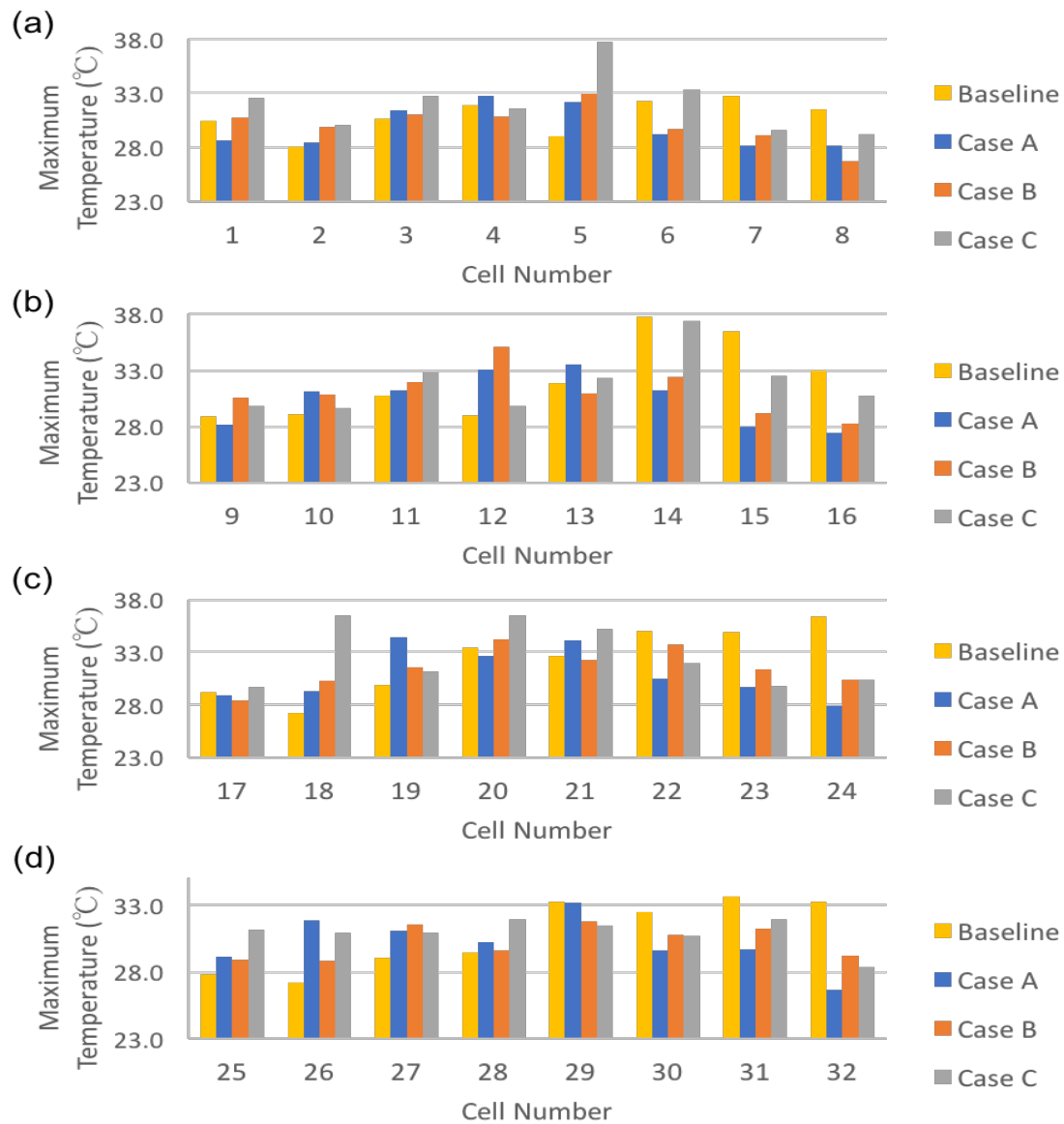


Figure 4.4: Maximum temperature of cells across (a) Row 1, (b) Row 2, (c) Row 3 and (d) Row 4.

The temperature difference between the maximum and the minimum temperatures for cells in each row is shown in Figure 4.5. In Case A, 9 cells show a higher temperature difference than the cells in Case C. This shows that 72% of cells in Case A have more temperature uniformity than Case C and the average temperature uniformity is increased by 34.8%. In Case B, 14 cells have higher temperature differences when compared with Case C. This shows that 56% of cells in Case B have higher temperature uniformity than Case C and the average temperature uniformity is increased by 6.5%. In Case A, 11 cells have higher temperature variations than

the cells in Case B. This shows that 66% of cells in Case A have higher temperature uniformity and the average temperature uniformity is increased by 26.5%. Furthermore, compared to the baseline battery pack, the average temperature uniformity of Case A is increased by 38.8%. Therefore, Case A has the lowest average maximum temperatures and the highest temperature uniformity compared to the baseline battery pack and Case B and C.

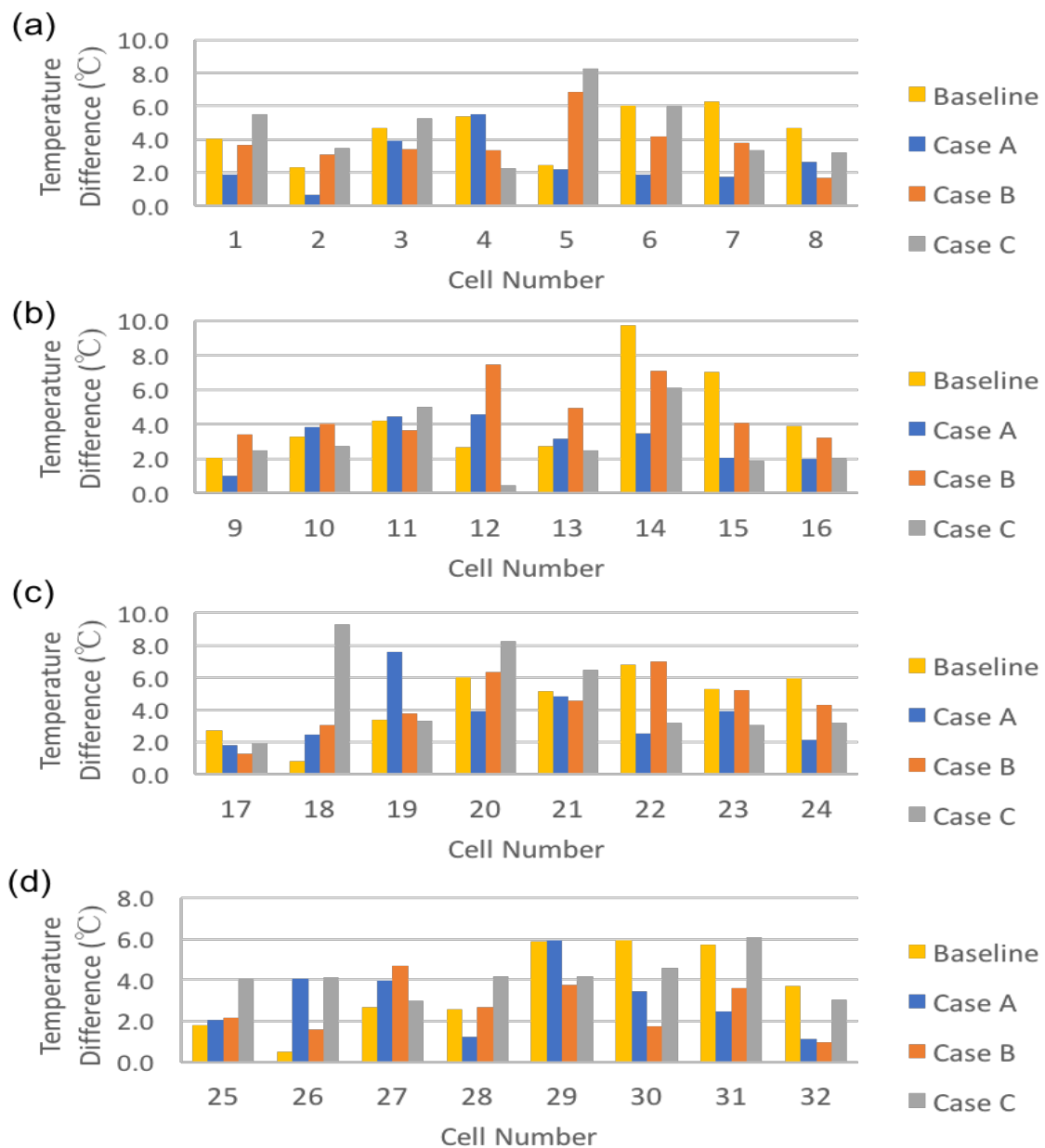


Figure 4.5: Temperature difference between the maximum and minimum temperatures of cells across (a) Row 1, (b) Row 2, (c) Row 3, and (d) Row 4.

4.3.2 Air Flow Analysis

One of the problems with the design of the baseline battery pack is that the air flows straight in between the rows and only some of the air enters in between the adjacent cells. This leads to recirculation of the air between the cells and dead air regions as seen in Figure 4.6a and Figure 4.7a. In the baseline battery pack, the first few cells do not experience this problem because of the fact that the higher inlet velocity mixes after hitting the cells as seen in Figure 4.7a. The higher turbulence kinetic energy between the first few cells reduces the maximum temperature and the temperature variation across the cells. However, once the flow becomes streamlined in the second half of the battery pack the turbulence kinetic energy between the cells in the same row reduces to a minimum, resulting in an increase in the maximum temperature and a decrease in the temperature uniformity as represented in Figure 4.4 and 4.5. Additionally, Figure 4.8a shows that the temperature is lower where there is a higher turbulence kinetic energy and a higher mixing of flows, whereas, once the flow starts to flow in between the rows there is less flow or air in between the adjacent cells along the length of the battery pack. Therefore, to tackle this problem the inlet plenum was added to the battery packs.

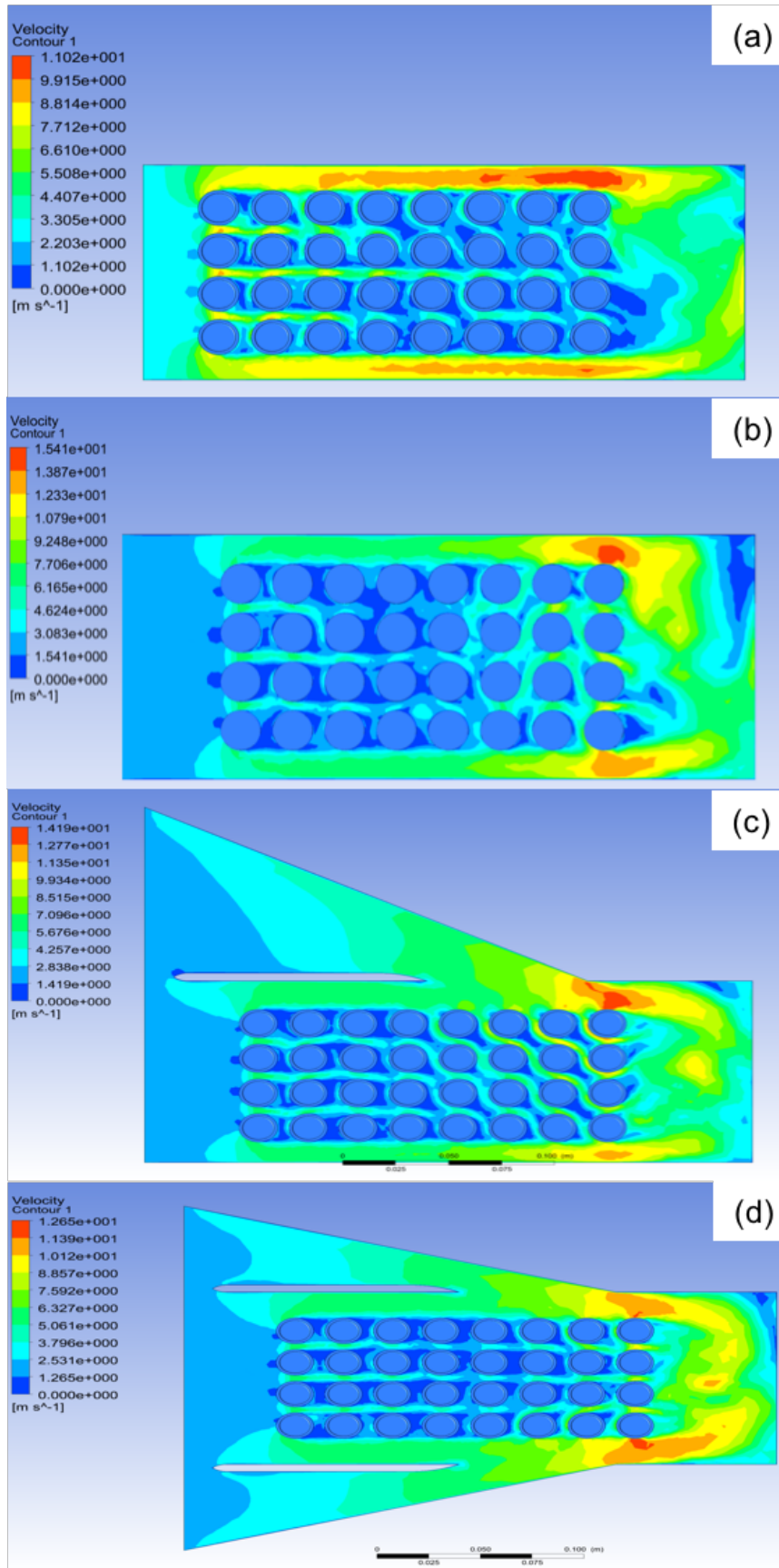


Figure 4.6: Velocity contours of (a) Case D, (b) Case A, (c) Case B, and (c) Case C in the horizontal plane at 52 mm from the base of the battery pack.

The injection of air in the battery packs has resulted in the mixing and turbulence in the flow as shown in Figure 4.6b, c, d and Figure 4.7b, c, d. In all the battery packs, it can be clearly observed that once the air is injected into the cells' compartment, the mixing and turbulence increases between the cells. The intense mixing of the fluid in turbulent flow enhances heat and momentum transfer between fluid particles, which in turn increases the convection heat transfer coefficient, resulting in a higher rate of heat transfer. Therefore, the locations with higher turbulence kinetic energy have high heat transfer and low temperatures.

From Figure 4.6c and Figure 4.7c, it can be observed that Case C has the least amount of mixing and turbulence, especially in row 2 and 3, compared to Case A and B. The turbulence kinetic energy near the cells in Case C is also lower compared to the other two cases. Due to less mixing and turbulence between the adjacent cells, Case C experiences higher values of maximum temperature and temperature variations resulting in less uniformity in the cooling of the battery pack, as suggested by the thermal analysis as well.

Moreover, by observing the results of Case A and Case B from Figure 4.6b, c, and Figure 4.7b, c, it can be seen that the two cases show higher values of turbulence kinetic energy near the cells in the second half of the battery packs. The airflow in between the cells also experiences a higher amount of mixing and turbulence which is why the thermal analysis results of both these cases were similar. However, from Figure 4.7b and c, it can be seen that in the second half of the battery pack the turbulence kinetic energy of air is more uniform in Case A when compared to Case B. Due to this in Case A, the cell in the second half of the battery pack exhibit higher temperature uniformity as reported in the thermal analysis earlier.

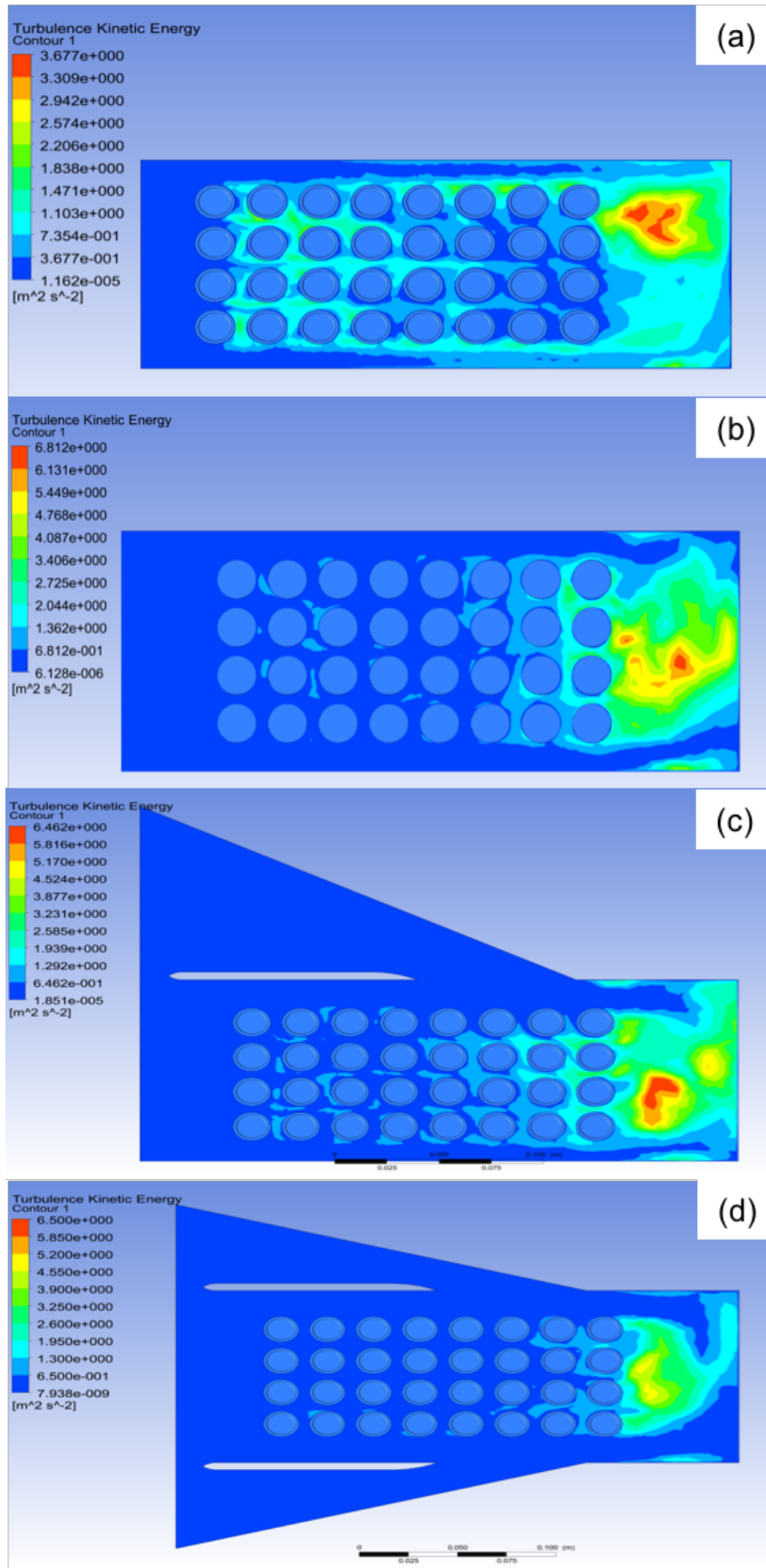


Figure 4.7: Turbulence kinetic energy contours of (a) Case D, (b) Case A, (c) Case B, and (c) Case C in the horizontal plane at 52 mm from the base of the battery pack.

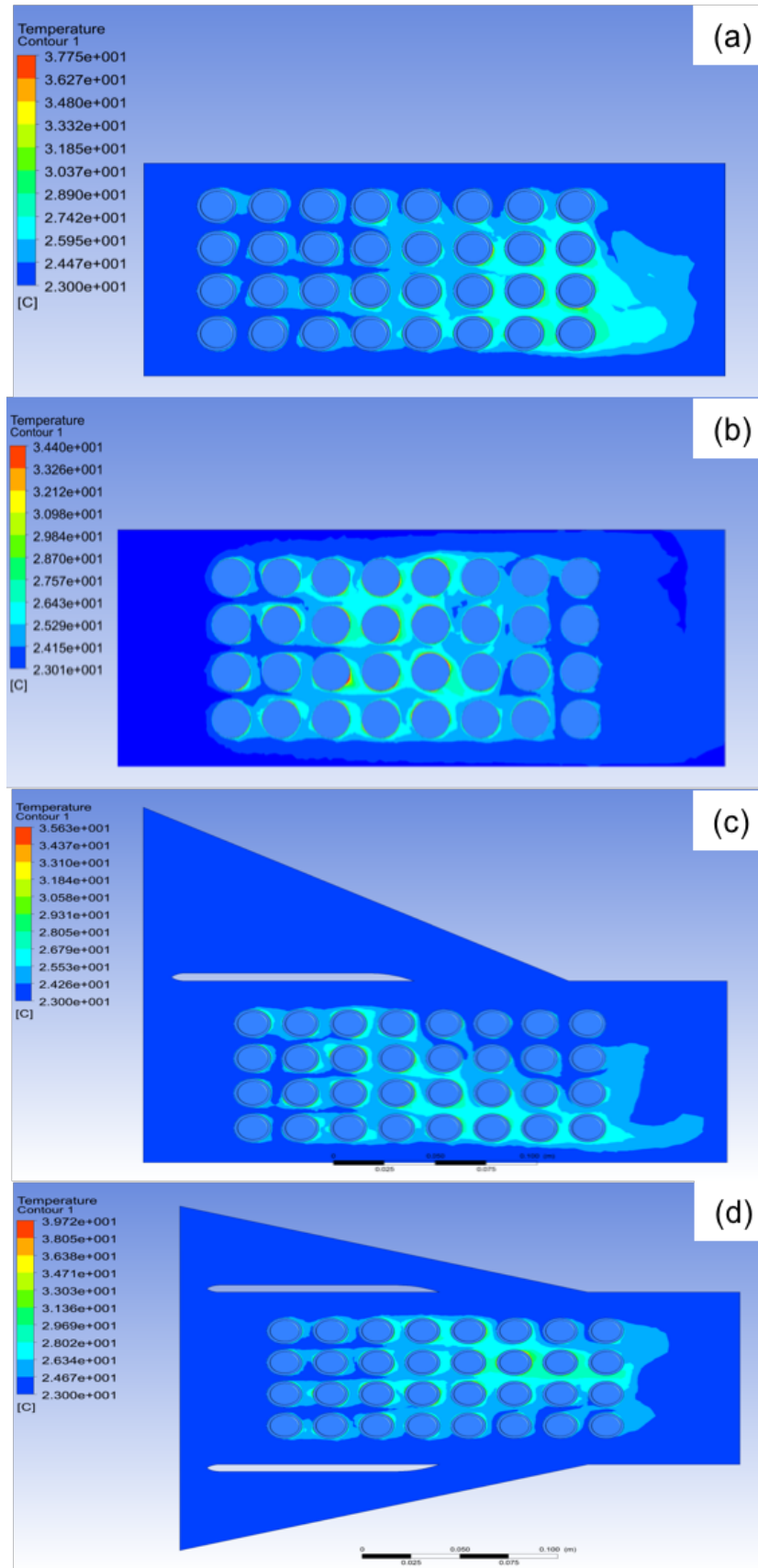


Figure 4.8: Temperature contours of (a) Case D, (b) Case A, (c) Case B, and (c) Case C in the horizontal plane at 52 mm from the base of the battery pack.

4.4 Parametric Study and Reynolds Number Study of Case A

Temperature uniformity in the battery pack, as well as that in a single cell, have a significant effect on the performance of the cells and the battery pack as stated earlier. The self-discharge rates of the cells are dependent on the temperature of the cell and if there are significant differences in temperature variations, the discharge rates of each cell will also vary significantly. This variation results in the different values of state of charge (SOC) amongst all the cells. In a battery pack, the lowest SOC cell determines the discharge rate of the battery pack and the lower end of the usable energy rate. On the other hand, the highest SOC cell determines the upper end of the usable energy range (Kuper et al., 2009). Non-uniform discharge rates result in electrically unbalanced cells and a degradation of the performance of the battery pack (Pesaran, 2002; Saw et al., 2016). Therefore, the desired temperature uniformity within each cell and within the battery pack is less than 5 °C (Kuper et al., 2009; Liu et al., 2015; Pesaran, 2002; Saw et al., 2016).

4.4.1 Separating Plate Length Analysis

The parameters for the Tests 1 to 5 are provided in Table 3.2. The variation of the maximum temperature of the battery pack with the increase in the length of the separating plate is shown in Figure 4.9a. It can be seen that the maximum temperature of the battery pack increases as the length of the separating plate is reduced. The lowest maximum temperature of 34.4 °C is exhibited by test number 1, in which the air from the nozzle enters half-way through the battery pack. The highest temperature of 37 °C is exhibited by test number 2, in which the air enters after the third column of cells, and test number 5, in which there is no separating plate. Test number 1, therefore, reduces the maximum temperature of the battery pack by 7.5%. The average maximum temperature for all the cells in the battery pack is shown in Figure 4.9c. By

reducing the length of the plate, the average maximum temperature also increases from 30.4 °C in test number 1 to 31.5 °C in test number 5, an increase of ~3.6%.

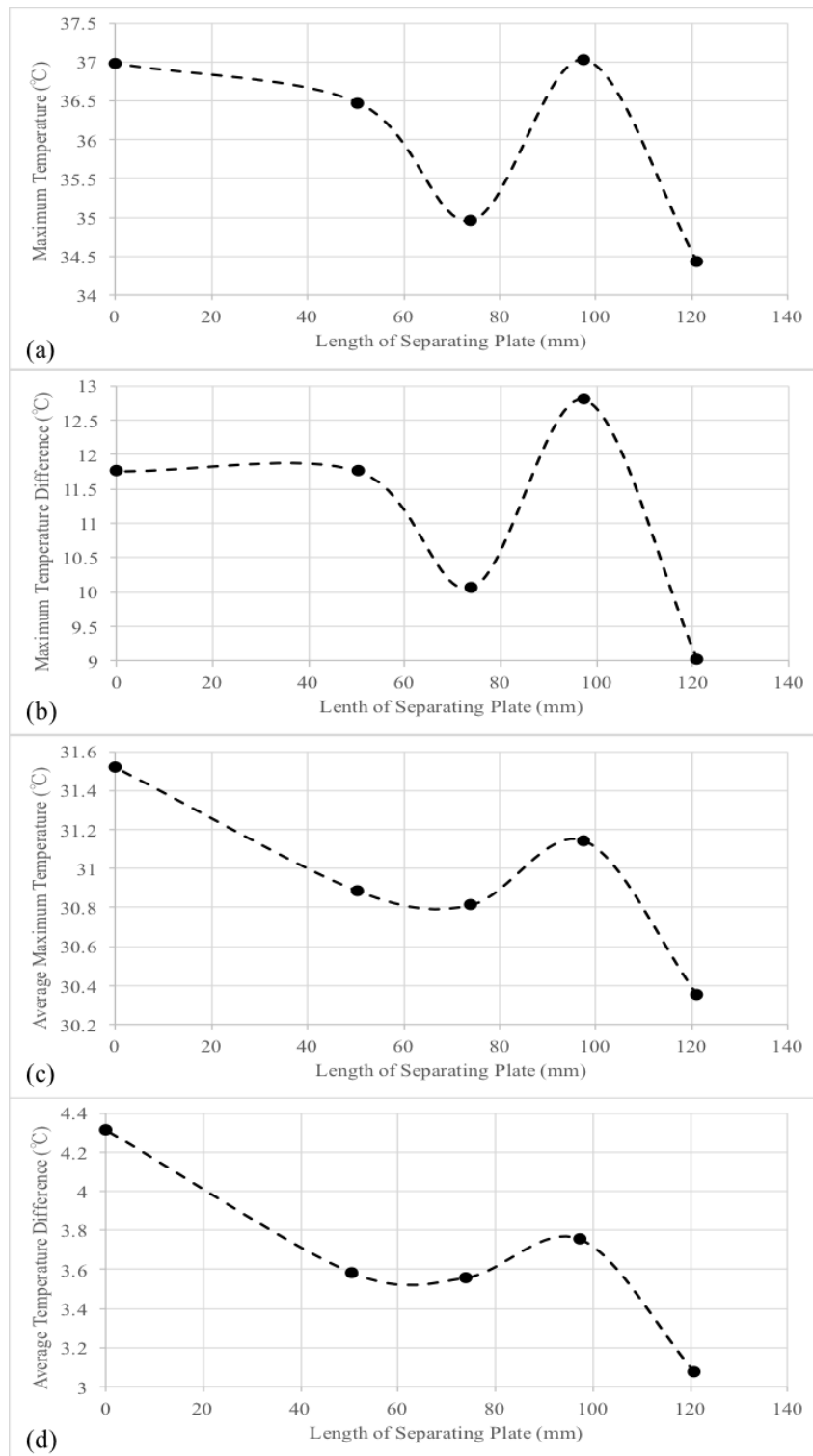


Figure 4.9: (a) Maximum temperature, (b) maximum temperature difference, (c) average maximum temperature and (d) average temperature difference across the battery pack for test numbers 1 to 5 in Table 3.2.

Figure 4.9b represents the maximum temperature difference between the lowest temperature and the highest temperature of the battery pack. The results also show that by decreasing the length of the separating plate the maximum temperature difference within the battery pack also increases from 9 to 11.8 °C, however, test number 2 shows a higher temperature non-uniformity as the maximum temperature difference goes up to 12.8 °C. The average temperature difference is shown in Figure 4.9d. This was calculated by measuring the temperature difference within each cell and then averaging it out for all the cells in the battery pack. The trend is similar to the trend observed from the maximum temperature difference. It shows that as the average temperature difference increases from 3.1 to 4.3 °C when the length of the separating is reduced, an increase of 40.3% in the temperature non-uniformity of the battery pack.

The temperature differences between the maximum and minimum temperatures of each cell are shown in Figure 4.10. It can be seen that 3 cells in test number 1, 6 cells in test number 2, 7 cells in test number 3 and 4 and 11 cells in test number 5 have temperature differences more than 5 °C. This shows that 90.6% of cells exhibit a desirable temperature uniformity in test number 1. This percentage reduces to 65.6% in test number 5 where there is no separating plate present between the main compartment and the nozzle. Therefore, compared to all the test configurations, test number 1 (121mm separating plate length) has the lowest maximum temperature and the highest temperature uniformity and is the optimum length of the separating plate.

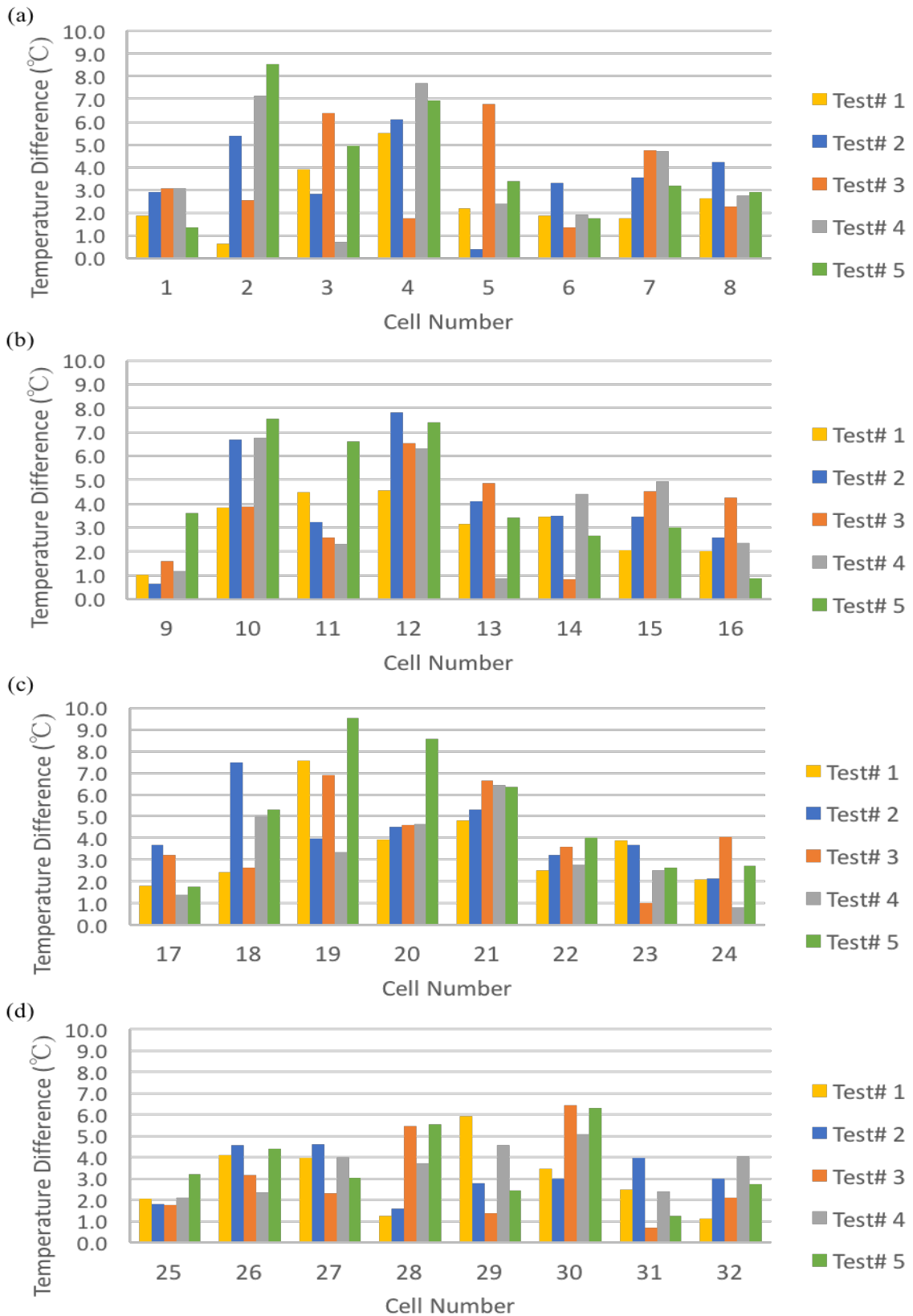


Figure 4.10: Temperature difference between the maximum and minimum temperatures of cells across (a) Row 1, (b) Row 2, (c) Row 3 and (d) Row 4.

4.4.2 Nozzle Slit Length Analysis

The parameters for test number 1, 6, and 7 are provided in Table 3.2 and the effects of changing the length of the nozzle slit on the maximum temperature and the temperature uniformity are represented by Figure 4.11. The maximum temperature of the battery pack is shown in Figure 4.11a. It can be seen that as the length of the nozzle and subsequently, the length of the nozzle slit increases the maximum temperature of the battery pack reduces from 37.7 to 34.4 °C, a decrease of 9.4%. However, the average maximum temperature of all the cells in the battery pack (Figure 4.11c) slightly increases as the length of the nozzle slit is increased. The average maximum temperature only increased from 30.1 to 30.4 °C, which amounts to an increase of 1%.

The change in the maximum temperature difference between the lowest and highest temperature in the battery pack is shown in Figure 4.11b. It can be seen from the figure that by increasing the length of the nozzle slit, the maximum temperature difference also reduces from 12.6 to 9 °C, a decrease of 39.3%. Additionally, the average temperature difference for all the cells, shown in Figure 4.11d, also reduce from 3.4 to 3.1 °C (or ~11.2%).

The results of this analysis show that test number 1 has lowest maximum temperature and the highest temperature uniformity. Therefore, the optimum length of the separating plate is 121 mm and the optimum length of the nozzle slit is 88 mm.

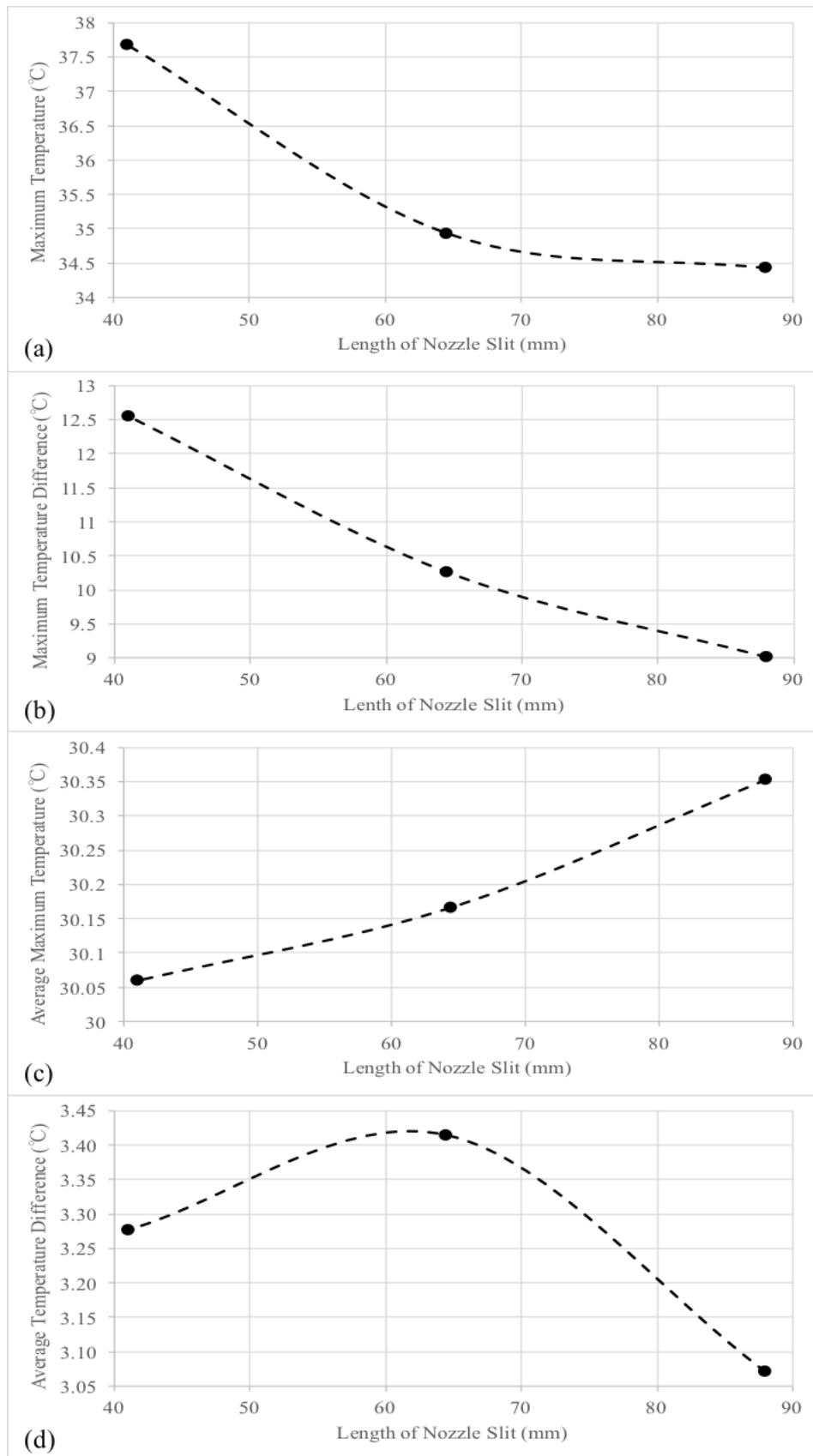


Figure 4.11: (a) Maximum temperature, (b) maximum temperature difference, (c) average maximum temperature, and (d) average temperature difference across the battery pack for test numbers 1, 6 and 7 in Table 3.2.

4.4.3 Reynolds Number Study

The results of separating plate and nozzle slit length analysis show that test number 1 is the optimum configuration in terms of maximum temperature and temperature uniformity within the battery pack. However, Figure 4.10 shows that there are 3 cells in test number 1 that exhibit a temperature difference between the maximum and the minimum temperature of more than 5 °C. Also, Figure 4.11b shows that the maximum temperature difference of test number 1 battery pack is 9 °C. Therefore, to increase the temperature uniformity of the battery pack, a Reynolds number study was carried out and the parameters are provided in Table 3.3.

The results shown in Figure 4.12 indicate that there is no dramatic reduction in the maximum temperature and temperature non-uniformity after Reynolds number of 7440. At the Reynolds number of 7440, the maximum temperature of the battery pack (Figure 4.12a) reduces to 28.1 °C from 34.4 °C, a reduction of 18.3%. The maximum temperature difference (Figure 4.12b) of the battery pack also reduces from 9 to 4.1 °C. This results in an increase in the temperature uniformity by 54.6%. Additionally, the average maximum temperature (Figure 4.12c) also reduces from 30.4 to 26.3 °C and the average temperature difference reduces from 3.1 to 1.6 °C (Figure 4.12d). Therefore, the results indicate that the optimum Reynolds number is 7440.

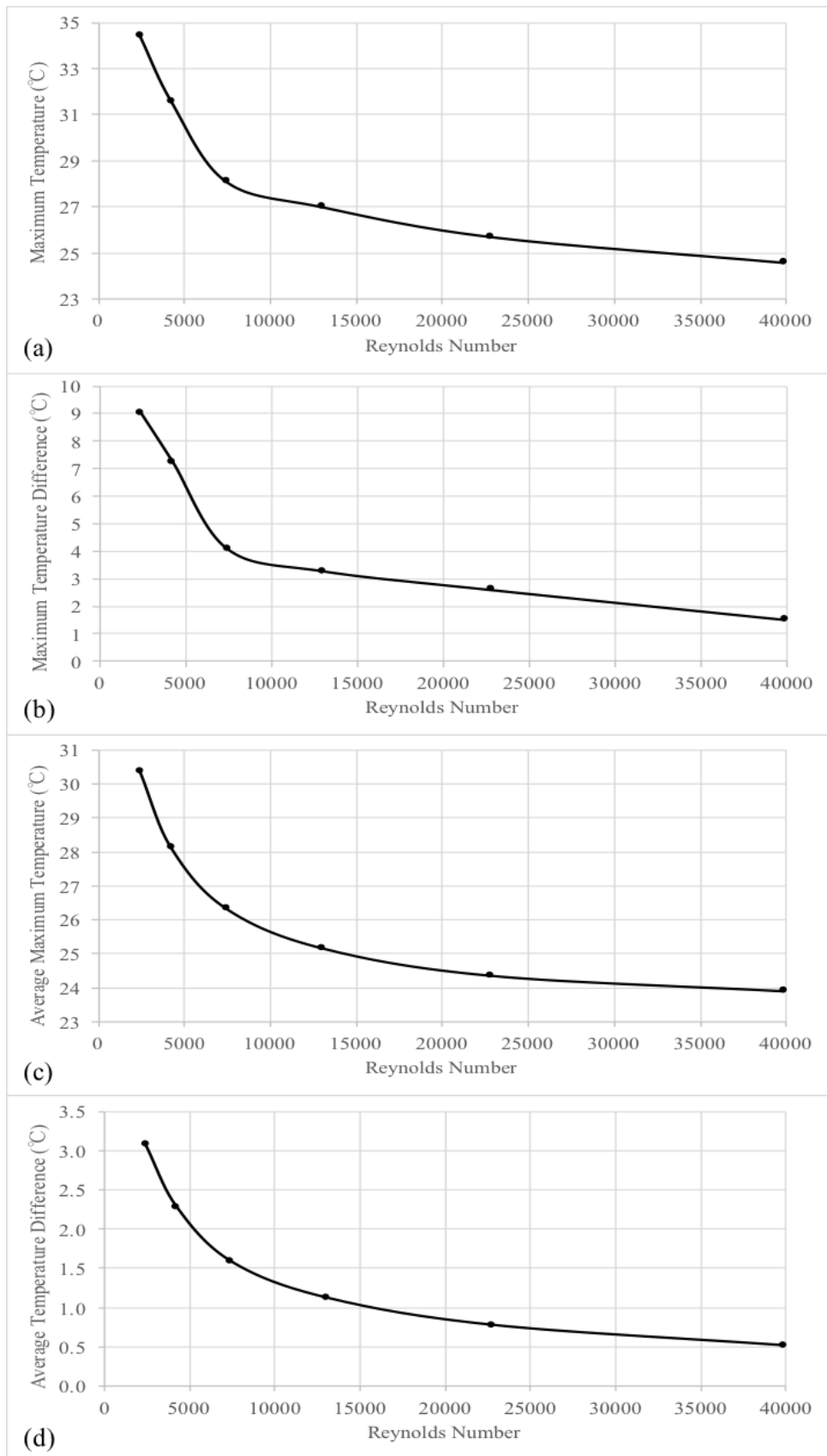


Figure 4.12: (a) Maximum temperature, (b) maximum temperature difference, (c) average maximum temperature, and (d) average temperature difference across the battery pack for test numbers 8 to 13 in Table 3.2.

4.5 Jet Inlet and Multiple Vortex Generator Study for Case A

4.5.1 Jet Inlet Analysis

A summary of the comparison of results from Case A1 and Case A is given in Table 4.3. The maximum temperature in the table (T_{\max}) represents the maximum temperature of the whole battery pack and not a particular cell. Similarly, the temperature difference (T_{diff}) represents the difference between the maximum temperature of the battery pack and the minimum temperature of the battery pack. The temperature difference per cell ($T_{\text{diff_cell}}$) in the tables represents the cell with the highest temperature difference in the battery pack. The average maximum temperature (T_{\max_ave}) provides the averages of the maximum temperatures of each cell and similarly, the average temperature difference ($T_{\text{diff_ave}}$) gives the averages of the temperature differences between the maximum and minimum temperatures of each cell. Note that a higher temperature difference equates to lower temperature uniformity in the battery pack and a lower temperature difference equates to a higher temperature uniformity. A negative value of the percentage difference means that the maximum temperature or the temperature difference is higher, whereas, a positive value shows that the maximum temperature or temperature difference is lower.

Table 4.3: Comparison of Case A1 with Case A.

Parameters	Case A	Case A1	Percentage Difference (%)
T_{\max} (°C)	31.6	31.7	-0.489
T_{diff} (°C)	7.25	7.45	-2.66
T_{\max_ave} (°C)	28.1	27.9	0.941
$T_{\text{diff_ave}}$ (°C)	2.28	2.35	-3.13
$T_{\text{diff_cell}}$ (°C)	4.94	5.76	-16.7

It can be seen from Table 4.3 that there are minute differences in the maximum temperatures and average maximum temperatures of Case A1 compared to Case A. The temperature difference of the Case A1 configuration increased by only 2.66% and the average temperature

difference of all the cells increases by 3.13%. The contours of velocity, turbulence kinetic energy and temperature are shown in Figure 4.13.

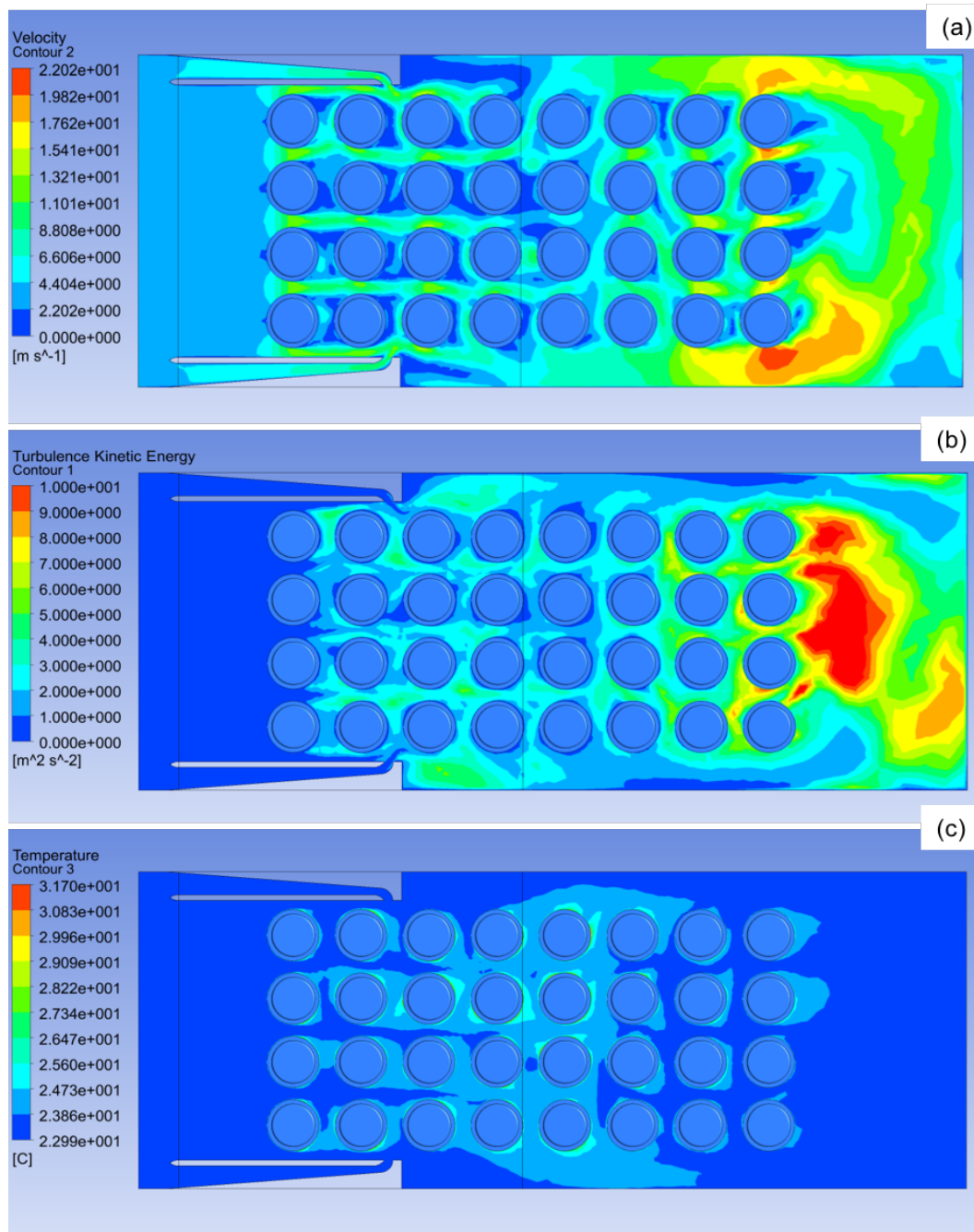


Figure 4.13: Contours of (a) velocity, (b) turbulence kinetic energy, and (c) temperature in the horizontal plane at 52 mm from the base of the battery pack for Case A1.

It can be seen from Figure 4.13a that the air entering from the jet inlet forces the air to enter into the empty spaces between the adjacent cells. Additionally, the air flows towards the gap beside the first row and last row of cells (created due to the jet inlet). This suggests that there

is increased turbulence and mixing near the 2nd and the 3rd columns of cells. To investigate the flow of turbulence, the turbulence kinetic energy contours were obtained as shown in Figure 4.13b. However, as seen in Figure 4.13b the turbulence kinetic energy reduces near the 4th and 5th columns of the cells. The rest of the columns experienced high turbulence kinetic energy due to the inlet plenum placed at the top of the battery pack. It can be seen from Figure 4.13c that the locations with relatively high turbulence kinetic energy experience low temperatures due to the incoming low temperature from the inlet plenum and jet inlets. This can be attributed to the intense mixing of the fluid flow which enhances heat and momentum transfer. This, in turn, increases the convection heat transfer coefficient, resulting in a higher rate of heat transfer. Therefore, the locations with higher turbulence kinetic energy have high heat transfer and low temperatures.

4.5.2 Multiple Vortex Generator Analysis

Table 4.4 provides a summary of the results of Case A2 compared to those of Case A. Similar to Case A1, the results of Case A2 show insignificant differences in the maximum temperatures of the battery pack and the average maximum temperatures for all the cells. The temperature uniformity of the Case A2 configuration is approximately the same as Case A, and the average temperature uniformity decreases by 7.4% in Case A2 configuration. The results of Case A2 are similar to those of Case A. Figure 4.14 provides the contours of velocity, turbulence kinetic energy, and temperature for Case A2.

Table 4.4: Comparison of Case A2 with Case A.

Parameters	Case A	Case A2	Percentage Difference (%)
T_{\max} (°C)	31.6	31.5	0.250
T_{diff} (°C)	7.25	7.29	-0.448
$T_{\max \text{ ave}}$ (°C)	28.1	28.1	-0.0869
$T_{\text{diff ave}}$ (°C)	2.28	2.45	-7.44
$T_{\text{diff cell}}$ (°C)	4.94	5.38	-8.93

It can be seen from Figure 4.14b that due to the turbulence created by the multiple vortex generators, the cells in the 1st two columns experience high turbulence. However, the turbulence energy dissipates away quickly as the flow moves to the 4th and 5th column of cells. From Figure 4.14c it can be seen that temperature starts to increase after the 2nd column as the turbulence kinetic energy reduces and the cells in the 4th and 5th columns experience the highest temperatures. This is also because a higher turbulence and mixing near the cells in the 1st and 2nd columns causes a greater amount of fresh air to convect heat away from the cells in these columns and as a result the temperature of the air increases. Therefore, less amount of fresh air is available to convect heat away from the cells in the 4th and 5th columns. This reduces the convection of heat, thereby, increasing the maximum temperatures of the cells. So even though the cells near the vortex generators have a lower temperature and a high-temperature uniformity, the overall impact of this is very low because the cells in the middle of the battery pack have low uniformity and high temperature.

By comparing Case A1 (Figure 4.13b) and Case A2 (Figure 4.14b), it can be seen that Case A1 displays higher turbulence kinetic energy across the entire battery pack compared to Case A2, which is why Case A1 exhibits an overall lower average maximum temperature. Additionally, comparing Figure 4.13b and 4.14b, it can be seen that the higher temperature air is forced out towards the sides of the battery pack, rather than traveling axially (as in Figure 4.14b), which also lowers the average maximum temperature and the average temperature difference of the battery pack. This is because, as shown in Figure 4.13a, the jet inlet creates an empty space in front of it, and the air tends to move towards that empty space.

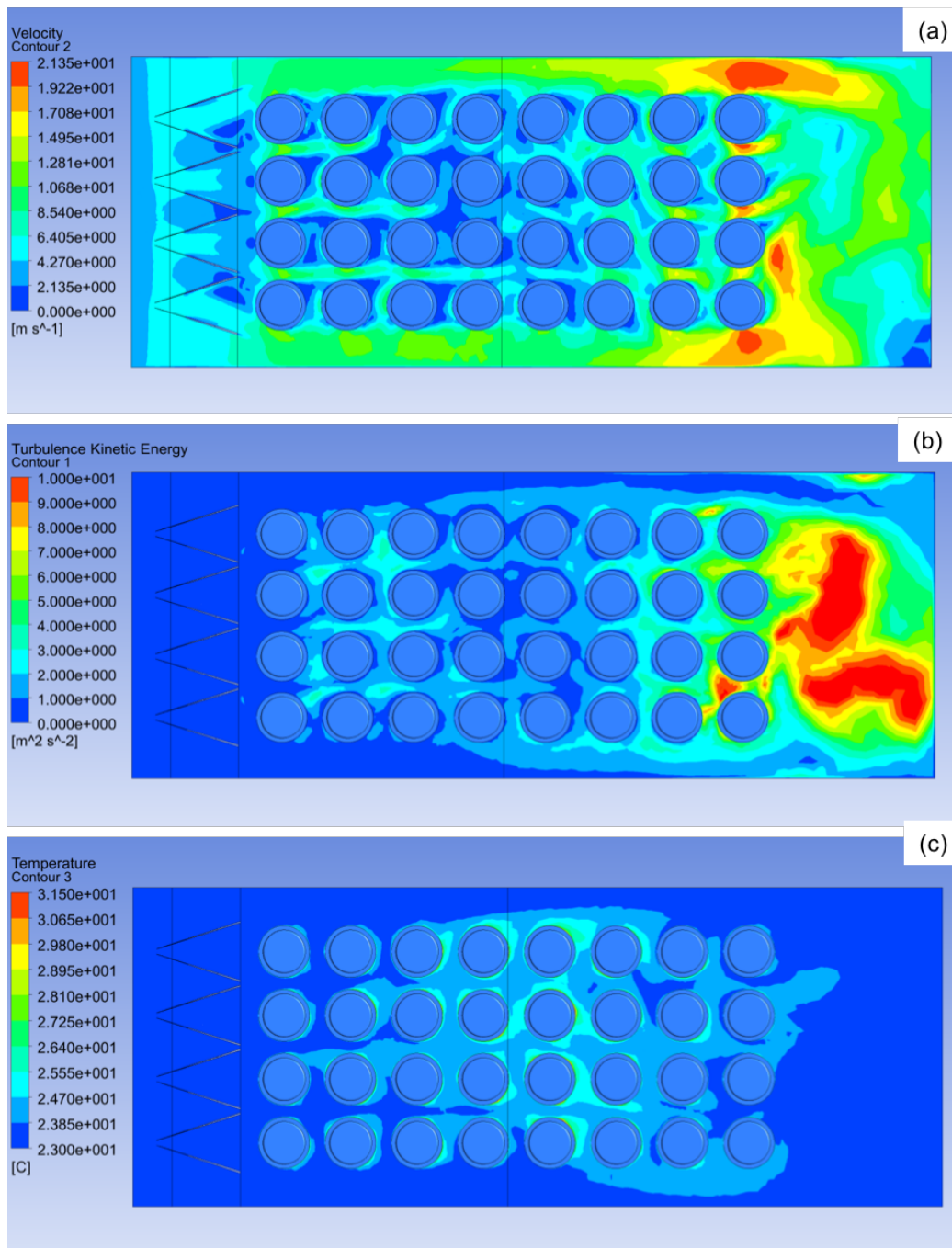


Figure 4.14: Contours of (a) velocity, (b) turbulence kinetic energy, and (c) temperature in the horizontal plane at 52 mm from the base of the battery pack for Case A2.

4.5.3 Jet Inlet and MVG Analysis

Table 4.5 provides the summary of the results of Case A3 compared with Case A. It can be seen that by adding jet inlets in combination with the MVGs, the results have improved significantly. The maximum temperature of the battery pack is by 4.96% to 30 °C and the

temperature difference of the battery pack decreased by 21.5%. Additionally, the cell with highest temperature difference exhibited a temperature difference of 4.13 °C, whereas, the cell in Case A exhibited a temperature difference of 4.94 °C. An improvement of 16.3%. Detailed contours of velocity, turbulence kinetic energy, and temperature for Case A3 are provided in Figure 4.15 and contours of Case A are provided in Figure 4.16, for comparison purposes.

Table 4.5: Comparison of Case A3 with Case A.

Parameters	Case A	Case A3	Percentage Difference (%)
T_{\max} (°C)	31.6	30.0	4.96
T_{diff} (°C)	7.25	5.69	21.5
$T_{\max \text{ ave}}$ (°C)	28.1	27.7	1.58
$T_{\text{diff ave}}$ (°C)	2.28	2.34	-2.33
$T_{\text{diff cell}}$ (°C)	4.94	4.13	16.3

It can be seen from the comparison of Case A3 (Figure 4.15b) and Case A (Figure 4.16b) that by incorporating jet inlets and vortex generators into the battery pack the turbulence kinetic energy across the battery has significantly increased, and at the same mass flow rate the maximum temperature has reduced and temperature uniformity increased significantly. This increased turbulence in the battery pack increases the amount of heat convected away from the cells. The jet inlets also provide fresh air with the inlet temperature of the cells at the middle of the battery pack, which, as shown in Figure 4.15c results in reduced temperature at the hotspots observed in previous configurations and the baseline configuration (Figure 4.16c). It can be seen by comparing Figure 4.15a and Figure 4.16a that due to MVGs and jet inlets there is a higher amount of mixing of air, that enables the air to pass between the spaces of adjacent cells. Thereby, convecting the heat away from the locations that previously experienced less convection.

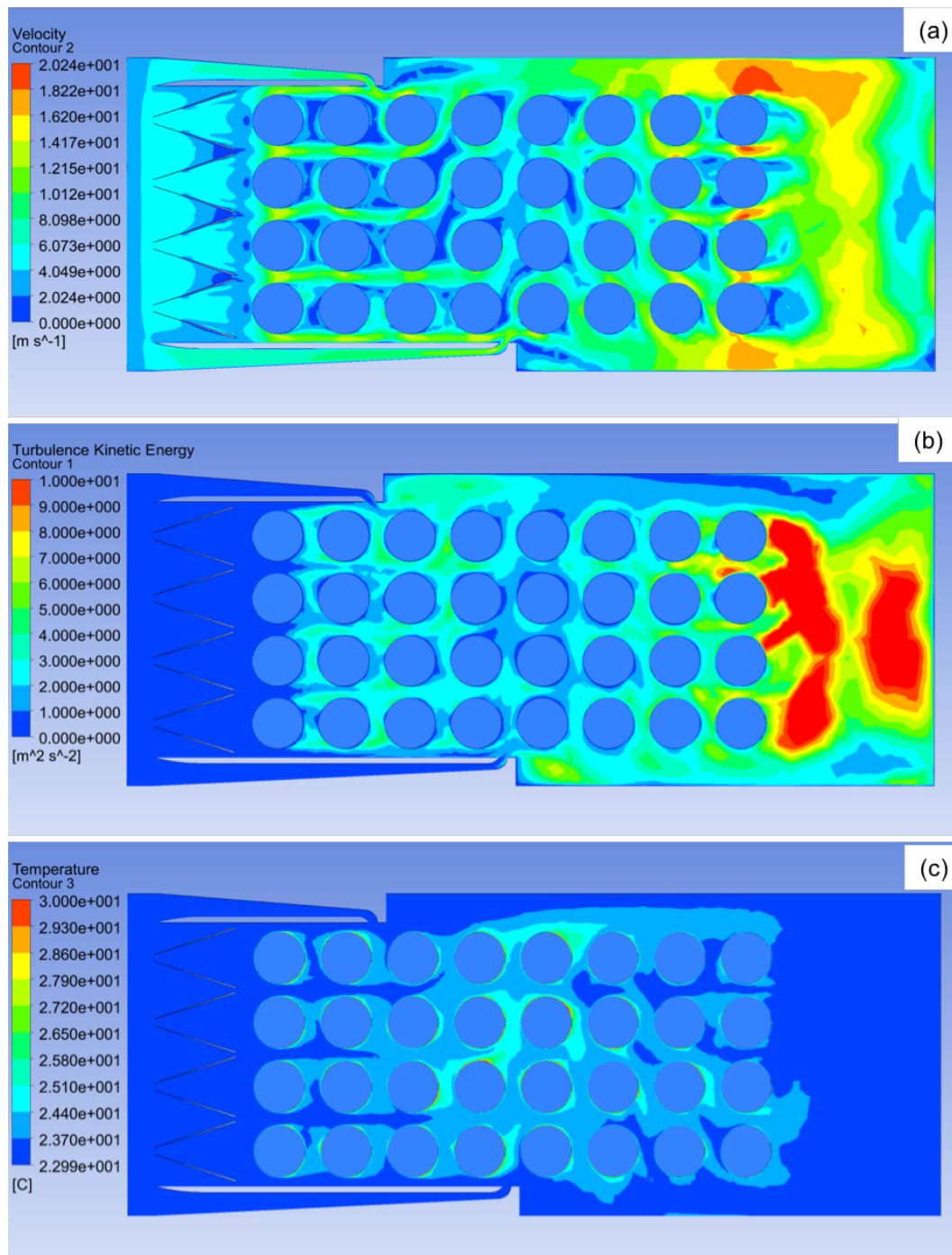


Figure 4.15: Contours of (a) velocity, (b) turbulence kinetic energy, and (c) temperature in the horizontal plane at 52 mm from the base of the battery pack for Case A3.

By comparing Case A2 (Figure 4.14b) and Case A3 (Figure 4.15b), it can be observed that in Case A3 configuration the whole battery pack experiences increased turbulence kinetic energy instead of just the first two columns of Case A2. In addition to this, the temperature distribution is more uniform in Case A3 (Figure 4.15c) across the battery pack, when compared to Case A2

(Figure 4.14c), resulting in an increased temperature uniformity. This is because, in Case A3 (Figure 4.15a), it can be seen that the jet inlets change the direction of the flow. This allows the air to pass through the gaps between adjacent cells and increase mixing of air, rather than flowing in a straight direction as in Case A2 (Figure 4.14a).

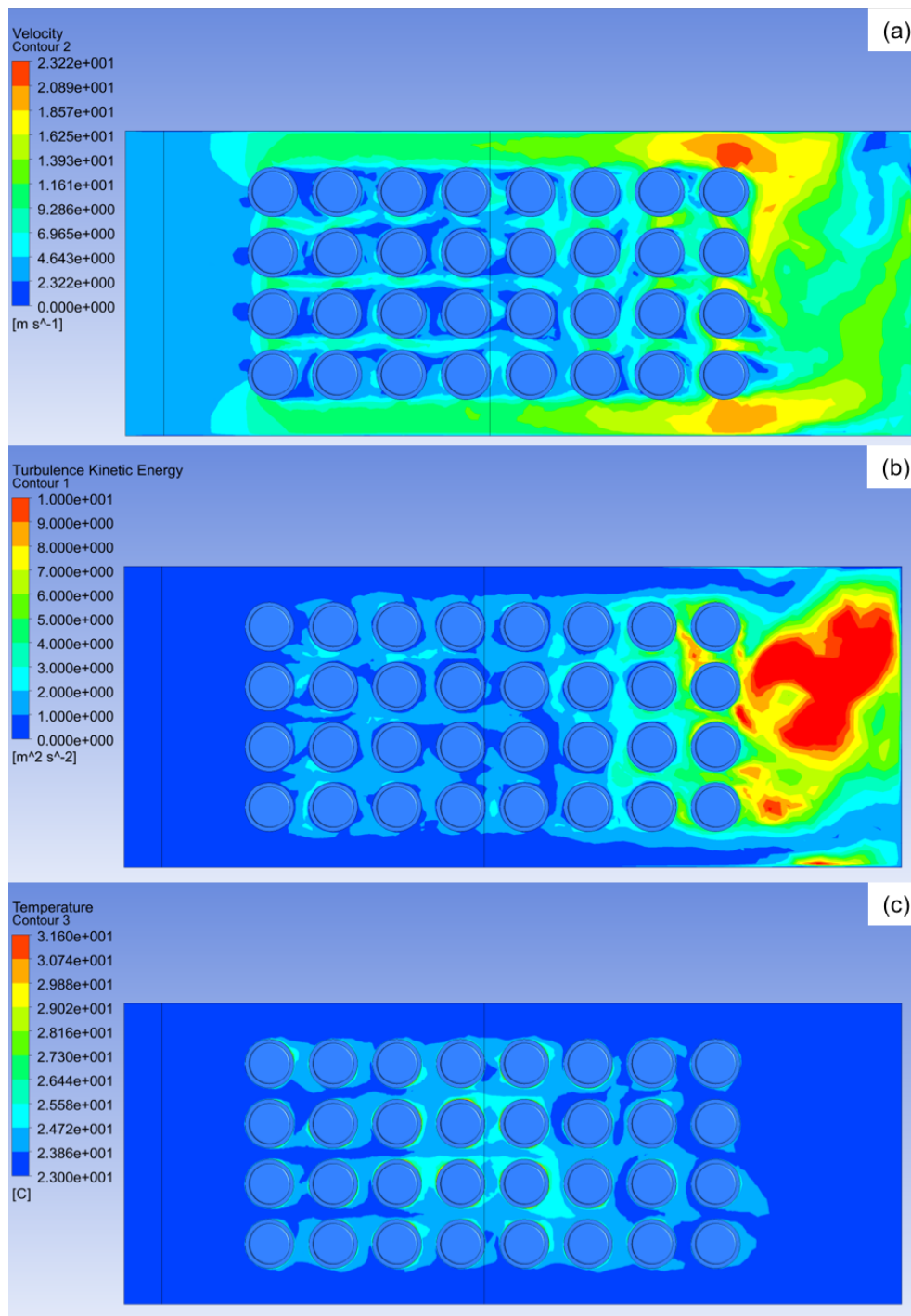


Figure 4.16: Contours of (a) velocity, (b) turbulence kinetic energy, and (c) temperature in the horizontal plane at 52 mm from the base of the battery pack for Case A.

4.6 Jet Inlet and Multiple Vortex Generator Study for Baseline (Case D)

4.6.1 Jet Inlet and Multiple Vortex Generator Analysis

A summary of the results obtained from Case D1 relative to those of Case D (baseline case) is provided in Table 4.6.

Table 4.6: Comparison of Case D1 with Case D (baseline case).

Parameters	Case D (Baseline)	Case D1	Percentage Difference (%)
T_{\max} (°C)	30.4	29.5	2.92
T_{diff} (°C)	6.39	5.89	7.76
T_{\max_ave} (°C)	26.9	26.6	1.16
$T_{\text{diff_ave}}$ (°C)	2.22	1.81	18.4
$T_{\text{diff_cell}}$ (°C)	5.24	4.35	17.1

The temperature difference between the maximum temperature and minimum temperature of the battery pack has been reduced by 7.8% in Case D1. However, the value of 5.89 °C is still higher. Additionally, the cell with the highest temperature difference between the maximum temperature and the minimum temperature in Case D1 exhibited a temperature difference of 4.35 °C, whereas in Case D the temperature difference recorded was 5.24 °C, a reduction of 17.1%. For an in-depth analysis, the contours of velocity, turbulence kinetic energy, and temperature for Case D are shown in Figure 4.17 and for Case D1 in Figure 4.18.

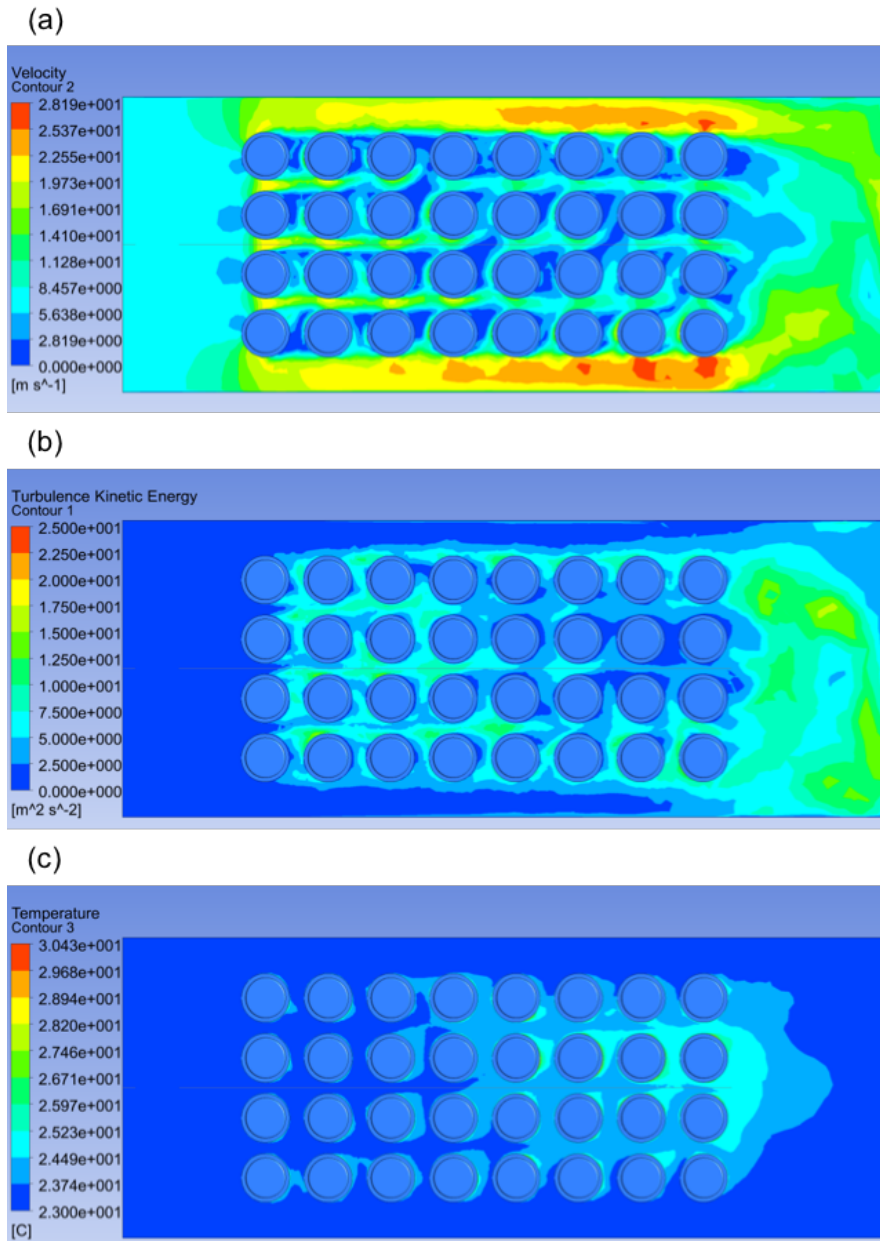


Figure 4.17: Contours of (a) velocity, (b) turbulence kinetic energy, and (c) temperature in the horizontal plane at 52 mm from the base of the battery pack for Case D.

It can be seen from Figure 4.17a that the flow tends to move in between the rows of the cells, due to which there are regions between the cells that experience less airflow, resulting in lower heat convection and subsequently higher temperature at those regions. In addition, the turbulence created from the cells (Figure 4.17b), causes more mixing which forces airflow into the dead air regions in the first half of the battery pack. The airflow convects away some of the heat resulting in a lower temperature of cells (Figure 4.17c). Moreover, it can be seen from the

temperature contours (Figure 4.17c) that the temperature of the air keeps increasing as it moves forwards towards the latter half of the battery pack. Therefore, there is a requirement to inject fresh air (low-temperature air) into the battery pack at different intervals, in order to increase the amount of heat the airflow convects away from the cells. It can also be seen from Figure 4.17c that the heat is confined within the cell boundaries by the high-velocity flow (Figure 4.17a) at the sides of the battery pack.

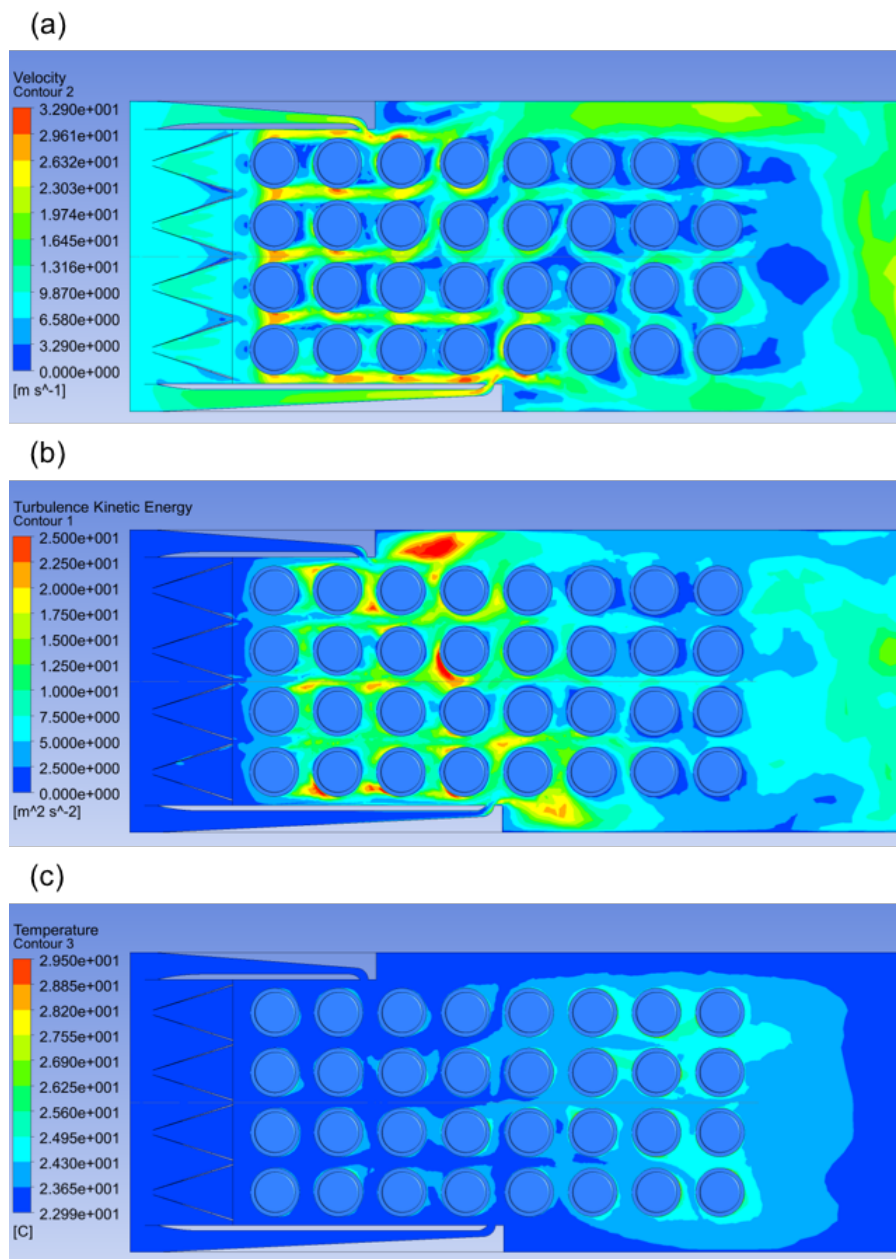


Figure 4.18: Contours of (a) velocity, (b) turbulence kinetic energy, and (c) temperature in the horizontal plane at 52 mm from the base of the battery pack for Case D1.

Figure 4.18 shows the results of the combined effects of jet inlets and MVGs. The results indicate that there is an increase in the turbulence kinetic energy (Figure 4.18b) when compared to Case D (Figure 4.17b). This has resulted in increased mixing and allows higher amounts of airflow to enter the empty spaces of adjacent cells, as shown in Figure 4.18a. It can also be seen from Figure 4.18c that the locations with relatively high turbulence kinetic energy experience low temperatures due to the incoming low-temperature airflow from the jet inlets. This can be attributed to the intense mixing of the fluid flow which enhances heat and momentum transfer. This, in turn, increases the convective heat transfer coefficient (He et al., 2014b), resulting in a higher rate of heat transfer. Therefore, the locations with higher turbulence kinetic energy have high heat transfer and low temperatures. It can be seen from Table 4.6 that that addition of jet inlets in combination with the delta winglet multiple vortex generators has improved the temperature uniformity within the battery pack and each cell.

Table 4.7 summarizes the results obtained from Case D2 described above in Section 3.1.5. In addition, the contours of velocity, turbulence kinetic energy, and temperature of Case D2 are shown in Figure 4.19. It can be seen that due to the addition of 3rd jet inlet, a significant reduction in the maximum temperature and improvements in the temperature uniformity have been achieved. The maximum temperature of the of the battery pack has reduced by 5.9% to 28.6 °C and the temperature difference of the battery pack has reduced by 23,7% to 4.87 °C. Additionally, 37.2% improvement has been recorded in the temperature uniformity in a single cell. Also, the temperature difference has reduced from 5.24 to 3.29 °C.

Table 4.7: Comparison of Case D2 with Case D (baseline case).

Parameters	Case D (Baseline)	Case D2	Percentage Difference (%)
T_{\max} (°C)	30.4	28.6	5.89
T_{diff} (°C)	6.39	4.87	23.7
T_{\max_ave} (°C)	26.9	26.3	2.30
$T_{\text{diff_ave}}$ (°C)	2.22	1.75	21.3
$T_{\text{diff_cell}}$ (°C)	5.24	3.29	37.2

By comparing the contours of Case D2 (Figure 4.19) with Case D1 (Figure 4.18), it can be seen that by adding jet inlet 3 there have been significant improvements in the latter half of the battery pack. By allowing the airflow to enter between the 6th and 7th columns of cells, the airflow from jet inlet considerably changes the flow of the air towards the adjacent rows, as shown in Figure 4.19a. Thereby, increasing the flow of the air in the dead air regions. Additionally, the gap created after jet inlet 2 also allows the airflow to move into this, shifting the flow directions towards the right side of the battery pack. Moreover, by comparing Figure 4.19c with Figure 4.18c, it can be seen that turbulence kinetic energy has increased across the whole battery pack in Case D2, whereas, in Case D1 there is very high turbulence in the first half of the battery pack and as the airflow moves forward into the second half the turbulence kinetic energy starts to dissipate. This increase in the turbulence kinetic energy across the battery pack increases the cooling and temperature uniformity within the battery pack as suggested by the results in Table 4.7.

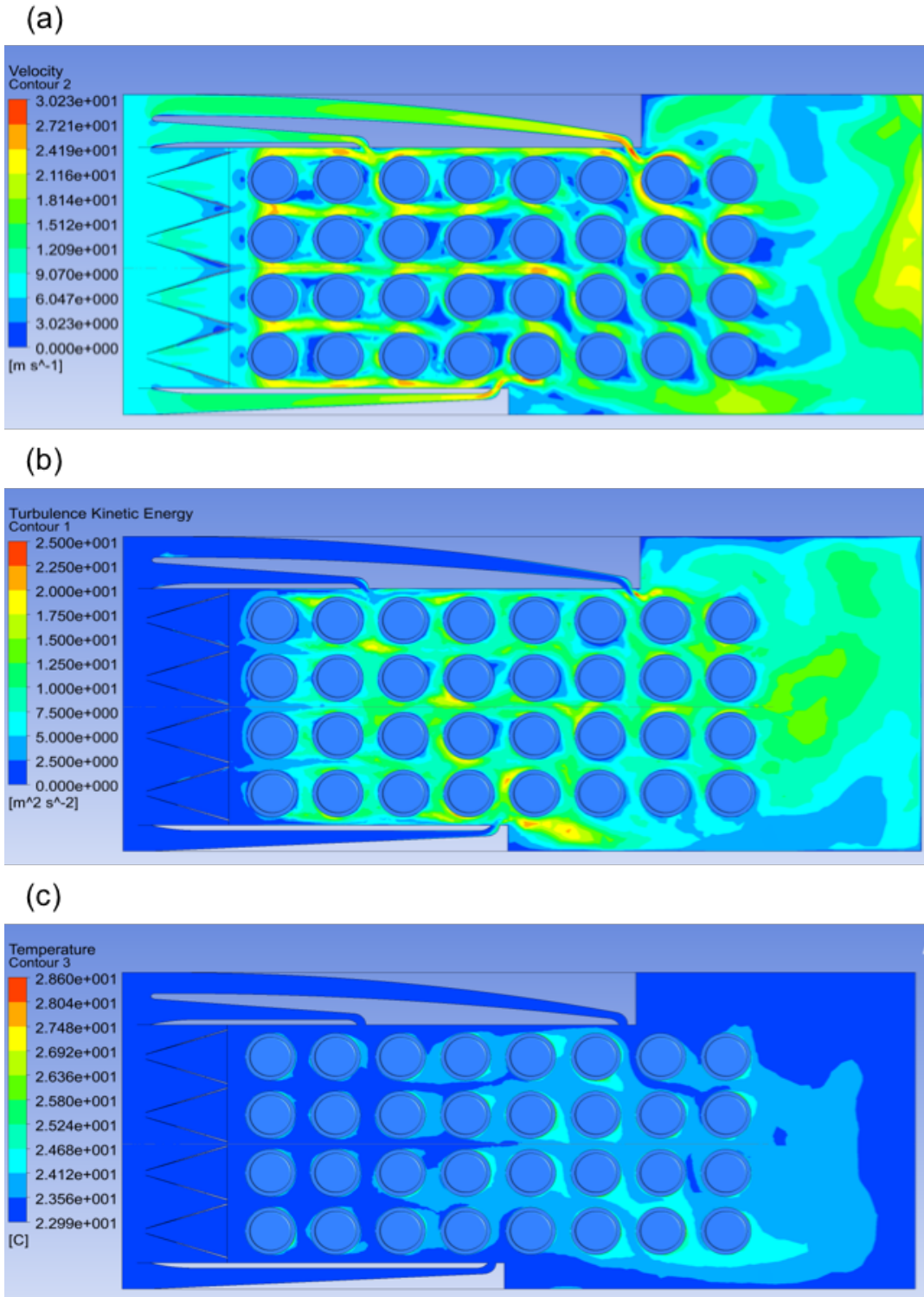


Figure 4.19: Contours of (a) velocity, (b) turbulence kinetic energy, and (c) temperature in the horizontal plane at 52 mm from the base of the battery pack for Case D2.

4.6.2 Vortex Generator Placement Analysis

In order to analyze the effects of the placement of vortex generators on the cooling and temperature uniformity of the battery pack, a comparison is made between Case D3 and Case D2. The results are summarized in Table 4.8 and the contours of velocity, turbulence kinetic energy, and temperature of Case D3 are shown in Figure 4.20. Note that a negative value of the percentage difference means that the maximum temperature or the temperature difference is higher, whereas, a positive value shows that the maximum temperature or temperature difference is lower.

Table 4.8: Comparison of Case D3 with Case D2.

Parameters	Case D2	Case D3	Percentage Difference (%)
T_{\max} (°C)	28.6	28.5	0.562
T_{diff} (°C)	4.87	4.92	-1.03
T_{\max_ave} (°C)	26.3	26.3	-0.0231
$T_{\text{diff_ave}}$ (°C)	1.75	1.85	-6.09
$T_{\text{diff_cell}}$ (°C)	3.29	3.57	-8.54

It can be seen from Table 4.8 that the placement of the vortex generator has a negligible impact on the maximum temperature and the average maximum temperature of the battery pack. Moreover, in Case D3, the temperature uniformity in the battery pack and for each cell has been reduced by placing the vortex generators in front of the cells rather than between the cell rows. The differences in temperature uniformity are, however, not significant as the temperature difference of the battery pack increases from 4.87 °C (in Case D2) to 4.92 °C (in Case D3), an increase of 1% and the average temperature difference increases from 1.75 to 1.85 °C, an increase of 6%. The temperature difference for a single cell also increases from 3.29 to 3.57 °C, which amounts to an increase of 8.5%.

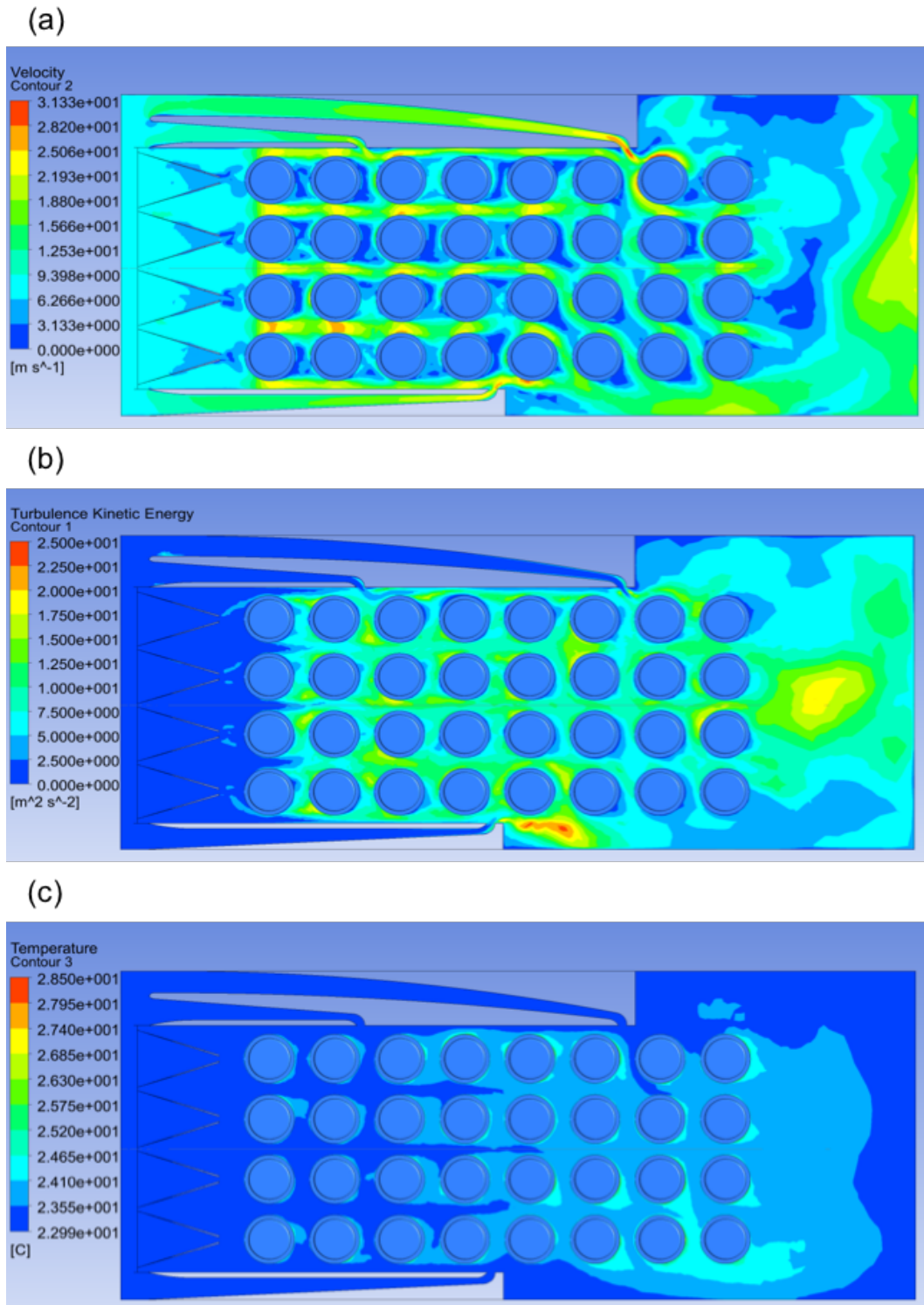


Figure 4.20: Contours of (a) velocity, (b) turbulence kinetic energy, and (c) temperature in the horizontal plane at 52 mm from the base of the battery pack for Case D3.

By comparing the contours of Case D2 (Figure 4.19) and Case D3 (Figure 4.20), it can be seen that the contours are very similar, which is also reflected in the results in Table 4.8. There is, however, a slight difference in the turbulence kinetic energy contours. It can be seen from

Figure 4.20b that by changing the placement of vortex generators to in front of the cells the turbulence kinetic energy before the 1st column of cells has been slightly reduced when compared to Figure 4.19b. This has a marginal effect on the flow of the air near the 1st and 2nd columns of cells, presented in Figure 4.20a. Comparing Figure 4.20a with Figure 4.19a, it can be seen that the cells in the 1st and 2nd columns in Figure 4.20a experience less amount of air in between adjacent cells. This slight difference between Case D2 and Case D3 results in the differences in the results seen in Table 4.8.

4.6.3 Vortex Generator Type Analysis

As stated earlier, there was also an attempt to evaluate the type of VG used. The delta wing (DW) vortex generators are most common have been used in heat transfer application in the past (Fiebig, 1998; Fiebig et al., 1986; Fiebig, 1995; Eaton, 1994; Tiggelback et al., 1994; Wang et al., 2002). In Case D4 the results obtained for the rectangular wing (RW) vortex generators compared with Case D2 (DW-MVG). The results are summarized in Table 4.9 and the contours of velocity, turbulence kinetic energy, and temperature of Case D4 are shown in Figure 4.21.

Table 4.9: Comparison of Case D4 with Case D2.

Parameters	Case D2	Case D4	Percentage Difference (%)
T_{\max} (°C)	28.6	29.1	-1.45
T_{diff} (°C)	4.87	5.35	-9.70
T_{\max_ave} (°C)	26.3	26.5	-0.728
$T_{\text{diff_ave}}$ (°C)	1.75	1.83	-4.53
$T_{\text{diff_cell}}$ (°C)	3.29	3.64	-10.6

It can be seen from Table 4.9 that the type of the vortex generator has an impact on the maximum temperature and the average maximum temperature of the battery pack. In Case D4, the temperature uniformity of the battery pack and of each cell has been reduced by using rectangular winglet vortex generators. The temperature difference of the battery pack increases

from 4.87 °C (in Case D2) to 5.35 °C (in Case D4), an increase of 9.7%, and the average temperature difference increases from 1.75 to 1.83 °C, an increase of 4.5%. The temperature difference for a single cell also increases from 3.29 to 3.64 °C, which amounts to an increase of 10.6%.

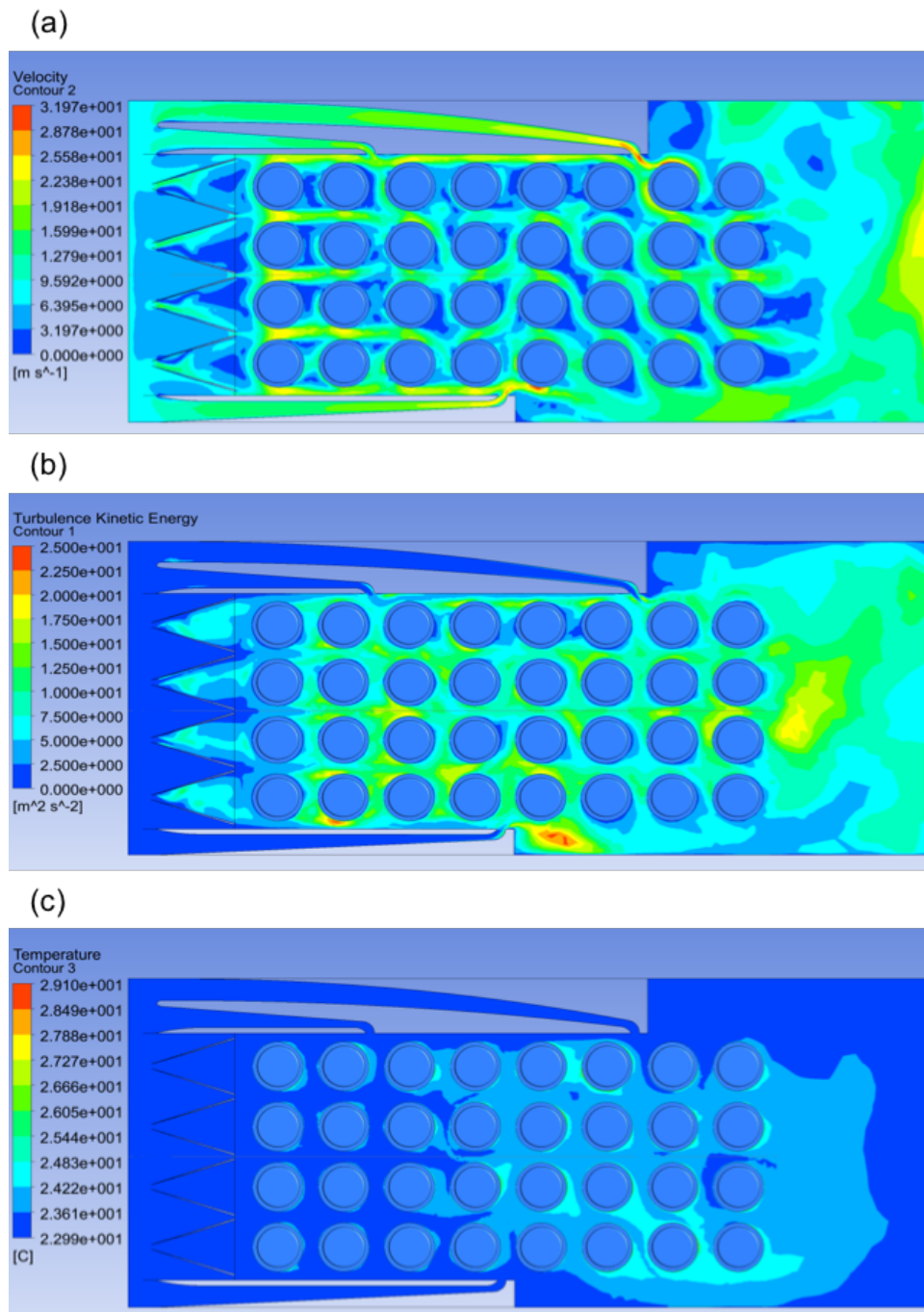


Figure 4.21: Contours of (a) velocity, (b) turbulence kinetic energy, and (c) temperature in the horizontal plane at 52 mm from the base of the battery pack for Case D4.

The contours of Case D4 are similar to the contours of Case D2. The difference near the 1st and 2nd columns of cells can be observed in the velocity contours of Case D4 (Figure 4.21a) and Case D2 (Figure 4.19a). It can be seen in Figure 4.21a that due to rectangular nature of the vortex generators, an increased blockage is introduced in the airflow path resulting in the air passing in between the cell rows at higher velocities. This, in turn, results in reduced flow of air between adjacent cells. This results in the reduced temperature uniformity as shown in Table 4.9.

Chapter 5: Conclusions and Recommendations

5.1 Summary of Results and Conclusions

In this thesis, concepts for improving air-cooling and temperature uniformity in simple battery packs are developed and investigated. The studies were performed by incorporating inlet plenum, jet inlets, and vortex generators into the proposed battery pack concepts. Numerical simulations were conducted for all the battery packs. Additionally, experiments were conducted to validate the numerical studies. The effectiveness of the new concepts was examined based on the results of the maximum temperature and temperature uniformity at both the cell level and the battery pack level. The results suggest that the addition of the inlet plenum and jet inlets, change the direction of the flow and eliminate the problem of recirculation and dead air regions between adjacent cells. Also, the vortex generators increase the turbulence levels of the incoming flow, resulting in improved momentum and heat transfer. A summary of the results and the conclusions drawn are as follows:

- Amongst all the battery pack configurations, Case D2 (which includes 3 jet inlets and delta winglet multiple vortex generators) achieved the highest cooling and temperature uniformity. Compared to the baseline battery pack, the maximum temperature of the battery pack was reduced by about 6% and the temperature difference between the maximum temperature and the minimum temperature exhibited by the battery pack was reduced by 24%. Additionally, there was improvement in the temperature uniformity at the cell level by about 37%.
- In examining the effects of the orientation of the inlet plenum and the cells, the results concluded that Case A (which has the inlet plenum at the top of the battery pack) is the most effective battery pack, when compared with Case B (which has the inlet plenum at the left side of the battery pack) and Case C (which has the inlet plenum at both sides

of the battery pack). This comparison was based on the maximum temperature and the temperature uniformity across the cells and battery pack. The results indicated that the maximum temperature in Case A is reduced by 9% compared to the baseline battery pack. The results also show an improvement of about 39% in the temperature uniformity compared to the baseline battery pack.

- For the Reynolds number study, the results revealed that beyond a Reynolds number of 7440, corresponding to the mass flow rate of 137 g/s, there was no dramatic change in the maximum temperature of the battery pack and the temperature uniformity in Case A.
- In modifying Case A, by incorporating vortex generators and jet inlets in the same configuration, the requirement of power and mass flow rate was reduced by up to 43%, as the optimum Reynolds number required was reduced from 7440 (mass flow rate of 137 g/s) to 4252 (mass flow rate of 78 g/s). The results showed that at Reynolds number of 4252, the temperature difference between the maximum temperature and the minimum temperature exhibited by the battery pack was reduced by 21.5%. Additionally, the cell with the highest temperature difference between the maximum temperature and the minimum temperature exhibited a temperature difference of 4.13 °C. This results in about 16% improvement in the temperature uniformity of a single cell.
- Additionally, the results concluded that the battery pack exhibits lower temperature and higher temperature uniformity when the vortex generators are placed in-between the cells rather than in front of the cells.
- Compared with the concept with rectangular winglet vortex generators, it was observed that the delta winglet vortex generators are more effective and exhibited lower

maximum temperatures and better temperature uniformity at both the pack level and the cell level.

- The results also concluded that the lowest maximum temperatures and best temperature uniformity was achieved when the air from the jet inlets was introduced in between the second and third columns (from the first jet inlet), fourth and fifth columns (from the second jet inlet), and sixth and seventh columns (from the third jet inlet).

The concepts developed and used in this study were able to limit the maximum temperature of the battery pack to 28.6 °C, which is a significant improvement over battery packs developed for similar batteries in the open literature. The developed battery pack concept also achieved the desired temperature uniformity at both the pack level and cell level to within 5 °C. It is concluded that this battery pack concept is simple, requires no moving parts and introduces mixing and turbulence in the air flow to provide an improved cooling and temperature uniformity in the battery pack.

5.2 Contributions

The contributions of this research are as follows:

- A new battery pack concept for cylindrical Li-ion cells was developed that incorporates jet inlets and vortex generators to increase turbulent mixing and eliminate the dead air zones within the battery pack. It significantly improves cooling and temperature uniformity without a significant penalty in fan power.
- A unique set of vortex generator arrays were developed to meet the research objective. The vortex generator array was constructed on both sides of the plate to increase the number of vortices created for the limited space.
- An array of jet inlets was developed to minimize the air mass flow rate requirement and hence, fan power. The locations of the jet inlets were strategically determined in order

to provide the highest amount of mixing of air and eliminate dead air zones between the adjacent cells.

5.3 Recommendations

Several recommendations can be made for future research as listed below:

- An experiment should be conducted that discharges the whole battery pack at once, in order to improve the results of the validation of the model.
- Thermal cameras can be used to get the temperature contours on the surface of the cells during the experimental study and validate it with the numerical studies.
- A study should be conducted to optimize the outlet shape and size of the jet inlets.
- This study focuses on conventional vortex generators to confirm its feasibility in the battery pack. Based on this, a study is required to incorporate more complex and different types of vortex generators into the battery pack and study its effect.
- A study should also be conducted that implements the techniques of jet inlets and vortex generators to a larger battery pack with increased number of cells.
- Based on the techniques of jet inlets and vortex generators, a study should be conducted in which these techniques are applied to the battery packs with larger cells such as the 26650 and 42120 cylindrical cells.
- The battery pack concept developed should be scaled-up to meet the power requirements of a realistic electric vehicle.

Appendices

Appendix I

In this appendix, basic definitions related to electric batteries are provided.

Cells and Batteries – A cell is a single unit which converts the chemical energy into electrical energy, whereas, a battery is the collection of electrochemical cells which either connect in series or parallel (CG, n.d.).

Cells, Modules and Battery Packs – EVs and HEVs contain battery packs of high voltage to power the cars. These battery packs consist of individual modules connected in either series or parallel. The modules are made up of several cells connected in series or parallel. A cell is the smallest unit and packaged form a battery can take and it usually provides 1 to 6 V (Team, 2008).

Secondary and Primary Cells – Primary cells are the one that cannot be recharged and secondary cells are the ones that are rechargeable. Therefore, the cells used in EVs and HEVs are all secondary cells (Team, 2008).

C-rates and E-rates – The charging and discharging currents of a cell are expressed in C-rates. A 1 C rating means that a 1 Ah cell will provide 1 A of current for 1 hour. Similarly, for 2 C, a 1 Ah cell will provide 2 A of current for 0.5 hours (or 30 minutes). Likewise, the E-rate describes the charging and discharging power (Team, 2008).

State of Charge (SOC) – This is an expression that provides a percentage measure of the capacity of the cell or battery to the maximum capacity. This is usually calculated by integrating the current with respect time. The integral provides the aggregate number of

coulombs, N_C , that is transported into or out of the battery. The equations used for calculating the SOC are as follows (Panchal, 2016):

$$N_C = \int_{t_0}^t I dt \quad (\text{A.1})$$

The total number of coulombs are expressed as capacity, C , following a simple unit conversion.

$$C = \int_{t_0}^t \frac{I}{3600} dt \quad (\text{A.2})$$

Therefore, SOC is estimated by considering the initial state of charge (SOC_0) and the capacity consumed during the usage of the battery as a percentage of the maximum capacity (C_{max}).

$$SOC = SOC_0 - \frac{Q}{Q_{max}} \times 100\% \quad (\text{A.3})$$

Depth of Discharge (DOD) – The amount of capacity that has already been discharged and is expressed as a percentage with respect of the maximum capacity. A discharge up to at least 80% of maximum capacity is considered as a deep discharge (Team, 2008).

Terminal Voltage (V) – The voltage across the terminals of the battery when a load is applied. It varies depending on the SOC and the current applied while charging or discharging (Team, 2008).

Open-circuit Voltage (V) – The voltage across the terminals of the battery when no load is applied. It depends on the state of charge and increases or decreases according to it (Team, 2008).

Internal Resistance (IR) – Internal resistance, also considered as the ohmic resistance of the cell, is an immediate change in the voltage once a current step is drawn from a cell in an equilibrium position. It is the summation of the ohmic, activation and diffusion polarization

resistances (Park, 2012). The voltage drop is characterized as (a) IR drop due to the flow of current across the internal resistance of the battery, (b) activation polarization due to the different retarding factors inherent in the kinetics of an electrochemical reaction. It is similar to the work that the ions required for overcoming the junction between the electrodes and electrolytes and (c) concentration polarization due to the resistance encountered because of the mass transfer (diffusion) process by which the ions are transported across the electrolyte from one electrode to the other (Panchal, 2016). Figure 2.1 shows a typical polarization curve of the battery.

Nominal Voltage (V) – Nominal voltage (also referred as the “normal” voltage) is the reported voltage or the reference voltage of the cell (Team, 2008).

Cut-off Voltage (V) – This is the minimum allowable voltage and defines the “empty” state of the battery (Team, 2008).

Charge Voltage (V) – This is the voltage that the battery charges to when it reaches its maximum capacity. Charging of the battery is usually done at a constant current until it reaches the charge voltage and then the battery charges at a constant voltage, and the current is reduced until it gets very low (Team, 2008).

Float Voltage (V) – This is the voltage at which the battery is kept to after it has been fully charged (that is up to 100% SOC) to maintain the maximum capacity by compensating for the self-discharge of the battery (Team, 2008).

Specific Energy (Wh/kg) – This is the nominal battery energy per unit mass. It is also referred as the gravimetric energy density. This is the characteristic of the chemistry of the battery and its packaging. In addition to providing the energy consumption of the vehicle, it also determines the weight of the battery that will be required to achieve a given electric range (Team, 2008).

Specific Power (W/kg) – This is the maximum available power per unit mass. This is the characteristic of the chemistry of the battery and its packaging (Team, 2008).

Energy Density (Wh/L) – This is the nominal battery energy per unit volume. This is the characteristic of the chemistry of the battery and its packaging (Team, 2008).

Power Density (W/L) – This is the maximum available power per unit volume. This is the characteristic of the chemistry of the battery and its packaging (Team, 2008).

Appendix II

In this section, the CAD models (Figure A.1) and schematics (Figure A.2) of the better battery pack concept developed in this study are presented. It incorporates 3 jet inlets and an array of delta winglet multiple vortex generators. It has a low maximum temperature and high-temperature uniformity and compares favorably with similar battery packs in the open literature.

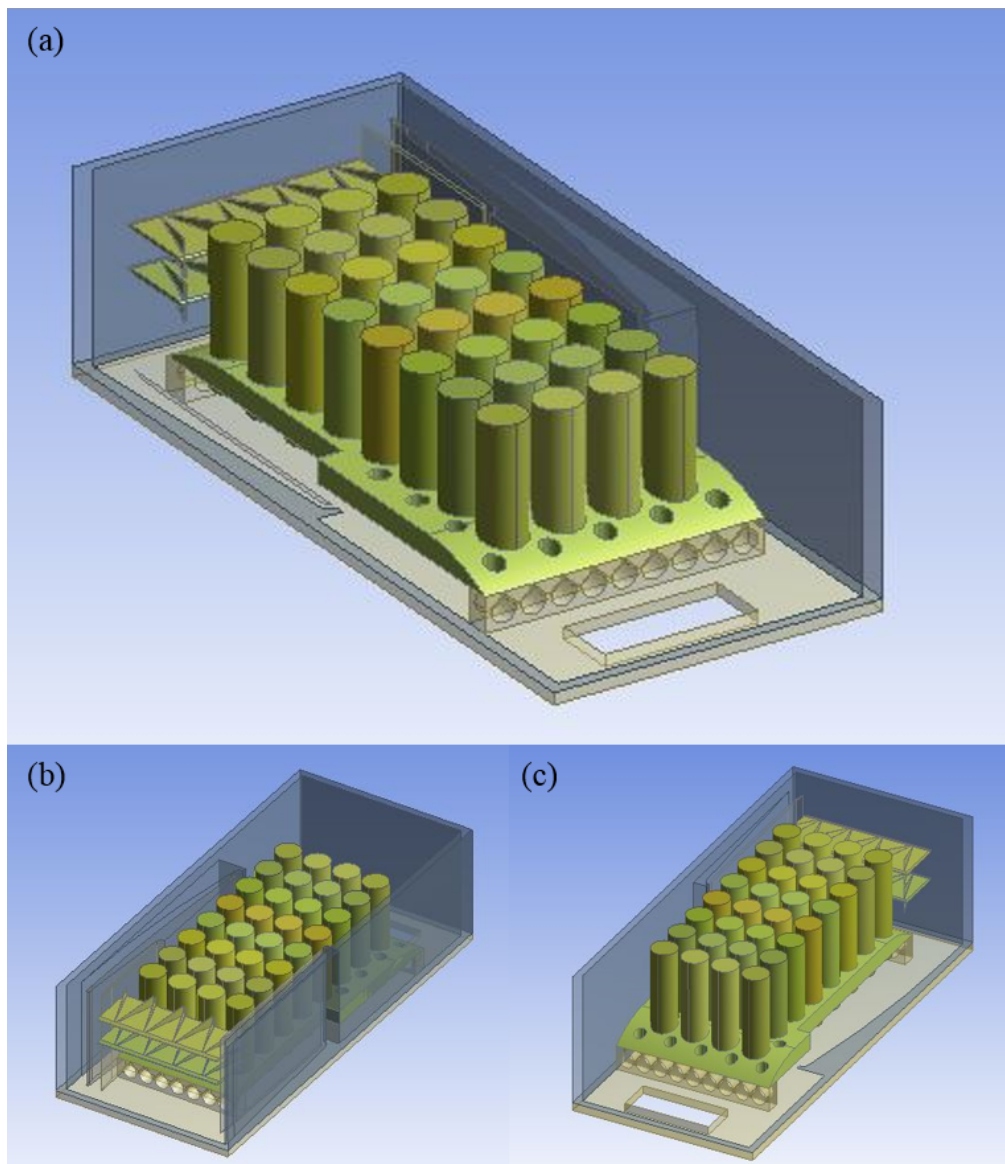


Figure A.1: Various views of the CAD model of the better pack concept developed.

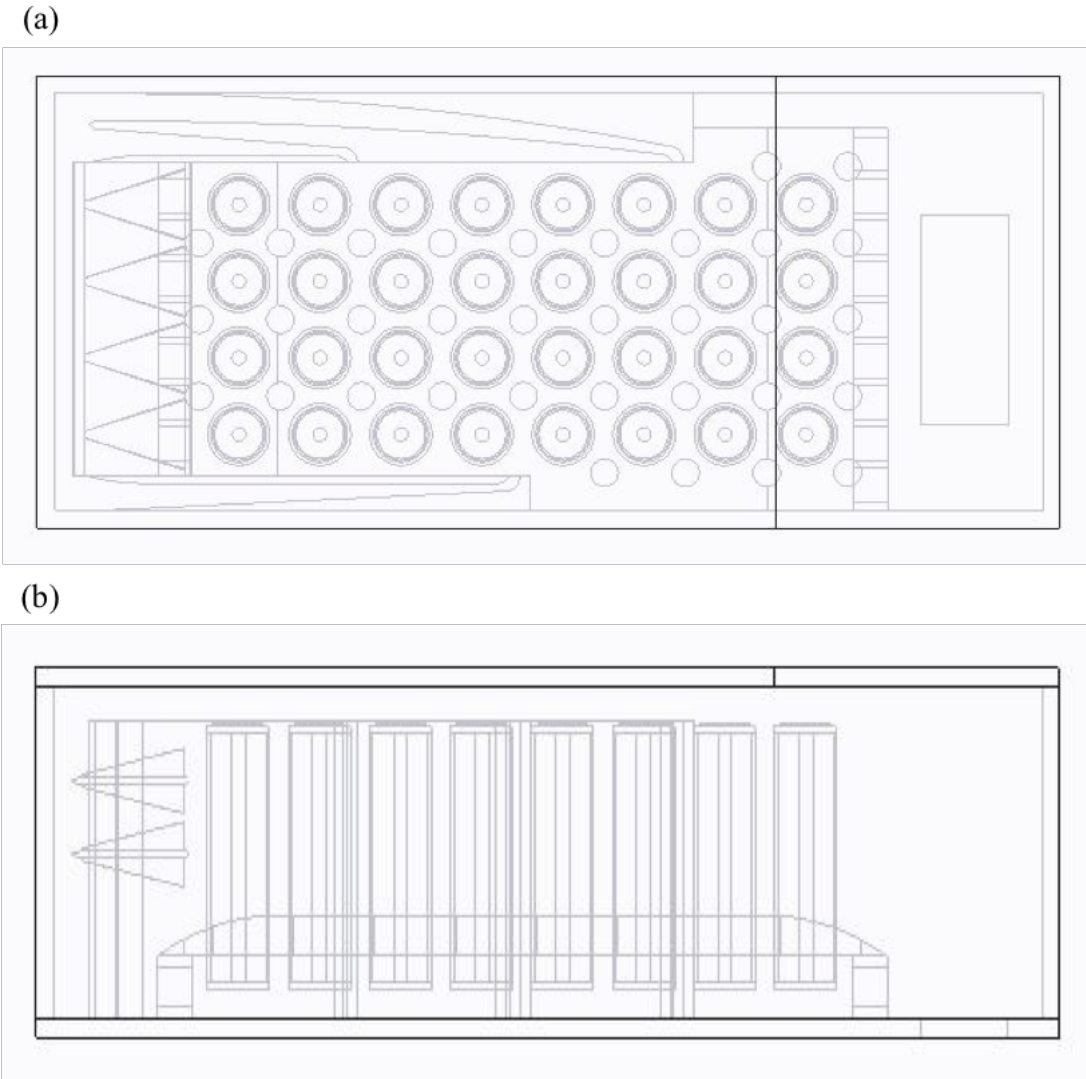


Figure A.2: Schematic of the better pack concept developed: (a) plan view and (b) side view.

References

Abdul-Quadir, Y., Laurila, T., Karppinen, J., Jalkanen, K., Vuorilehto, K., Skogström, L. and Paulasto-Kröckel, M., 2014a. Heat generation in high power prismatic Li-ion battery cell with LiMnNiCoO₂ cathode material. *International Journal of Energy Research*, 38(11), pp.1424-1437.

Abdul-Quadir, Y., Laurila, T., Karppinen, J. and Paulasto-Kröckel, M., 2014b. Thermal simulation of high-power Li-ion battery with LiMn_{1/3}Ni_{1/3}Co_{1/3}O₂ cathode on cell and module levels. *International Journal of Energy Research*, 38(5), pp.564-572.

Al-Hallaj, S., Kizilel, R., Lateef, A., Sabbah, R., Farid, M. and Selman, J.R., 2005, September. Passive thermal management using phase change material (PCM) for EV and HEV Li-ion batteries. In *Vehicle Power and Propulsion, 2005 IEEE Conference* (pp. 5-pp). IEEE.

Al-Hallaj, S. and Selman, J.R., 2002. Thermal modeling of secondary lithium batteries for electric vehicle/hybrid electric vehicle applications. *Journal of power sources*, 110(2), pp.341-348.

Alrashdan, A., Mayyas, A.T. and Al-Hallaj, S., 2010. Thermo-mechanical behaviors of the expanded graphite-phase change material matrix used for thermal management of Li-ion battery packs. *Journal of Materials Processing Technology*, 210(1), pp.174-179.

Althaher, M.A., Abdul-Rassol, A.A., Ahmed, H.E. and Mohammed, H.A., 2012. Turbulent heat transfer enhancement in a triangular duct using delta-winglet vortex generators. *Heat Transfer—Asian Research*, 41(1), pp.43-62.

Andrea, D., 2010. *Battery management systems for large lithium-ion battery packs*. Artech house.

Arcus, C., 2016. Tesla Model S Battery vs Nissan LEAF Battery vs Chevy Volt Battery. <https://cleantechnica.com/2016/01/06/a-tale-of-3-battery-packs/> (accessed May 17, 2017).

Bandhauer, T.M., Garimella, S. and Fuller, T.F., 2011. A critical review of thermal issues in lithium-ion batteries. *Journal of the Electrochemical Society*, 158(3), pp.R1-R25.

Battery University., 2017a. BU-1003: Electric Vehicle (EV) – Battery University. http://batteryuniversity.com/learn/article/electric_vehicle_ev (accessed May 17, 2017).

Battery University., 2017b. Types of Battery Cells; Cylindrical Cell, Button Cell, Pouch Cell. http://batteryuniversity.com/learn/article/types_of_battery_cells (accessed May 17, 2017).

Battery University., 2017c. BU-205: Types of Lithium-ion. http://batteryuniversity.com/learn/article/types_of_lithium_ion (accessed July 4, 2017).

Berini, G.A., Fagas, G., Gammaitoni, L. and Paul, D., 2014. A Research Agenda Towards Zero-Power ICT. In ICT-Energy-Concepts Towards Zero-Power Information and Communication Technology. InTech.

Biswas, G., Torii, K., Fujii, D. and Nishino, K., 1996. Numerical and experimental determination of flow structure and heat transfer effects of longitudinal vortices in a channel flow. *International Journal of Heat and Mass Transfer*, 39(16), pp.3441-3451.

Brodd, R.J., and Kozawa, A., 2009. *Lithium-Ion Batteries*. Springer, New York, NY.

Chen, D., Jiang, J., Kim, G.H., Yang, C. and Pesaran, A., 2016. Comparison of different cooling methods for lithium ion battery cells. *Applied Thermal Engineering*, 94, pp.846-854.

Chen, Y. and Evans, J.W., 1996. Thermal analysis of lithium-ion batteries. *Journal of the Electrochemical Society*, 143(9), pp.2708-2712.

Cho, G.Y., Choi, J.W., Park, J.H. and Cha, S.W., 2014. Transient modeling and validation of lithium ion battery pack with air cooled thermal management system for electric vehicles. *International journal of automotive technology*, 15(5), p.795.

Choi, Y.S. and Kang, D.M., 2014. Prediction of thermal behaviors of an air-cooled lithium-ion battery system for hybrid electric vehicles. *Journal of Power Sources*, 270, pp.273-280.

Chu, P., He, Y.L. and Tao, W.Q., 2009. Three-dimensional numerical study of flow and heat transfer enhancement using vortex generators in fin-and-tube heat exchangers. *Journal of Heat Transfer*, 131(9), p.091903.

Circuit Globe. Difference Between Recruitment and Selection (with Comparison Chart). <http://circuitglobe.com/difference-between-cell-and-battery.html> (accessed June 9, 2017).

Coman, P.T., Rayman, S. and White, R.E., 2016. A lumped model of venting during thermal runaway in a cylindrical Lithium Cobalt Oxide lithium-ion cell. *Journal of Power Sources*, 307, pp.56-62.

CWTD, 2013. CWTD Design Notebook#1.
http://www.cwtd.org/CWTD_Design_Notebook.html (accessed July 8, 2017).

Dahn, J. and Ehrlich, G.M., 2011. Lithium-ion batteries. Linden's handbook of batteries, 4. McGraw Hill, New York, NY.

Demirbas, M.F., 2006. Thermal energy storage and phase change materials: an overview. Energy Sources, Part B: Economics, Planning, and Policy, 1(1), pp.85-95.

Dhameja, S., 2001. Electric vehicle battery systems. Newnes.

Drake, S.J., Martin, M., Wetz, D.A., Ostanek, J.K., Miller, S.P., Heinzl, J.M. and Jain, A., 2015. Heat generation rate measurement in a Li-ion cell at large C-rates through temperature and heat flux measurements. Journal of Power Sources, 285, pp.266-273.

Eaton, J.K., 1994. The effect of embedded longitudinal vortex arrays on turbulent boundary layer heat transfer. Journal of heat transfer, 116, p.871.

Engineering ToolBox., 2017a. Air Properties. http://www.engineeringtoolbox.com/air-properties-d_156.html (accessed July 8, 2017).

Engineering ToolBox., 2017b. Thermal conductivities for some common liquids. http://www.engineeringtoolbox.com/thermal-conductivity-liquids-d_1260.html (accessed July 8, 2017).

Feng, X., He, X., Ouyang, M., Lu, L., Wu, P., Kulp, C. and Prasser, S., 2015a. Thermal runaway propagation model for designing a safer battery pack with 25Ah LiNi_xCo_yMn_zO₂ large format lithium ion battery. Applied Energy, 154, pp.74-91.

Feng, X., Sun, J., Ouyang, M., Wang, F., He, X., Lu, L. and Peng, H., 2015b. Characterization of penetration induced thermal runaway propagation process within a large format lithium ion battery module. Journal of Power Sources, 275, pp.261-273.

Fiebig, M., 1995. Embedded vortices in internal flow: heat transfer and pressure loss enhancement. International Journal of Heat and Fluid Flow, 16(5), pp.376-388.

Fiebig, M., 1998. Vortices, generators and heat transfer. Chemical Engineering Research and Design, 76(2), pp.108-123.

Fiebig, M., Kallweit, P. and Mitra, N.K., 1986. Wing type vortex generators for heat transfer enhancement. Heat Transfer, 1(1986), pp.909-2.

Gu, W.B. and Wang, C.Y., 2000. Thermal-electrochemical modeling of battery systems. *Journal of The Electrochemical Society*, 147(8), pp.2910-2922.

He, F., Li, X. and Ma, L., 2014a. Combined experimental and numerical study of thermal management of battery module consisting of multiple Li-ion cells. *International Journal of Heat and Mass Transfer*, 72, pp.622-629.

He, F., Wang, H. and Ma, L., 2015. Experimental demonstration of active thermal control of a battery module consisting of multiple Li-ion cells. *International Journal of Heat and Mass Transfer*, 91, pp.630-639.

He, J., Liu, L. and Jacobi, A.M., 2014b. Experimental and Numerical Investigation of Surface Convection Enhancement by a V-Formation Delta-Winglet Array in a Developing Channel Flow. *ASHRAE Transactions*, 120(Part 2).

Huat, B.S.L., 2014. Thermal management of electric vehicle battery packs (Doctoral dissertation). National University of Singapore.

Inside EVs., 2015. Tesla or GM: Who has the best battery thermal management?. <http://insideevs.com/tesla-or-gm-who-has-the-best-battery-thermal-management-bower/> (accessed July 8, 2017).

Jain, A., Biswas, G. and Maurya, D., 2003. Winglet-type vortex generators with common-flow-up configuration for fin-tube heat exchangers. *Numerical Heat Transfer: Part A: Applications*, 43(2), pp.201-219.

Jarrett, A. and Kim, I.Y., 2011. Design optimization of electric vehicle battery cooling plates for thermal performance. *Journal of Power Sources*, 196(23), pp.10359-10368.

Jarrett, A. and Kim, I.Y., 2014. Influence of operating conditions on the optimum design of electric vehicle battery cooling plates. *Journal of Power Sources*, 245, pp.644-655.

Johnson, V.H., Pesaran, A.A. and Sack, T., 2001. Temperature-dependent battery models for high-power lithium-ion batteries (No. NREL/CP-540-28716). National Renewable Energy Lab., Golden, CO (US).

Kalhammer, F.R., Kopf, B.M., Swan, D.H., Roan, V.P. and Walsh, M.P., 2007. Status and prospects for zero emissions vehicle technology. Report of the ARB Independent Expert Panel, 1(1), pp.12-36.

Karimi, G. and Dehghan, A.R., 2014. Thermal analysis of high-power lithium-ion battery packs using flow network approach. *International Journal of Energy Research*, 38(14), pp.1793-1811.

Kim, G.H., Gonder, J., Lustbader, J. and Pesaran, A., 2008. Thermal management of batteries in advanced vehicles using phase-change materials. *The World Electric Vehicle Journal*, 2(2), pp.0134-0147.

Kim, U.S., Shin, C.B. and Kim, C.S., 2009. Modeling for the scale-up of a lithium-ion polymer battery. *Journal of Power Sources*, 189(1), pp.841-846.

Kizilel, R., Lateef, A., Sabbah, R., Farid, M.M., Selman, J.R. and Al-Hallaj, S., 2008. Passive control of temperature excursion and uniformity in high-energy Li-ion battery packs at high current and ambient temperature. *Journal of Power Sources*, 183(1), pp.370-375.

Kuper, C., Hoh, M., Houchin-Miller, G. and Fuhr, J., 2009. Thermal management of hybrid vehicle battery systems. *EVS24, Stavanger, Norway*, pp.1-10.

Lee, G.G., Allan, W.D. and Boulama, K.G., 2013. Flow and performance characteristics of an Allison 250 gas turbine S-shaped diffuser: Effects of geometry variations. *International Journal of Heat and Fluid Flow*, 42, pp.151-163.

Lei, Y.G., He, Y.L., Tian, L.T., Chu, P. and Tao, W.Q., 2010. Hydrodynamics and heat transfer characteristics of a novel heat exchanger with delta-winglet vortex generators. *Chemical Engineering Science*, 65(5), pp.1551-1562.

Li, X., He, F. and Ma, L., 2013. Thermal management of cylindrical batteries investigated using wind tunnel testing and computational fluid dynamics simulation. *Journal of Power Sources*, 238, pp.395-402.

Ling, Z., Chen, J., Fang, X., Zhang, Z., Xu, T., Gao, X. and Wang, S., 2014. Experimental and numerical investigation of the application of phase change materials in a simulative power batteries thermal management system. *Applied Energy*, 121, pp.104-113.

Ling, Z., Wang, F., Fang, X., Gao, X. and Zhang, Z., 2015. A hybrid thermal management system for lithium ion batteries combining phase change materials with forced-air cooling. *Applied Energy*, 148, pp.403-409.

Liu, Y.P., Ouyang, C.Z., Jiang, Q.B., and Liang, B., 2015. Design and parametric optimization of thermal management of lithium-ion battery module with reciprocating air-flow. *Journal of Central South University*, 22(10), pp.3970–3976.

Mahamud, R. and Park, C., 2011. Reciprocating air flow for Li-ion battery thermal management to improve temperature uniformity. *Journal of Power Sources*, 196(13), pp.5685-5696.

McKinney, B.L., Wierschem, G.L. and Mrotek, E.N., 1983. Thermal management of lead-acid batteries for electric vehicles (No. 830229). SAE Technical Paper.

Menter, F.R., Kuntz, M. and Langtry, R., 2003. Ten years of industrial experience with the SST turbulence model. *Turbulence, heat and mass transfer*, 4(1), pp.625-632.

Moffat, R.J., 1988. Describing the uncertainties in experimental results. *Experimental thermal and fluid science*, 1(1), pp.3-17.

National Instruments. NI USB-9211/9211A. <http://www.ni.com/pdf/manuals/371566e.pdf> (accessed October 16, 2016).

National Research Council, 2012. *The Role of the Chemical Sciences in Finding Alternatives to Critical Resources: A Workshop Summary*. National Academies Press.

Ohzuku, T. and Brodd, R.J., 2007. An overview of positive-electrode materials for advanced lithium-ion batteries. *Journal of Power Sources*, 174(2), pp.449-456.

Omar, N., Monem, M.A., Firouz, Y., Salminen, J., Smekens, J., Hegazy, O., Gaulous, H., Mulder, G., Van den Bossche, P., Coosemans, T. and Van Mierlo, J., 2014. Lithium iron phosphate based battery—assessment of the aging parameters and development of cycle life model. *Applied Energy*, 113, pp.1575-1585.

Omega. User's Guide (HFS-3, HFS-4 Thin Film Flux Sensors). <http://www.omega.com/manuals/manualpdf/m1844.pdf> (accessed March 27, 2017).

Pals, C.R. and Newman, J., 1995. Thermal modeling of the lithium/polymer battery I. Discharge behavior of a single cell. *Journal of the Electrochemical Society*, 142(10), pp.3274-3281.

Panchal, S., 2016. *Experimental investigation and modeling of lithium-ion battery cells and packs for electric vehicles* (Doctoral dissertation). Faculty of Engineering and Applied Science, University of Ontario Institute of Technology.

Panchal, S., Mathewson, S., Fraser, R., Culham, R. and Fowler, M., 2015. Thermal management of lithium-ion pouch cell with indirect liquid cooling using dual cold plates approach. *SAE International Journal of Alternative Powertrains*, 4(2015-01-1184), pp.293-307.

Park, J.K. ed., 2012. Principles and applications of lithium secondary batteries. John Wiley & Sons.

Park, S. and Jung, D., 2013. Battery cell arrangement and heat transfer fluid effects on the parasitic power consumption and the cell temperature distribution in a hybrid electric vehicle. *Journal of Power Sources*, 227, pp.191-198.

Pesaran, A.A., 2002. Battery thermal models for hybrid vehicle simulations. *Journal of power sources*, 110(2), pp.377-382.

Pesaran, A., Keyser, M. and Burch, S., 1999. An approach for designing thermal management systems for electric and hybrid vehicle battery packs (No. NREL/CP-540-25992). National Renewable Energy Laboratory, Golden, CO (US).

Qu, Z.G., Li, W.Q. and Tao, W.Q., 2014. Numerical model of the passive thermal management system for high-power lithium ion battery by using porous metal foam saturated with phase change material. *International Journal of Hydrogen Energy*, 39(8), pp.3904-3913.

Ramadass, P., Haran, B., White, R. and Popov, B.N., 2002. Capacity fade of Sony 18650 cells cycled at elevated temperatures: Part I. Cycling performance. *Journal of power sources*, 112(2), pp.606-613.

Rao, Z. and Wang, S., 2011. A review of power battery thermal energy management. *Renewable and Sustainable Energy Reviews*, 15(9), pp.4554-4571.

Rao, Z., Wang, S. and Zhang, G., 2011. Simulation and experiment of thermal energy management with phase change material for ageing LiFePO₄ power battery. *Energy Conversion and Management*, 52(12), pp.3408-3414.

Sabbah, R., Kizilel, R., Selman, J.R. and Al-Hallaj, S., 2008. Active (air-cooled) vs. passive (phase change material) thermal management of high power lithium-ion packs: Limitation of temperature rise and uniformity of temperature distribution. *Journal of Power Sources*, 182(2), pp.630-638.

Samsung SDI Company Ltd., 2014. Lithium-ion rechargeable cell for power tools Model name: INR18650-25R. http://dalincom.ru/datasheet/SAMSUNG_INR18650-25R.pdf (accessed March 27, 2017).

Saw, L.H., Ye, Y., Tay, A.A., Chong, W.T., Kuan, S.H. and Yew, M.C., 2016. Computational fluid dynamic and thermal analysis of Lithium-ion battery pack with air cooling. *Applied Energy*, 177, pp.783-792.

Schalkwijk, W. and Scrosati, B., 2002. Advances in Lithium Ion Batteries Introduction. *Advances in Lithium-Ion Batteries*, pp.1-5.

Smart Battery. Cylindrical Vs Prismatic Cells. <https://www.lithiumion-batteries.com/cylindrical-vs-prismatic-cells.php> (accessed June 7, 2017).

Somasundaram, K., Birgersson, E. and Mujumdar, A.S., 2012. Thermal–electrochemical model for passive thermal management of a spiral-wound lithium-ion battery. *Journal of Power Sources*, 203, pp.84-96.

Sparrow, E.M., Abraham, J.P. and Minkowycz, W.J., 2009. Flow separation in a diverging conical duct: effect of Reynolds number and divergence angle. *International Journal of Heat and Mass Transfer*, 52(13), pp.3079-3083.

Spotnitz, R. and Franklin, J., 2003. Abuse behavior of high-power, lithium-ion cells. *Journal of Power Sources*, 113(1), pp.81-100.

Tarascon, J.M. and Armand, M., 2001. Issues and challenges facing rechargeable lithium batteries. *Nature*, 414(6861), pp.359-367.

Team, M.E.V., 2008. A guide to understanding battery specifications. Academia. edu. http://web.mit.edu/evt/summary_battery_specifications.pdf (accessed June 7, 2017).

Tiggelbeck St., Mitra N.K. and Fiebig M.M., 1994. Comparison of Wing-Type Vortex Generators for Heat Transfer Enhancement in Channel Flows. *Journal of Heat Transfer*, 116(4), pp.880-885.

Tian, L.T., He, Y.L., Lei, Y.G. and Tao, W.Q., 2009. Numerical study of fluid flow and heat transfer in a flat-plate channel with longitudinal vortex generators by applying field synergy principle analysis. *International Communications in Heat and Mass Transfer*, 36(2), pp.111-120.

United States Environmental Protection Agency, 2015. Sources of greenhouse gas emissions. <https://www.epa.gov/ghgemissions/sources-greenhouse-gas-emissions> (accessed July 8, 2017).

Vyroubal, P., Kazda, T., Maxa, J. and Vondrák, J., 2015. Analysis of temperature field in lithium ion battery by discharging. *ECS Transactions*, 70(1), pp.269-273.

Wang, C.C., Lo, J., Lin, Y.T. and Wei, C.S., 2002. Flow visualization of annular and delta winlet vortex generators in fin-and-tube heat exchanger application. *International Journal of Heat and Mass Transfer*, 45(18), pp.3803-3815.

Wang, T., Tseng, K.J. and Zhao, J., 2015. Development of efficient air-cooling strategies for lithium-ion battery module based on empirical heat source model. *Applied Thermal Engineering*, 90, pp.521-529.

Wang, T., Tseng, K.J., Zhao, J. and Wei, Z., 2014. Thermal investigation of lithium-ion battery module with different cell arrangement structures and forced air-cooling strategies. *Applied energy*, 134, pp.229-238.

Wenige, R., Niemann, M., Heider, U., Jungnitz, M. and Hilarius, V., 1997. Liquid electrolyte systems for advanced lithium batteries. In *Proceeding of the Industrial Chemistry Symposium* (pp. 61–76). Seoul, Korea.

Wu, M.S., Liu, K.H., Wang, Y.Y. and Wan, C.C., 2002. Heat dissipation design for lithium-ion batteries. *Journal of power sources*, 109(1), pp.160-166.

Yang, N., Zhang, X., Li, G. and Hua, D., 2015. Assessment of the forced air-cooling performance for cylindrical lithium-ion battery packs: A comparative analysis between aligned and staggered cell arrangements. *Applied Thermal Engineering*, 80, pp.55-65.

Yang, T., Yang, N., Zhang, X. and Li, G., 2016. Investigation of the thermal performance of axial-flow air cooling for the lithium-ion battery pack. *International Journal of Thermal Sciences*, 108, pp.132-144.

Yu, K., Yang, X., Cheng, Y. and Li, C., 2014. Thermal analysis and two-directional air flow thermal management for lithium-ion battery pack. *Journal of Power Sources*, 270, pp.193-200.

Zhang, S.S., 2007a. A review on the separators of liquid electrolyte Li-ion batteries. *Journal of Power Sources*, 164(1), pp.351-364.

Zhang, S.S., 2007b. An overview of the development of Li-ion batteries: From material, single cell to battery pack, in *advanced materials and methods for Lithium-ion batteries*. Canada: Research Signpost, pp.1-22.

Zhang, L., Shang, B., Meng, H., Li, Y., Wang, C., Gong, B. and Wu, J., 2016. Effects of the arrangement of triangle-winglet-pair vortex generators on heat transfer performance of the shell side of a double-pipe heat exchanger enhanced by helical fins. *Heat and Mass Transfer*, 1(53), pp.127-139.

Zhao, J., Rao, Z., Huo, Y., Liu, X. and Li, Y., 2015. Thermal management of cylindrical power battery module for extending the life of new energy electric vehicles. *Applied Thermal Engineering*, 85, pp.33-43.